

**Quantitative and intuitive liver tumor
treatment with multi-constrained
planning and holographic augmented
reality**

Dissertation

zur

Erlangung des Doktorgrades (*Dr. rer. nat.*)

der

Mathematisch-Naturwissenschaftlichen Fakultät

der

Rheinischen Friedrich–Wilhelms–Universität Bonn

vorgelegt von

Ruotong LI

aus

Xi'an, China

Bonn 2022

Angefertigt mit Genehmigung der Mathematisch-Naturwissenschaftlichen
Fakultät der Rheinischen Friedrich-Wilhelms-Universität Bonn

Erstgutachter: Prof. Dr. Reinhard Klein
Zweitgutachter: Prof. Dr. Thomas Schultz

Tag der Promotion: 12. Dezember 2022
Erscheinungsjahr: 2022

Abstract

In recent years, thermal ablation has become a widely accepted minimal invasive treatment for liver tumor patients. However, surgical planning and performing are still challenging tasks in two aspects: on one hand, surgical planning relies on fulfilling multiple medical constraints, especially for the ablation based on configurations of multiple electrodes. On the other hand, the precise and efficient performance of the percutaneous tumor punctures under free-breathing conditions is hard to achieve because of the high dependency on surgeons' experience.

This thesis presents a novel quantitative and intuitive surgical planning and navigation modality for percutaneous respiratory tumor puncture via holographic visualization, which overlays the pre-operative computer-assisted surgical planning and navigation information precisely onto the intra-operative surgical scenario.

In the pre-operation stage, we present the versatile approach for the computer-assisted planning of liver tumor thermal ablation, including the multi-electrode configuration for large tumors based on the patient-specific anatomical data and the insertion trajectory determine based on a series of medical constraints. We also build up the internal-external correlation model which represents the liver and tumor state under free-breathing with respect to the skin markers attached to the patient. In the intra-operative stage, we first propose a virtual-real alignment method to precisely superimpose the virtual information on the surgical scenario. Then, a user-friendly collaborative holographic interface is designed for real-time 3D respiratory tumor puncture navigation, which can assist surgeons in fast and accurately localizing needles towards the target step-by-step.

In comparison to the state-of-the-art method and manually sketched thermal planning result, our method can achieve compact ablation regions without relying on assumptions of potential needle path search. This navigation system is validated on the static abdominal phantom, in-vivo beagle dogs, or pigs with artificial lesions. Experimental results demonstrate that the proposed holographic augmented reality navigation modality can effectively reduce the needle adjustment for precise puncture.

Our surgical navigation system shows its clinical feasibility to provide the quantitative planning of optimal thermal ablation, which allows completely ablating the tumor region as well as reducing the damage of healthy tissue in comparison to the previous state-of-the-art method. In addition, the proposed augmented virtual reality navigation system can effectively improve the precision and reliability in percutaneous hepatic tumor treatment and has the potential to be used for other surgical planning and navigation tasks.

Keywords: Liver tumor ablation, Surgical navigation, Pre-operative planning, Augmented reality, Mixed reality

Acknowledgments

First of all, I'd like to thank Prof. Dr. Reinhard Klein for his outstanding support and guidance. Prof. Klein is not only a supervisor who gave me the chance to study and work on interesting topics in the computer graphics group, but also a venerable elder who sparked my passion for research. He taught me so much and gave much great advice. And inspired by his example, our group always works in a high spirit and friendly atmosphere.

Then, I would like to thank all my colleagues in the Department of Computer Science II, University of Bonn. I feel so lucky for being a part of the team. Especially to Dr. Michael Weinmann and Sebastian Merzbach, who guided me through their constant feedback. I learned a lot from them. Other colleagues: Elena Trunz, Alex Dieckmann, Dennis den Brok, Richard Vock, Sebastian Ochmann and Stefan Krumpfen gave me lots of useful advice on research. Besides, I would like also to thank Ralf Sarlette, Simone von Neffe, and Michaela Mettler for helping me solve problems in the office and for living in Bonn. Besides, I would like to thank Prof. Dr. Thomas Schultz for his valuable advice on my thesis.

Furthermore, I'd like to thank Dr. Weixin Si, Tianpei Yang, and the colleagues I worked with at Shenzhen Institute of Advanced Technology, Chinese Academy of Sciences during my internship. I enjoyed working with you during the year. Collaborating with Tianpei Yang is truly an unforgettable experience, from which we worked so effectively to achieve our fruitful result. At the same time, I'd like to thank the doctors and technicians from the co-operation hospitals. On multiple occasions, we conducted our experiment well past midnight; I really appreciate the personal sacrifice you made to help our team complete the project.

I would like to thank Peter Gaal, Marianne Hilgel and Toni Higel, Ying Shang and all the friends and acquaintances I met in Bonn over the years. I felt so fortunate to have you around in the years I spent in Bonn. Your friendship and hospitality made me feel at home.

I'd like to thank the city of Bonn. It is such an enchanting place that after spending eight years of my youth here, it still feels too short.

I'd like to thank my family members and friends. Without their encouragement and support, I would never finish this thesis.

Finally, I would like to give a special thanks to Dr. Lu Wang, the one who encouraged me to leave my comfort zone to study abroad, the one who inspired me to begin my doctorate despite hesitation, the one who prodded me to continue when I want to give up. Without you, I may have never taken the first step on this long journey, nor will I meet so many interesting people and see such a wide world. This acknowledgment will be incomplete without your name.

Contents

List of Figures	x
List of Tables	xi
Abbreviations	xiv
I Introduction	1
1	3
1.1 Overview	3
1.2 Medical background	3
1.2.1 Liver tumor treatment	3
1.2.2 Thermal ablation planning	5
1.2.3 Liver tumor puncture	5
1.3 Augmented Reality	6
1.3.1 Commercial application of AR	6
1.3.2 AR-guided surgery	7
1.4 Challenges and Main Contributions	10
1.4.1 Surgical planning for liver tumor treatment	10
1.4.2 Dynamic liver tumor puncture	13
1.4.3 Augmented virtual reality guided liver tumor puncture under respiration	13
1.4.4 Overview of solution in this thesis	14
1.5 Publications and thesis outline	16
II Multi-constrained surgical planning for liver tumor ablation	19
2	21
2.1 Introduction	23
2.1.1 Related Work	24
2.1.2 Contributions	26
2.2 Materials and Methods	27
2.2.1 Initial Tumor Segmentation	28
2.2.2 Finding an Optimal Electrode Configuration for Thermal Ablation	28
2.2.3 Medical-constraint-based Determination of Needle Target Positions	30

2.2.4	Constraint-based Optimization of Needle Insertion Paths	32
2.3	Results	36
2.3.1	Experimental Materials	36
2.3.2	Result	37
2.3.3	Multi-electrode Plannings	41
2.3.4	Computational Time	41
2.4	Discussion	43
III Dynamic tumor puncture		49
3		51
3.1	Introduction	53
3.2	Methodology	54
3.2.1	Raw medical data acquisition and processing	54
3.2.2	Respiratory motion reconstruction	55
3.2.3	Tumor Position Prediction	56
3.2.4	Dynamic virtual-real alignment	57
3.3	Experiment	59
3.3.1	Material	59
3.3.2	Result	59
3.3.3	Discussion	60
3.4	Conclusion	60
4		63
4.1	Introduction	65
4.2	Related work	67
4.3	Methodology	69
4.3.1	Method overview	69
4.3.2	Medical Data Acquisition and Preprocessing	70
4.3.3	Virtual-real spatial information visualization registration	70
4.3.4	Statistical model based respiratory motion compensation	72
4.4	Results	76
4.4.1	Registration accuracy validation	76
4.4.2	Needle Insertion Comparison	77
4.5	Conclusion	79
IV Surgical navigation based on holographic augmented		

reality	83
5	85
5.1 Introduction	87
5.2 Related Work	90
5.3 Puncture Path	91
5.3.1 Patient Specific 3D Model Reconstruction	92
5.3.2 SDF-based Feasible Region Determination	93
5.3.3 Constraint-based Puncture Path Optimization	93
5.4 Puncture Navigation	96
5.4.1 Static Virtual-Real Alignment	96
5.4.2 Respiratory Motion Modeling of Target Region	98
5.4.3 Intra-operative Dynamic Alignment	101
5.5 Navigation Interface	101
5.5.1 Vision cue for accurate insertion	101
5.5.2 User Interface Integration	104
5.6 Experiments	105
5.6.1 Path planning result evaluation	106
5.6.2 System Calibration	106
5.6.3 Tumor Prediction Validation	109
5.6.4 System Communication	112
5.6.5 Puncture Experiment	112
5.7 Discussion	115
5.8 Conclusion and Future Work	116
V Discussion	119
6	121
6.1 Conclusion	121
6.2 Limitations and Future Work	122
6.2.1 Soft tissue prediction for the respiration movement	123
6.2.2 Flexible needle behavior prediction	124
6.2.3 Thermal ablation planning for versatile needle configuration	124
6.2.4 Surgical planning in other surgical scenarios	124

List of Figures

1.1	Augmented reality display techniques	6
1.2	Traditional thermal ablation surgery vs. AR guided minimal invasive surgery	7
1.3	Typical structure of an AR-based surgical navigation system	8
1.4	Our solution for liver tumor treatment with multi-constrained planning and holographic augmented reality	15
2.1	Illustration of the steps in our multi-constrained planning ap- proach for the thermal ablation of large liver tumors.	24
2.2	2D illustration of the specification of the treatment zone. . .	28
2.3	2D illustration of the effects of different needle positions and ablation radii.	30
2.4	2D illustration of the different types of constraints we used for the optimization of insertion paths of individual electrodes.	34
2.5	The anatomical structure of three clinical cases reconstructed from the medical data	44
2.6	The treatment zone of the 4 tumors in the five medical cases	45
2.7	MWA electrode ablation region validation on isolated bovine liver.	45
2.8	The needle target and trajectory planning result for the cases 1 to 3-1.	46
2.9	The needle target and trajectory planning result for the cases 3-1 to 5.	47
2.10	The CT images of the clinical outcome by surgeons.	48
3.1	Pipeline of AR-based surgical navigation system	55
3.2	Raw medical data acquisition.	56
3.3	Coordinate transformation	58
3.4	The surgeon performed AR-guided needle insertion.	60
3.5	Needle insertion result in CT	60
4.1	Mixed reality based needle insertion navigation.	66
4.2	Coordinate calibration between Microsoft HoloLens and NDI tracking system.	68
4.3	Statistical model based respiratory motion compensation. . .	69
4.4	Registration of 3D virtual structure and real object.	71
4.5	Patient-specific respiratory motion reconstruction.	72
4.6	Animal experiment setting and 3D reconstruction results. . .	73
4.7	Automatic registration accuracy validation, red points are landmarks.	75

4.8	The results of traditional CT-navigated needle insertion. . . .	76
4.9	Mixed reality-navigated needle insertion.	77
4.10	The results of our mixed reality-based needle insertion navigation.	77
5.1	The pipeline of our augmented virtual reality based respiratory liver tumor puncture.	89
5.2	The process of virtual puncture path planning.	92
5.3	Coordinate transformation for system configuration.	97
5.4	The scenario for raw medical data acquisition of the experimental animal.	100
5.5	Illustration of the insertion point.	102
5.6	Illustration of the puncture direction	103
5.7	Illustration of the way points	103
5.8	Illustration of the integration of visual cues in our augmented reality surgical navigation interface.	105
5.9	Path planning result for static multi-targets abdominal phantom.	107
5.10	The puncture result of static phantom under our augmented virtual reality navigation system.	108
5.11	Calibration accuracy test	109
5.12	Accuracy of the respiratory motion prediction	111
5.13	The surgeon performed AR-guided needle insertion on beagle dog.	114
5.14	CT result of the needle insertion	115

List of Tables

1.1	Ablation modality	4
1.2	Recent work on general surgery with augmented reality	9
1.3	Relevant work on tumor ablation surgical planning	11
2.1	Resulting number of electrodes and ablation regions.	39
2.2	Results for trajectory planning.	40
2.3	Comparison between our target planning and the manual planning performed by doctors.	42
2.4	Ablation target result comparison	42
3.1	Accuracy comparison of AR-guided and traditional CT- guided modalities.	61
4.1	Performance statistics of automatic registration (<i>mm</i>).	78
5.1	Path planning result compared with ground truth	107
5.2	Registration error comparison	110
5.3	Data transfer delay from PC to HoloLens2 and frame rate of HoloLens2	113

Abbreviations

An alphabetically sorted list of abbreviations used in the dissertations:

AR	Augmented Reality
Cryo-A	Cryoablation
CT	Computational tomography
DBS	Deep brain stimulation
DICOM	Digital Imaging and Communications in Medicine
GMLS	Generalized moving least square
HIFU	High-intensity focused ultrasound
IRE	Irreversible electroporation
LA	Laser ablation
MIS	Minimally invasive surgery
MR	Mixed Reality
MRC	Mixed Reality Capture
MRI	Magnetic Resonance Imaging
MRTK	open-source Mixed Reality ToolKit
MWA	Microwave ablation
OST-HMD	Optical see-through head-mounted display
PD	Parkinson's disease
PEI	Percutaneous ethanol injection
QICP	Quaternion-based iterative closest point
RFA	Radiofrequency ablation
RGMLS	Regularization GMLS
SEEG	Stereoelectroencephalography
TRE	Target registration error
US	Ultral Sound
VR	Virtual Reality

Part I

Introduction

Introduction

1.1 Overview

According to the WHO statistics [World Health Organization, 2021], the hepatic tumor is one of the most common types of cancer in humans. Therefore, doctors and researchers are looking for treatments that allow fast rehabilitation and minimal invasion. Compared with traditional open surgery, minimal invasive surgery can remove, ablate or kill the cancer cells in a short time with less damage to the healthy tissue, thus has become a widely accepted treatment in last years. Tumor ablation is a typical intervention surgery that kills the cancer cell with chemicals, energy or heat. Thermal ablation is the most common treatment way among all these solutions [Salati et al., 2017].

In practice, the liver tumor thermal ablation is performed via two steps: 1) pre-operative planning and 2) the percutaneous puncture. The surgical planning is done by the surgeons: determine the ablation boundary with the medical images, ensure the location of the ablation center, i.e. the insertion target of the ablation needle, and plan the trajectory of ablation needle insertion. While performing the percutaneous puncture, doctors will manually insert the biopsy or ablation needle into a patient with the imagination of the target structure. In order to fulfill the requirement for precise and qualitative treatment in modern medical, quantitative and intuitive surgical planning and navigation are urgently needed.

The aim of this thesis is to provide a solution for a quantitative and intuitive treatment of the liver tumor with computer assisted method. In particular, this thesis talks about the multi-constrained pre-operative planning for liver tumor thermal ablation, intra-operative dynamic surgical target movement estimation, and the holographic augmented reality navigation for percutaneous tumor puncture respectively.

1.2 Medical background

1.2.1 Liver tumor treatment

Traditionally, tumors are treated by surgical resection, such as removal of the tumor region in organs or an organ transplant. However, due to its large open wound and long rehabilitation, it is not the best option for all patients.

Compared with traditional open surgery that always gives a large open wound, tumor ablation is performed in a minimally invasive or non-invasive way. It is a minimal invasive surgical method for treating solid cancers in the lung, liver, bone or kidney [The Johns Hopkins University, 2022b].

The indications of tumor ablation are patients with a few small or slightly large tumors, i.e. whose diameter is smaller than 5cm. For the patients with small hepatocellular carcinomas or benign tumors in the liver, tumor ablation surgery is considered the first-line therapy for them [Knavel and Brace, 2013]. Nowadays, thermal ablation surgery methods such as radiofrequency ablation (RFA) and microwave ablation (MWA) approaches have become particularly popular for hepatic tumor treatment [Salati et al., 2017]. This is partly because the development of medical image techniques and early diagnosis of liver cancer gives the opportunity to cure hepatic cancer in this minimal invasive way. And because of its fast rehabilitation and minimal invasion, ablation surgery is also considered the best option for those patients who are not suited for the traditional open surgery, i.e. the ones with poor health or liver function reduction [American Cancer Society, Inc, 2022].

Table 1.1: Ablation modality

Abb.	Ablation Modalities	Surgical Type
RFA	Radio-frequency ablation: Ionic agitation and production of frictional heat by current flowing through tissue.	Minimal invasive
MWA	Microwave ablation: uses dielectric hysteresis to produce heat in tissue	Minimal invasive
LA	Laser ablation: Fiberoptic applicator are used for applying the yttrium aluminum garnet lasers to target tissue. The light energy then converted into heat in tissue.	Minimal invasive
HIFU	High-intensity focused ultrasound: With increased intensity of the ultrasound, the region of interest absorb the this high-intensity energy acoustic wave and cause ablative heating of the target.	Noninvasive
Cryo-A	Cryoablation: Create rapid cooling inside the most distal end of cryoprobe with the change of gas pressure; destroys tumors by cooling them to cytotoxic temperatures.	Minimal invasive
IRE	Irreversible electroporation: Pulses of electrical current transmitted through the electrodes, cause irreversible damage to the cell membrane, and initiation of apoptosis.	Minimal invasive
PEI	Ethanol (alcohol) ablation: also known as percutaneous ethanol injection (PEI)	minimal invasive

Notes: Abb.: Abbreviations; Minimal invasive: percutaneously, laparoscopically, through a celiotomy incision, or endoscopically.

Tab. 1.1 Listed some of the common modalities of tumor ablation: radiofrequency, microwave, laser, high-intensity focused ultrasound, cryoablation, and irreversible electroporation [Knavel and Brace, 2013]. In the minimal invasive ablation like RFA, MWA, LA, etc., doctors insert one or multiple ablation probes into the tumor target percutaneously, laparoscopically, through a celiotomy incision, or endoscopically. With the temperature

change at the ablation needle tip, tissue is cool or heated to cytotoxic levels, so that the cancer cell can be destroyed. Careful surgical planning and accurate probe localizing are necessary for achieving good treatment results.

1.2.2 Thermal ablation planning

Thermal ablation of liver tumors is performed via inserting one or multiple ablation needles, i.e. radiofrequency probes (in RFA) or electrodes (in MWA) into the target tumor region. Then, the ablation needles are powered on and generate a high temperature at the needle tip that heats the tumor tissue to the temperature (eg. in RFA is higher than 60° C) so that the cancer cells can be killed [Minami and Kudo, 2013, Simon et al., 2005].

The shape of an ablation region is a spherical-like volume where the heat distribution has the highest temperature at the needle tip, from where it is decreasing to the spherical border [Chen et al., 2018b]. The radius of the ablation region is influenced by two aspects: on the one hand, it can be modified by changing the configuration of the needle, such as the energy and the duration of the power on the ablation needle. On the other hand, for the same configuration of the needle, the fat and water content in the tissue may also influence the shape of the ablation region. When there are more than one electrode or probe working together, the effect region will increase and influence each other. In these cases, surgeons need not only consider the heat distribution for each needle but also influence the heat distribution between multi-needles and their effect regions.

In order to achieve complete ablation of the lesion tissue, the center of the ablation region, with respect to the tip of the ablation needle should be located inside the tumor and the ablation radius should completely cover the tumor region with a safety margin of $5mm$ according to experts' consensus. The presence or extent of the tumor can be determined by medical image analysis and biopsy tests. For minimizing the damage to the healthy tissue, the ablation region should cover as less healthy tissue as possible. In other words, a too large ablation region may cause damage to healthy tissue while a too small ablation region may cause an incomplete treatment which leads to severe aftereffects [Liang et al., 2009]. Therefore, precise pre-operative planning is the key factor for the successful ablation of cancer tumors.

1.2.3 Liver tumor puncture

Liver tumor puncture is the key step for both biopsy and thermal ablation in the tumor treatment procedure. In the biopsy step, the doctor punctures the biopsy needle towards the tumor region and assesses the nature and severity of liver diseases via the tissue got from the liver [Bravo et al., 2001]. In the ablation step, cancer cells are killed with the ablation needle that punctured into the tumor region. In both steps, puncture trajectory planning is

necessary for helping surgeons insert the needle towards the target.

In a traditional liver puncture operation, the CT-image-based navigation modality has evolved rapidly over the past decade and become a widely accepted treatment option for patients that needs tumor puncture step in diagnosis or treatment. In this modality, as shown in Fig. 1.2, the pre-operative planning together with the CT image is displayed on the monitor above the operation bed during the surgery. While percutaneously puncturing the ablation needle towards the target tumor, doctors need to look at the screen for observing the trajectory information. For successfully applying the operation, the imagination of abdominal anatomical structures and hand-eye coordination is required. Therefore, the puncture precision and operation efficiency are highly dependent on the surgeon's experience.

1.3 Augmented Reality

Augmented reality techniques can superimpose the virtual information onto the real scenario. This provides depth perception and offers interaction for the user and is widely used in entertainment, education and the industrial environment.

1.3.1 Commercial application of AR



Figure 1.1: Three different ways for visualize augmented reality information. Left: show virtual model on screen of smart phone. Mid: visualize virtual information with 3D projector. Right: show virtual information with OST-HMD.

Besides the holographic augmented reality display with OST-HMDs, there are also other ways for visualizing augmented reality information. Fig.1.1 shows the three common ways for showing the augmented reality information. Mobile Apps like Pokémon Go [Niantic, 2016], Google Measure [Google, 2018] show the virtual model with the camera captured scene on the screen of mobile devices. The 3D projectors such as WERKLICHT [EXTEND3D GmbH, 2019] visualize the AR information with laser

light. These types of 3D projection techniques are often used in the industry or cultural relics protection and presentation.

Today's out-of-shelf OST-HMDs achieve the holographic augmented visualization with different technical routes: Google glass [Google, 2020] equips a small transparent screen on the corner of the glasses to display the UI information. Microsoft HoloLens [Microsoft, 2016, Microsoft, 2019] and Magic Leap [Magic Leap, 2018] integrate screens on both left and right glasses, making use of the stereo effect based on the left and right eye for presenting the 3D scene. Under this modality, the user obtains an immersive depth perception that allows the user to walk around the virtual objects and observe them from different views.

1.3.2 AR-guided surgery

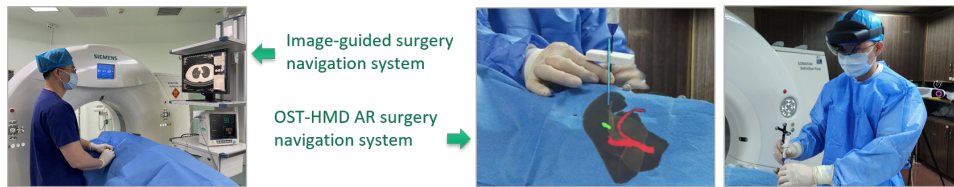


Figure 1.2: Left: In traditional CT image guided surgery, the surgeon is puncturing the ablation needle towards to the tumor, while looking at the screen and analyzing whether the needle trajectory follows the pre-planned path showed on the screen. Right: By employing the optical see-through head mounted display (OST-HMD), it can directly overlay the 3D navigation information of the region of interest onto patient's body.

Nowadays, the AR technique is applied to surgical scenarios by superimposing the internal anatomical structure onto the patients' bodies. As shown in Fig. 1.2, doctors can perform minimal invasive surgery intuitively. Companies like Scopis and Novorad OpenSight have released an augmented reality navigation system for surgery in the spine, dental, neurology and laparoscopic surgery [Scopis Inc., 2017, Novorad Healthcare Imaging, 2019, Bernhardt et al., 2017a, Guha et al., 2017b].

A typical AR-based surgical navigation system contains the following parts: an OST-HMD, a spatial tracking system, a patient model and surgical instruments equipped with tracking markers. In this system, the registration between the pre-operative surgical planning and the intra-operative patient model relies on spatial tracking systems for positioning the OST-HMDs, operation instrument and patient in the operation. During the navigation process, the pre-operative surgical planning information is superimposed onto the patient in real-time, so that doctors can perform the operation in a more intuitive way. Fig. 1.3 shows a typical

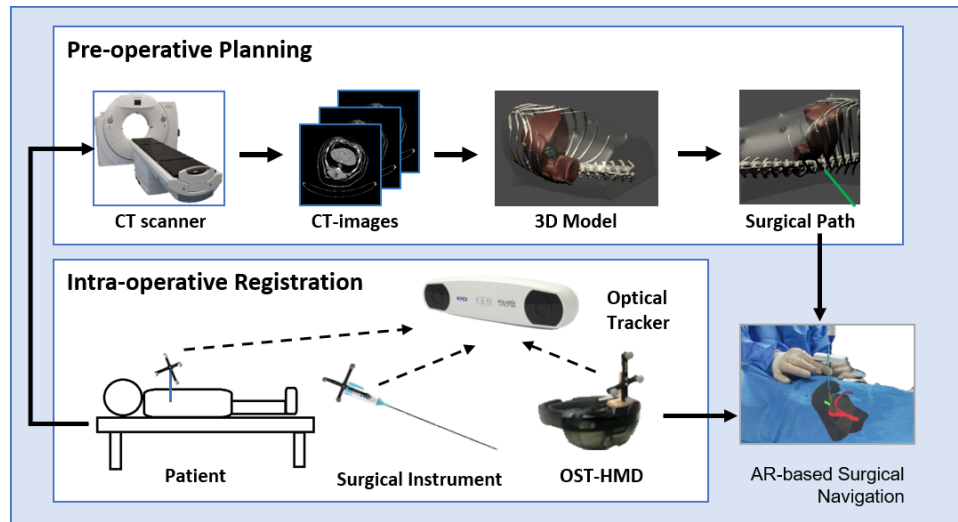


Figure 1.3: A typical AR-based surgical navigation system contains the optical tracker that register all the elements in the surgical scenario so that the pre-operative information can be superimposed on the patient's body precisely.

scenario of the AR-guided operation pipeline. For its intuition and user-friendliness, this technique is applied in the spine, dental and neurology surgery [Novarad Healthcare Imaging, 2019, Scopis Inc., 2017] as well as the telementoring and teleconsultation [Birlo et al., 2022]. However, for soft tissue surgery, the dynamics included by elastically moving structures may influence the position and shape of the target region, thereby can applying the use of this AR-guided surgical modality. Tab. 1.2 gives a brief look at some work in general surgery that is applied with augmented reality techniques.

Table 1.2: Recent work on general surgery with augmented reality

Reference	Surgical context	Calibration and tracking strategy	Display devices
[Andersen et al., 2016]	Abdominal incision telemonitoring	Feature detection	Tablet display
[Lin et al., 2018]	Needle biopsy surgical guidance	OptiTrack Flex 13, strain sensor on needle	HoloLens
[Mahmood et al., 2018]	Surgical training	MRC by HoloLens and Arrow idagram	HoloLens
[Wu et al., 2018]	Surgical guidance	Vuforia’s image tracking together with RGB-D sensor	HoloLens
[Rojas-Muñoz et al., 2019]	Abdominal incision telemonitoring	Same as in [Andersen et al., 2016]	Tablet display
[Pepe et al., 2019]	Surgical guidance for Head and neck tumor resection	Facial landmark detection [Kazemi and Sullivan, 2014]	HoloLens
[Pelanis et al., 2020]	Liver resection pre-operative planning	No	HoloLens
[Zhou et al., 2020]	Surgical navigation for seed implantation thoracoabdominal brachytherapy	QICP for pre-intra operative registration, EM tracker for surgical tool tracking	HoloLens
[Al Janabi et al., 2020]	Surgical guidance for Ureteroscopy	No	HoloLens
[Galati et al., 2020]	Anatomy assessment for open abdomen surgery	MRTK	HoloLens
[Li et al., 2020a]	Surgical planning, training and teleconsultation for Laparoscopic partial/radical nephrectomy	”Vascular bifurcation labeling” technology and manually interaction	HoloLens
[Chan et al., 2021]	Surgical navigation system	NDI inferred tracker	Laser pico-projector

1.4 Challenges and Main Contributions

Computer-assisted thermal ablation for hepatic tumor treatment is complicated by challenges in both the pre-operative stage and intra-operative stage. In the pre-operative stage, surgical planning is the key factor for a successful treatment. The surgical planning should consider using the least number of the electrode to achieve the complete ablation of the tumor region and cause as less healthy-tissue-damage as possible. In the intra-operative stage, the patient's abdomen moves with a wavy motion corresponding to the breath so that the location of the tumor target is not static while performing the puncture. This dynamic scenario gives difficulties in performing the percutaneous puncture. Besides, in order to provide quantitative and intuitive depth perception for the surgeons in the AR-based surgical navigation modality, accurate calibration and useful vision clues are necessary. In the following, we briefly introduce the major challenges for each of these problems in more detail as well as the most closely related work.

1.4.1 Surgical planning for liver tumor treatment

According to the experts' consensus, incomplete ablation may cause severe aftereffects while too large ablation may damage too much healthy tissue may also lead to health issues. Therefore, especially for large tumors, pre-operative planning remains a challenging task that relies on fulfilling multiple medical constraints, especially for the ablation based on configurations of multiple electrodes. The placement of the electrodes to completely ablate the tumor as well as their insertion trajectory to their final position has to be planned to cause as little damage to healthy anatomical structures as possible to allow a fast rehabilitation.

Researchers have considered this planning problem in the scope of medical constraints and thermal distribution analysis, trajectory planning, bio-heat simulation and constraint-based needle tip targeting. The following section thus takes a closer look into thermal ablation surgical planning, with related work summarized in Table 1.3.

Table 1.3: Relevant work on tumor ablation surgical planning

Reference	Method	Topic	Remarks
Medical constraints analysis			
[Livraghi et al., 2003]	Retrospective study	Liver tumor RFA	Report complications encountered by patients
[Liang et al., 2009]	Retrospective study	Liver tumor MWA	Report complications encountered by patients
Thermal distribution Analysis			
[Altrogge et al., 2006]	Numerical computation of heat distribution with temperature based objective function	RFA	Nomo and bipolar probes
[Schumann et al., 2015]	GPU-based simulation of heat distribution together with numerical optimization	Liver RFA	Realistic estimation of the heat distribution is taken into account
[Chen et al., 2018b]	Simplified Pennes bioheat equation	Hepatic RFA	Temperature distribution in RFA + heat-sink effect of vessel
Insertion Path Planning			
[Villard et al., 2005]	Constraint-based Optimization	Hepatic RFA	Delineate candidate insertion zone on skin, compute trajectories to tumor
[Baegert et al., 2007b]	Computation of authorized insertion zones and multi-criteria optimization	RFA on Liver	Single Needle trajectory planning
[Baegert et al., 2007a]	Candidate insertion zone optimal trajectory	RFA	Single Needle trajectory planning
[Schumann et al., 2010]	Weighted combination of cylindrical projections	Percutaneous image-guided interventions (RFA, biopsy, seed implantation)	For a choosing target point, generates paths automatically
[Seitel et al., 2011b]	Pareto optimality with hard and soft constraints	CT guided minimal invasive interventions	Single needle, constraint-based optimization
Needle tip locating			
[Ren et al., 2013]	Multiple-objective optimization	RFA for large tumor	Integer program to find a minimal number of trajectories and ablations along the selected trajectories necessary to cover the tumor.
[Chen et al., 2018a]	Semiautomatic planning on clustering process	RFA for hepatic tumor	Manually defined puncture scope + clustering algorithm
[Liang et al., 2019a]	Multiple Constraints Based on Set Covering	RFA for liver tumor	Multiple ablation regions with the same size. Enumerately scoring all the potential combination of entry point and target point.

In order to consider medical constraints, insertion path planning of the ablation needle can be formulated as a constraint-based optimization problem [Villard et al., 2005]. The underlying goal is the optimization of the insertion path so that it does not pass through any of the critical anatomical structures in the abdomen, such as the gallbladder, bile duct as well as large vessels in and around the liver, and, hence, avoid complications in terms of injuring the bile duct or intestinal perforation [Livraghi et al., 2003, Liang et al., 2009]. Several investigations [Baegert et al., 2007a, Baegert et al., 2007b, Seitel et al., 2011b] focused on the respective optimization with weighted constraints. In further work, Altrogge et al. [Altrogge et al., 2006] discussed the placement of RFA probes via minimizing a temperature-based objective function. The works by Schumann et al. [Schumann et al., 2015, Schumann et al., 2010] have also taken the heat-sink affection into consideration.

However, all of the aforementioned studies only considered the ablation based on a single electrode. For large tumors (i.e. with a *diameter* $> 3\text{cm}$), multiple electrodes are required to cover the treatment zone so that a multi-electrode-based coverage of the region to be ablated has to be considered. Chen et al. [Chen et al., 2018a] introduced a manual adjustment when the planned path passes through large vessels or ribs. The works of Liang et al. [Liang et al., 2019b, Liang et al., 2019a] allow fast and automatic computations of the insertion paths of multiple needles. However, their approach cannot ensure global optimization.

To address this, we propose a novel, versatile approach for the planning of thermal ablation of large liver tumors [Li et al., 2021a]. For this purpose, we formulate the tumor ablation task as a constrained optimization problem that optimizes the placement of the set of involved electrodes and their insertion to the final position.

In contrast to previous work, our approach leverages constraints for avoiding too much overlap of the individual ablation zones, thereby improving the efficiency of the ablation, as well as for exceeding the maximal distance between electrodes in addition to constraints regarding tumor coverage, and the reduction of ablating of healthy tissue. Our approach explicitly allows the optimization regarding a configuration of multiple target positions for the ablation and the respective insertion paths which renders our approach suitable for simultaneous ablation by different electrodes. The evaluation shows that our approach can achieve the optimal planning for the thermal ablation of large liver tumors without the dependence on the clinician’s experience. Compared with the state-of-the-art method and the planning by expert clinicians, our method involves the medically inspired constraints where doctors can set the importance of the individual terms according to patients’ characteristics. Thus, this method has a high potential for guiding the thermal ablation of the tumors.

1.4.2 Dynamic liver tumor puncture

In the intra-operative stage, the patient’s abdomen movement is influenced by the respiratory process. This movement causes the instability of the target tumor location for ablation, thus complicating the puncture by doctors. In the traditional CT-guided liver puncture procedure, doctors need to image the target tumor movement during the puncture procedure. Even nowadays several researchers apply the AR-guided surgical application in different types of operations [Xie et al., 2017, Qian et al., 2018, Novarad Healthcare Imaging, 2019, Scopis Inc., 2017], however, they do not take the dynamic information into account.

In this thesis, we focus on the reconstruction of the patient-specific organ motion together with the tumor position with a statistical motion model. Inspired by the work by [Jud et al., 2017], we [Li et al., 2019a] describe the respiratory motion with a statistical motion model and adopt the variability in 4D for compensating for the movement of liver tumors. By constructing the correlation model of the external movement of skin markers attached to the patient’s abdominal and the internal position of the liver tumor, our prototype can predict the tumor position in real-time via the tracking of the movement of the intra-operative skin markers [Li et al., 2019b]. In our platform, we also propose a calibration procedure to properly align the coordinate system tracking system, the rendering of the virtual surgical navigation information and patient in the real surgical scenario, thereby making the operation simpler, more efficient and accurate. We experimentally validated the proposed system on in vivo beagle dogs and vivo pigs with artificial lesions respectively in the work, which shows that our proposed system can improve the puncture efficiency and precision.

1.4.3 Augmented virtual reality guided liver tumor puncture under respiration

When performing the liver tumor therapy under free-breathing, the puncture target position can be computed via the internal-external correlation model with statistics (see Sec. 1.4.2) and the puncture path can be pre-planned according to the multi-objective constraint-based method (see Sec. 1.4.1). With the augmented reality-based surgical navigation technology, the hand-eye coordination problem can be solved. However, it is still hard for surgeons to locate the needle towards the correct path when there’s only the visualization of the target position. Without quantitative navigation information for the puncture direction and depth, the puncture behavior would be hard to perform. Especially when the needle tip is away from the target, the vision cues like color code [Liu et al., 2018] would be helpful for measuring the accuracy of the needle insertion position and direction. Other types of vision cues for the puncture direc-

tion and utility depth information can also improve the surgical accuracy [Zhou et al., 2019, De Paolis and De Luca, 2019]. However, they only measure the error between the performing and planning, still cannot help surgeons to locate the needle towards the correct path, especially under the dynamic scenario.

In our work [Li et al., 2021b], we present a novel quantitative and intuitive surgical navigation modality for percutaneous tumor puncture under the respiration process via augmented reality, which achieves a precise overlay of the pre-operative virtual planning information onto the intra-operative surgical scenario. In our prototype, the target tumor position can be predicted from the patient-specific pre-operative internal-external correlation model, while the puncture path can be generated from the multi-objective optimization algorithm. In order to provide a precise overlay of the virtual guidance information on the corresponding area of the patient’s body, we track all the utilities in the surgery scenario with an optical tracking system. Besides, this work presents the dynamic update of the pre-planned needle trajectory. Using the pre-operative medical image data, we generate the feasible region for needle puncture. While in the intra-operative navigation, with the update of the target position, our method updates the needle trajectory at the same time to adjust the waypoint’s position to ensure that all of them are located inside the feasible region. For quantitatively measuring the puncture process and enhancing the depth perception, we also integrate way-point visual cues into our guidance information, which can effectively assist surgeons in the fast and accurate location of the target step-by-step. Besides, in our prototype, the time-consuming computations of the surgical guidance information are performed on the desktop while the OST-HMD is only responsible for displaying the well-organized information via network transfer. In this way, the computational power of the present commercial HMDs can be extended. This can also provide more complex but intuitive navigation information for clinicians.

1.4.4 Overview of solution in this thesis

As shown in Fig. 1.4, this thesis gives a solution for performing the efficient and qualitative liver tumor treatment with percutaneous thermal ablation quantitatively and intuitively. The system is working with the respect of:

1. The computer-assisted pre-operative planning based on patient-specific anatomical reconstruction. For the ablation planning, both medical constraints and the attributes of the thermal distribution are used to determine the needle target determination. Geometry constraints and the practical expert consensus are used for generate the optimal trajectory for needle insertion.
2. Dynamic target movement estimation according to statistic motion

model and the respiratory state estimation. Making use of the pre-operative medical data, the internal-external correlation model and the respiratory motion compensation of specific breathing state can be constructed. The intra-operative tumor target position and liver movement can be predicted with the real time capture of the surface marker attached on patient's abdomen according to the internal-external correlation model.

3. Our proposed holographic augmented reality guided liver tumor puncture system calibrated with the optical tracking system. The navigation information involves the target movement and the surrounding tissue movement inside the patient's respiration cycle. During the puncture navigation, the pre-planned needle trajectory is super imposed on the patient's body with the use of OST-HMD. The intra-operative target region movement is updated based on the captured optical markers on patient's abdomen.

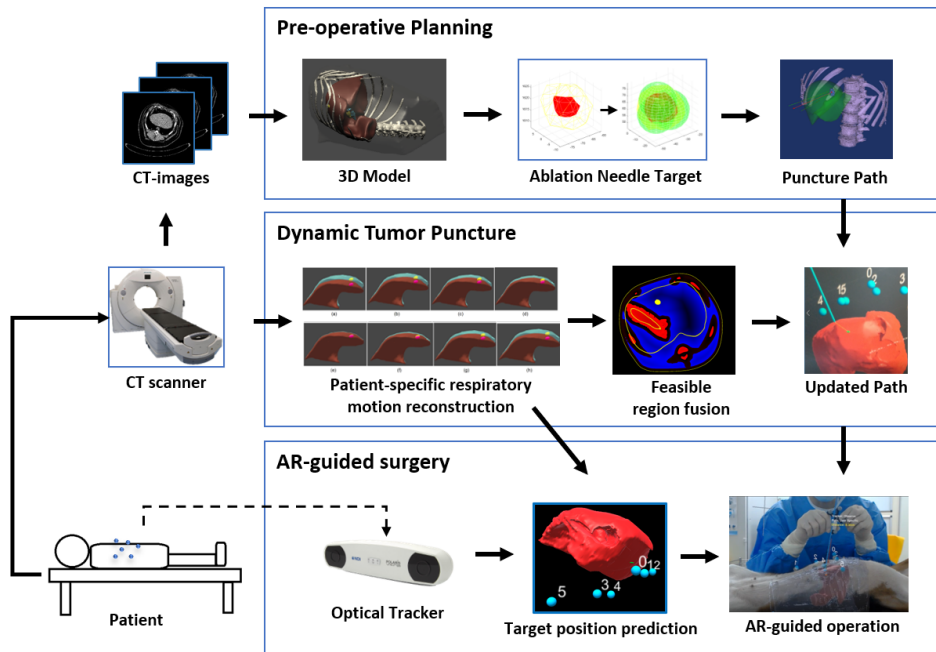


Figure 1.4: Our solution for liver tumor treatment with multi-constrained planning and holographic augmented reality.

1.5 Publications and thesis outline

All of the material involved in this thesis has been published in the scope of peer reviewed journals or conferences:

- **Ruotong Li**, Yangyang Shi, Weixin Si, Li Huang, Bowen Zhuang, Michael Weinmann, Reinhard Klein, Pheng-Ann Heng: Versatile Multi-constrained Planning for Thermal Ablation of Large Liver Tumors. *Computerized Medical Imaging and Graphics*, 94(2021): 101993 doi: 10.1016/j.compmedimag.2021.101993
- **Ruotong Li**, Tianpei Yang, Weixin Si, Xiangyun Liao, Qiong Wang, Reinhard Klein, Pheng-Ann Heng: Augmented Reality Guided Respiratory Liver Tumors Punctures: A Preliminary Feasibility Study. *ACM SIGGRAPH Asia Technical Briefs 2019*: 114-117. doi: 10.1145/3355088.3365166
- **Ruotong Li**, Weixin Si, Xiangyun Liao, Qiong Wang, Reinhard Klein, Pheng-Ann Heng: Mixed reality based respiratory liver tumor puncture navigation. *Computational Visual Media* 5(4): 363-374 (2019). doi: 10.1007/s41095-019-0156-x
- **Ruotong Li**, Yuqi Tong, Tianpei Yang, Jianxi Guo, Weixin Si, Yanfang Zhang, Reinhard Klein, Pheng-Ann Heng: Towards Quantitative and Intuitive Percutaneous Tumor Puncture via Augmented Virtual Reality. *Computerized Medical Imaging and Graphics*, 90(2021): 101905, ISSN 0895-6111, doi: 10.1016/j.compmedimag.2021.101905

Other publications that are not involved in this thesis are listed below:

- **Ruotong Li**, Weixin Si, Michael Weinmann, Reinhard Klein: Constraint-Based Optimized Human Skeleton Extraction from Single-Depth Camera. *Sensors*. 2019;19(11):2604. Published 2019 Jun 7. doi:10.3390/s19112604
- **R. Li**, W. Si, J. Guo, Y. Zhang, R. Klein, P. A. Heng: Constraint-based optimal needle path planning with 3D signed distance field fusion. *CARS 2020. Computer Assisted Radiology and Surgery Proceedings of the 34th International Congress and Exhibition. Int J CARS* 15, S117 (2020). doi:10.1007/s11548-020-02171-6
- Y. Shi, Y. Tong, **R. Li** and W. Si: Internal Motion Estimation during Free-Breathing via External/Internal Correlation Model, 2021 IEEE International Conference on Real-time Computing and Robotics (RCAR), 2021, pp. 986-990, doi:10.1109/RCAR52367.2021.9517379

- Yangyang Shi, Xuesong Deng, Yuqi Tong, **Ruotong Li**, Yanfang Zhang, Lijie Ren, Weixin Si: Synergistic Digital Twin and Holographic Augmented-Reality-Guided Percutaneous Puncture of Respiratory Liver Tumor, in IEEE Transactions on Human-Machine Systems, vol. 52, no. 6, pp. 1364-1374, Dec. 2022, doi: 10.1109/THMS.2022.3185089.

This thesis is organized in four parts. The introduction Part I gives the background and preliminaries of the augmented reality guided minimal invasive liver tumor treatment. This part reviews the related work in this research domain. This is following by the parts for solving the key challenges in this scope:

- Part II is given by the paper [Li et al., 2021a], and provides a solution for tumor puncture planning, especially when multiple electrodes are needed for a complete ablation of the tumor.
- Part III involves the content of the papers [Li et al., 2019a] and [Li et al., 2019b]. Both publications focus on predicting the dynamic movement of the target while performing the ablation puncture, thus increasing the precision of the liver tumor puncture.
- Part IV is given by the paper [Li et al., 2021b], and discusses how the augmented virtual navigation system supports doctors on applying the tumor puncture precisely and efficiently.

Part V summarizes this thesis, explains the significance of the research and points out potential future work. Part II, III and IV includes the full text of my first-author articles with a corresponding summary in front of each.

Part II

Multi-constrained surgical planning for liver tumor ablation

Surgical Planning for Ablation Surgery

Versatile Multi-constrained Planning for Thermal Ablation of Large Liver Tumors

High-quality surgical planning is the first step toward achieving precise treatment. Thermal ablation is the minimal invasive treatment for small and slightly large tumors with the diameter no larger than 5cm. It is considered the first-line treatment for small hepatocellular carcinomas with diameter smaller than 3cm and benign tumors in the liver [Knavel and Brace, 2013].

According to the Retrospective studies on the medical record of thermal ablation surgery, either incomplete ablation or too large tissue damage will cause severe complication [Livraghi et al., 2003, Liang et al., 2009]. Thus, the principle of a precision ablation treatment is complete coverage of the tumor region with the least healthy tissue damage. Since the effect region of an ablation needle is limited, careful pre-operative planning is even more significant in the large tumor thermal ablation which needs multiple needles working together. For ensuring the treatment requirement, this work takes both the medical constraints for ablation and the geometry constraints for optimizing the needle trajectory into consideration.

In this chapter, we proposed the method for helping doctors plan the thermal ablation with a computer-assisted modality. In this work, both RFA and MWA for liver tumor treatment are taken into consideration. The planning starts with patient-specific target anatomical structure reconstruction and treatment region determination. For each treatment zone, our algorithm first gives the suggestion of initial needle configuration. Then the algorithm computes the needle target distribution that can best cover the treatment region while giving less tissue damage in the surrounding area. In this step, the medical constraints are involved to ensure the result fulfills the cure requirement. The needle insertion trajectory is then computed with the geometry constraints that extracts from the expert consensus. In this way, the final planning achieves treatment purpose with convenient performance. Our method gives the option for doctors to interfere with the procedure in any step, in order to get planning that matches the specific situation for each patient and their personal operation preference.

The proposed algorithm is validated on the medical data provided by The First Affiliated Hospital, Sun Yat-sen University. Compared with the planning given by the doctors, the simulated ablation region of our planning result allows a reliable coverage of the tumor zone and an adjustable safety margin while causing as little damage as possible to healthy tissue. Our method incorporates medical constraints in the automatic optimization approach for the needle insertion trajectory from the percutaneous puncture position to the needle target position. The optimized trajectory proves that our approach can achieve the optimal planning of multi-electrode thermal ablation while reducing the dependence on clinicians' experience. The result of the experiment shows that our approach outperforms the state of the art by achieving a complete tumor ablation with reduced damage to healthy tissue. At the same time, it increases the clinical applicability due to the use of medical constraints. In addition, it also enhances the feasibility of the proposed method.

The content of this chapter is published in the peer-reviewed journal *Computerized Medical Imaging and Graphics*:

Ruotong Li, Yangyang Shi, Weixin Si, Li Huang, Bowen Zhuang, Michael Weinmann, Reinhard Klein, Pheng-Ann Heng: Versatile Multi-constrained Planning for Thermal Ablation of Large Liver Tumors. *Computerized Medical Imaging and Graphics*, 94(2021): 101993 <https://doi.org/10.1016/j.compmedimag.2021.101993>

The First Affiliated Hospital, Sun Yat-sen University provides the medical data used in this article. Li Huang and Bowen Zhuang are responsible for medical image labeling and medical knowledge consulting.

Contribution of the thesis author: Conceptualization, Methodology, literature review, algorithm implementation and validation, results interpretation and visualization, manuscript composition, validation experiment design.

Abstract

The surgical planning of large hepatic tumor ablation remains a challenging task that relies on fulfilling multiple medical constraints, especially for the ablation based on configurations of multiple electrodes. The placement of the electrodes to completely ablate the tumor as well as their insertion trajectory to their final position have to be planned to cause as little damage to healthy anatomical structures as possible to allow a fast rehabilitation. In this paper, we present a novel, versatile approach for the computer-assisted planning of multi-electrode thermal ablation of large liver tumors based on pre-operative CT data with semantic annotations. This involves both the specification of the number of required electrodes and their distribution to adequately ablate the tumor region without damaging too much healthy

tissue. To determine the insertion trajectory of the electrodes to their final position, we additionally incorporate a series of medical constraints into our optimization, which allows a global analysis where obstacles such as bones are taken into account and damage to healthy tissue is mitigated. Compared with the state-of-the-art method, our method achieves compact ablation regions without relying on assumptions on a potential needle path for optimal global search and, hence, is suitable for guiding clinicians through the planning of the tumor ablation. We also demonstrate the feasibility of our approach in various experiments of clinical data and demonstrate that our approach not only allows completely ablating the tumor region but also reducing the damage of healthy tissue in comparison to the previous state-of-the-art method.

keyword: Computer-assisted ablation planning; multiple medical constraints; large liver tumor; versatile strategy

2.1 Introduction

Hepatic tumors is one of the most common types of cancer [World Health Organization, 2021]. Due to its potential of allowing a fast rehabilitation, minimal invasive surgery methods such as radiofrequency ablation (RFA) and microwave ablation (MWA) approaches have become particularly popular for hepatic tumor treatment nowadays [Salati et al., 2017]. The thermal ablation of large liver tumors is performed via inserting one or multiple radiofrequency probes (in RFA) or electrodes (in MWA) into the tumor, heating the tumor tissue to the temperature of 60° C and, thereby, killing the cancer cells [Minami and Kudo, 2013, Simon et al., 2005]. Therefore, precise pre-operative planning is the key factor for the successful ablation of cancer tumors. This planning includes the definition of the treatment zone, the planning of the respective electrode placement as well as the respective insertion paths' trajectory (shown in Fig 2.1). When an electrode performs the tumor ablation, its heat transfer according to the bio-heat equation in the different tissue depends on the local fat and water deposits [Emery and Sekins, 1982, Giering et al., 1995]. Except for the heat transport within the tissue, nearby blood vessels induce an additional cooling described by the heat-sink effect [Crezee and Lagendijk, 1992]. In order to completely ablate the cancer cells and the infiltrated tissue, the treatment zone is defined as the volume of the tumor region as well as a safety margin around it. In particular for large contact-with-vessel hepatocellular carcinoma, the risk of intrahepatic recurrence after RFA treatment is higher when the ablation has insufficient safety margins [Choi et al., 2001, sun Kim et al., 2006]. According to expert consensus, 5 mm is an adequate value to define the safety margin around

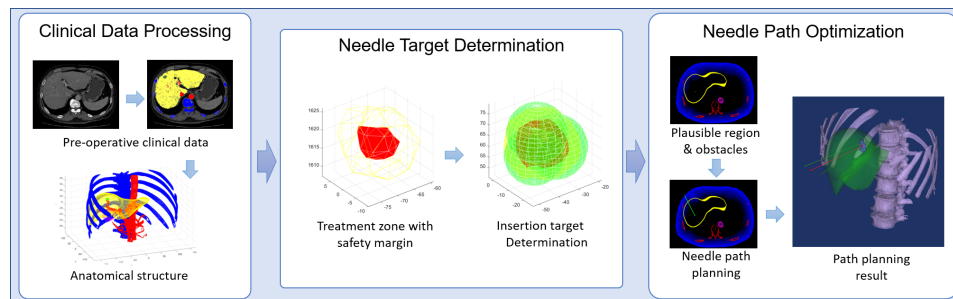


Figure 2.1: Illustration of the steps in our multi-constrained planning approach for the thermal ablation of large liver tumors. After extracting the anatomical structure from the pre-operative data, we first define the treatment zone with a safety margin and then determine the number of electrodes required for the surgery and the respectively desirable needle targets to allow an adequately fitting ablation region with respect to the tumor region and its surrounding safety margin. After that, we compute the needle path based on multiple constraints.

the tumor. However, the risk of damaging other vessels or organs has to be taken into account during the pre-operative planning. Hence, the safety margin should not exceed the liver. If the target tumor is too close to vessels, the treatment zone should be eroded to ensure that the treatment zone does not overlap with blood vessels [Chen et al., 2018a]. In case of large tumors, the treatment zone is specified by placing multiple electrodes [Chen et al., 2018b].

2.1.1 Related Work

To consider medical constraints provided by experts in the pre-operative planning, needle insertion can be formulated as a constraint-based optimization problem [Villard et al., 2005]. Here, the underlying goal is the optimization of both the final needle positions for an adequate ablation and the needle insertion points on the skin so that needles can be safely inserted to the tumor while damaging as little healthy tissue as possible.

In addition to the placement of the needles to allow for an adequate ablation of the tumor, this optimization strategy also needs to include a respective path planning from the respectively suitable needle insertion point to the target location at the tumor to prevent damaging other critical structures in the abdomen including gallbladder, bile duct as well as large vessels in and around the liver and, hence, avoid complications in terms of injuring the bile duct or intestinal perforation [Livraghi et al., 2003, Liang et al., 2009]. In the traditional image-guided RFA and MWA, this pre-operative needle trajectory planning process is based on 2D medical images, like computed

tomography (CT) and magnetic resonance imaging (MRI). Doctors then plan the insertion path based on their experience as well as according to the medical requirements and mark the insertion point in pre-operative CT images. However, 2D CT scanning cannot provide the intuitive patient-specific information, which severely impacts the surgical outcome and is greatly dependent on the doctors' experience. Instead, automatic approaches that directly exploit the given 3D information inherently allow a better planning of the needle path, and thereby offer a more useful tool for clinical pre-operative planning

Several investigations [Baegert et al., 2007a, Baegert et al., 2007b, Seitel et al., 2011b] focused on the respective optimization with weighted constraints. Baegert et al. [Baegert et al., 2007a] define four strict constraints, i.e. *lesion volume*, *insertion depth*, *critical distance* and *safe portion*, that have to be taken into account for planning insertion paths as well as three soft constraints (*whole tumor burnt*, *minimum damage* and *vital organs preserved*) that rate the quality of the candidate insertion path. Baegert et al. [Baegert et al., 2007b] use a multi-criteria method to optimize the needle path for RFA.

Similarly, Seitel et al. [Seitel et al., 2011b] defined hard constraints that specify medical requirements for determining the candidate insertion area on the skin, and then semi-automatically determine the trajectory by rating the candidate zone with the soft constraints, which uses the *pareto optimality* [Stadler, 1979] method for trajectory optimization. Except for those constraints stated by Baegert et al. [Baegert et al., 2007a], the *tangency constraint* [Baegert et al., 2007b] has been defined to ensure that the angle in which the trajectory intersects the skin and organ surface is larger than 20° . This work also included the development of a trajectory planning interface, with which doctors can interactively edit the planning result. Schumann et al. [Schumann et al., 2010] solved the placement of hepatic electrodes by selecting the optimal trajectory from the list of potential paths. These path proposals have been determined based on a weighted combination of cylindrical projections that represent individual path criteria. In further work, Altrogge et al. [Altrogge et al., 2006] discussed the placement of RFA probes via minimizing a temperature-based objective function. The work by Schumann et al. [Schumann et al., 2015] was inspired by their previous work [Schumann et al., 2010] and took the heat-sink affection into consideration.

However, all of the aforementioned studies only considered the ablation based on a single electrode. For large tumor regions (i.e. with a treatment zone with *diameter* $> 3cm$), multiple electrodes are required to cover the tumor and a multi-electrode based coverage of the region to be ablated has to be considered. For the planning of needle insertion paths in multi-electrode ablation scenarios, the converge of multiple ablation regions from the individual electrodes are taken into account. Chen et al. [Chen et al., 2018a]

proposed a constrained clustering method, which divides a large tumor into multiple ablation regions and then plans the puncture path with an semi-automatic process. This method allows manual adjustment when the planned path passes through large vessels or ribs. Inspired by the work by previous work [Liang et al., 2019b], Liang et al. [Liang et al., 2019a] proposed a method to automatically determine the planning of multiple needle insertion paths. The authors planned needle trajectories by adjusting the needle target inside the treatment region and the insertion position on the skin area. However, even though this more sophisticated method allows the fast computation of insertion paths, it cannot ensure a global optimization. Besides, this method considers only multiple ablation regions with the same size, which complicates achieving a global optimal planning.

Further work focused on achieving a complete tumor coverage by as few as possible spherical ablation regions as well as the optimization of needle insertion, where as many target positions as possible are passed per insertion and other anatomical constraints are taken into account, within a genetic optimization approach [Ren et al., 2013] or based on integer programming [Ren et al., 2014b]. Similar anatomically-inspired hard constraints have been used within a multi-objective optimization for ablation and path planning based on a multi-objective evolutionary algorithm to get a Pareto optimum [Li et al., 2020b]. The involved constraints penalize longer insertion depths, passing through long cavities as well as passing critical structures such as bones, large vessels and organs as well as deviations from the puncturing points to the target locations. However, several information needs to be provided by the user, which includes puncturings, puncturing order, and targets positions. The multi-objective planning by Liang et al. [Liang et al., 2019b, Liang et al., 2020] approaches a trade-off between the number of involved electrodes and the damage of surrounding healthy tissue under different clinical constraints, which is achieved based on an extended set cover-based model and Pareto optimization.

2.1.2 Contributions

In this paper, we propose a novel, versatile approach for the planning of thermal ablation of large liver tumors. For this purpose, we explore the use of pre-operative clinical data given by CT scans that have been segmented into the respective anatomical structures. We formulate the tumor ablation task as a constrained optimization problem that optimizes the placement of the set of involved electrodes with its spherical influence region to adequately cover the tumor region and its safety margin while mitigating damage to healthy tissue. In addition to the placement of the electrodes, we also optimize their insertion to the final position, where we take medical constraints such as the minimum insertion depth that is required to adequately anchor the electrode in the tissue when performing the ablation, close-to-orthogonal

insertion into the body or into organs as well a sufficiently large distance to bones and other critical anatomical structures into account. In contrast to previous work, our approach leverages constraints for avoiding too much overlap of the individual ablation zones, thereby improving the efficiency of the ablation, as well as for exceeding the maximal distance between electrodes in addition to constraints regarding tumor coverage, the reduction of ablating of healthy tissue. Our approach explicitly allows the optimization regarding a configuration of multiple target positions for the ablation and the respective insertion paths which renders our approach suitable for simultaneous ablation by different electrodes. We evaluate the benefits of our approach in a comparison to a representative state-of-the-art multi-objective planning approach and also analyze the real potential based on the feedback of medical experts. The constraints involved in our optimization are medically inspired and the different importance of the individual terms for the treatment of individual patients can be set by the doctors by increasing the weights for the respectively more important characteristics. Accordingly, our method has a high potential for guiding clinicians through the planning of the tumor ablation.

In summary, the main contributions of our work are:

- We present a novel multi-electrode planning method for thermal ablation of large liver tumors which allows a reliable coverage of the tumor zone and an adjustable safety margin while causing as little damage as possible to healthy tissue.
- By directly incorporating medical constraints into our automatic optimization approach for the needle insertion to the target position in terms of percutaneous puncture, our approach can achieve the optimal planning of multi-electrode planning for thermal ablation of large liver tumors, while reducing the dependence on clinicians' experience.
- Our approach outperforms the state-of-the-art by achieving a complete tumor ablation with a reduced damage to healthy tissue while increasing clinical applicability due to the use of medical constraints, which greatly enhances the feasibility of the proposed method.

2.2 Materials and Methods

Our pre-operative planning approach for the thermal ablation of liver tumors relies on the subtasks of i) finding an optimal configuration of electrode placements to completely ablate the tumor, which involves both the specification of the number of required electrodes and their placement, and ii) finding an optimal insertion path from the needle entry point to the final placement. All these tasks rely on the careful consideration of medical constraints. In the following, we provide details on these individual subtasks.

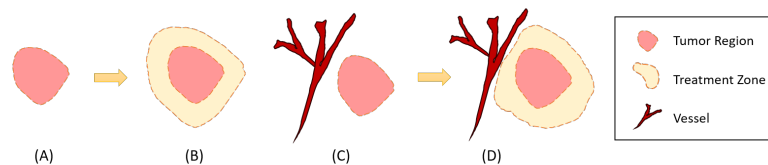


Figure 2.2: 2D illustration of the specification of the treatment zone. (A-B) Treatment zone (orange dashed line) determined by safety margin (yellow) around the tumor region (pink). (C-D) When there are vessels (dark red) in the vicinity of the tumor within the distance of θ_s , the treatment region (orange dashed line) has to be adjusted, so that the treatment region does not overlap with the vessels. Here, we depict the underlying idea in 2D, while our approach applies this concept in 3D.

2.2.1 Initial Tumor Segmentation

Our approach is applied to pre-operative medical data of hepatic carcinoma patients. In an initial step, we manually segment the anatomical structures based on their CT scans and reconstruct the 3D anatomical model in pre-operative medical data of hepatic carcinoma patients as shown in Fig. 2.5 to detect the location of the tumor and the critical anatomical structures nearby.

2.2.2 Finding an Optimal Electrode Configuration for Thermal Ablation

To allow a successful thermal ablation of a liver tumor while exposing patients to as little stress as possible, a proper treatment zone must ensure that the complete tumor will be destroyed with a minimum of damage to the healthy tissues in the patient's abdomen. For this purpose, we propose a two-step approach to define the treatment zone (see Fig. 2.2). First, we specify the tumor region with an additional safety margin θ_s , which is followed by the adjustment of the region to avoid overlaps with other critical regions within the abdomen including the gallbladder and the main vessels inside and around the liver and damaging these structures respectively. To allow a more save and efficient RFA process, doctors usually inject artificial ascite around the liver instead of adjusting the shape and size of the treatment zone. In addition, the planned treatment zone should not overlap the vessel in order to avoid the heat sink effect. In practice, large vessels too close to or superimposed with the tumor need to be blocked before applying thermal ablation.

Specification of the Ablation Region

The ablation region around an electrode is typically specified in terms of a sphere with radius r , which is influenced by the thermal energy and time of the ablation process. However, instead of carefully specifying both ablation energy and time, doctors in practice follow the instructions provided by the ablation systems and set the corresponding energy and time for each of the electrode so that the effect radius of the electrode will fulfill certain requirements. As the ablation radius for today’s out-off-shelf ablation needles heavily depends on the used needle type, our planning approach allows doctors to specify the range $[r_{min}, r_{max}]$ of the radius r of the ablated region.

In case an ablation surgery requires using multiple electrodes, the influence of the heat distribution among the electrodes has to be taken into account as well. Therefore, a validation of the ablation region on the isolated liver is highly recommended to ensure that the merged ablation region fulfills the treatment’s requirements. We will show an experiment regarding the validation of an ablation region in Sec. 2.3.1.

Initialization of the Number of Required Electrodes

With our approach, we aim at an automatic initialization of the involved electrodes’ placement. The number and position of needle targets are determined based on the ablation radii r_i of the electrodes and the shape of the treatment region. In order to mitigate damaging healthy tissue, doctors usually choose the least number of electrodes that cover the entire treatment area. Due to the variations of the radii according to $r_i \in [r_{min}, r_{max}]$, there may be multiple configurations with different numbers N of electrodes with $N \in [N_{min}, N_{max}]$.

Finding the minimum number N_{min} of required electrodes can be formulated as a sphere packing problem. Approximating the region affected by the electrodes in terms of non-overlapping spheres would lead to an estimate of the lower bound of the number of required electrodes according to

$$N_{min} = V_{Tzone} coverage / \left(\frac{4}{3} \pi r_i^3 \right) \quad (2.1)$$

where V_{Tzone} represents the volume of the treatment region, coverage denotes the ratio of the volume that can be covered with non-overlapping spheres and r_i determines the region size influenced by the i -th single electrode. It is well-known that the cubic close packing (FCC) and the hexagonal close packing (HCP), which both cover approximately 74% (i.e. $coverage = 74\%$) of the volume, providing the highest coverage among all possible lattice packings [Gauß, 1876]. We discretize the volume V_{Tzone} occupied by the treatment zone as a set of voxels $\{v_{x,y,z}\}$ and treat the voxel midpoints as points in three-dimensional space, i.e. a point set M . Here, we leverage the resolution of the original CT scans (shown in Fig. 2.5) to

specify the voxel sizes and their position. Then, we compute the variance of the voxel midpoints. Then, we compute the variance of these points on the principal axes by applying principle component analysis (PCA) to the point set M . The number of electrodes N for covering the treatment zone should fulfill the following inequalities:

$$\begin{aligned} Nr_i &> \max(\sigma_1, \sigma_2, \sigma_3) \\ N_{max} &< \text{sum}(\sigma_1, \sigma_2, \sigma_3)/r_{min} \end{aligned} \quad (2.2)$$

where σ_1, σ_2 and σ_3 denote the largest variance along the principle directions. The intuition behind is that non-overlapping spherical regions are aligned to cover the 2σ -region of the data (we already removed the factor 2 on both sides from the aforementioned equation) to cover 95.4% of the variance of the data. Therefore, we get the initial number of electrodes based on the inequalities 2.2 and 2.1.

2.2.3 Medical-constraint-based Determination of Needle Target Positions

After the number of required electrodes has been determined, we optimize the needle target locations for the electrodes. For this purpose, we recursively update the target positions p_i and the corresponding radii r_i of influence until we cover the entire treatment zone with the smallest overlap with each other and least damage to the surrounding tissues.

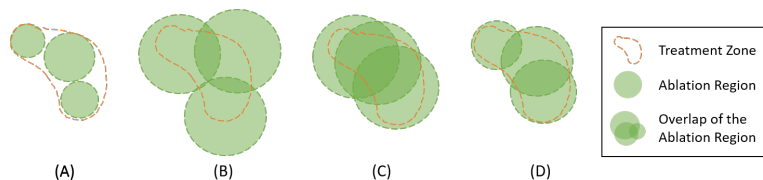


Figure 2.3: 2D illustration of the effects of different needle positions and ablation radii. For a simpler, more intuitive illustration, we depict the underlying idea in 2D, while our approach applies this concept in 3D. (A-D) Different target planning examples for the same treatment zone (region of orange dash line). (A) When the ablation radius of the electrodes is set too small, they cannot cover the total treatment zone, i.e. $C_{cover} < 1$, $C_{treat} < 1$. (B) While using too large ablation radii will cause larger damage to the surrounding tissue, i.e. C_{damage} is high, and (C) large overlaps of the ablation region result in a waste of time and energy, i.e. too large $C_{overlap}$, (D) a reasonable needle configuration should completely cover the treatment region with ablation regions and avoid causing damage to healthy tissue as much as possible.

For the ablation based on N electrodes, we compute the ablation region of each electrode with its ablation radius r_i

$$V_{Ezone}^i = \{x | (x - p_i)^2 \leq r_i^2\} \quad \text{for } i \in [1, N] \quad (2.3)$$

Thus, the total ablation region V_{Ezone} covered by these N electrodes can be represented as the union of the individual electrodes' ablation regions, i.e.

$$V_{Ezone} = V_{Ezone}^1 \cup V_{Ezone}^2 \cup \dots \cup V_{Ezone}^N. \quad (2.4)$$

In order to quantify medical constraints, we define the ratios C_{cover} , C_{treat} , $C_{overlap}$ and C_{damage} to evaluate the quality of the electrode target placement according to

$$C_{cover} = \frac{V_{tumor} \cap V_{Ezone}}{V_{tumor}} \quad (2.5)$$

$$C_{treat} = \frac{V_{Tzone} \cap V_{Ezone}}{V_{Tzone}} \quad (2.6)$$

$$C_{damage} = \frac{V_{Ezone}/V_{Tzone}}{V_{Ezone}} \quad (2.7)$$

$$C_{overlap} = \frac{V_{Ezone}^1 \cap V_{Ezone}^2 \cap \dots \cap V_{Ezone}^N}{V_{Ezone}} \quad (2.8)$$

where C_{cover} and C_{treat} denote the percentage of the ablated target tumor region and the coverage ratio with respect to the treatment zone including its safety margin respectively. Note that a proper surgical planning for successful tumor ablation has to ensure $C_{cover} = 1$, i.e. the complete tumor needs to be covered by the individual electrodes' ablation regions in order to achieve a complete ablation. In addition, the value of C_{treat} should be as large as possible to also adequately cover the safety margin and, hence, achieve a clean ablation. The ratio C_{damage} represents the region of healthy tissue ablated by the electrodes in comparison to the target tumor region, and $C_{overlap}$ denotes the redundancy of the ablation region. For a well-planned ablation surgery, the values of C_{damage} and $C_{overlap}$ should be as low as possible to avoid damaging healthy tissue and to lower redundancy. An illustration of these quantities is given in Fig. 2.3. We can easily compute the values of these individual regions based on Monte-Carlo integration. Following this numeric integration approach, we approximate the volume of a 3D region given in terms of the multi-dimensional integral $\int_{\Omega} f(\bar{\mathbf{x}}) d\bar{\mathbf{x}}$ based on the volume $V = \int_{\Omega} d\bar{\mathbf{x}}$ of the globally considered subset $\Omega \subset \mathcal{R}^3$ and setting the values of an indicator function to one for (regularly sampled) midpoints \bar{x}_i of the voxels in the respective sub-region $\Omega_S \subset \Omega$, i.e.

$$f_{\Omega_S}(\mathbf{x}) = \begin{cases} 1 & \text{if } \mathbf{x} \in \Omega_S \\ 0 & \text{if } \mathbf{x} \notin \Omega_S \end{cases},$$

and computing the searched volume according to $V \frac{1}{N} \sum_{i=1}^N f_{\Omega_S}(\bar{\mathbf{x}})$.

Besides the aforementioned quantities to measure the coverage of the tumor and treatment zones, the relative amount of damaged healthy tissue and the redundancy, we also add a distance constraint C_{tDis} for the final needle configuration that enforces the electrode targets to not be more distant than the maximum distance, i.e.

$$C_{tDis}(p_1, \dots, p_n) = \frac{1}{1 + e^{-k(\max(d(p_i, p_j)) - \theta_{nee})}} \quad (2.9)$$

where θ_{nee} denotes the maximum distance between the electrode targets p_1, \dots, p_n and k is a control parameter to steer the slope of the logistic function $C_{tDis}(p_1, \dots, p_n)$ where we set $k=2$.

Based on all these individual penalties, we define a energy function E_{Med} that combines the medical constraints:

$$E_{Med} = w_0(1 - C_{cover}) + w_1(1 - C_{treat}) + w_2C_{damage} + w_3C_{overlap} + w_4(C_{tDis}) \quad (2.10)$$

where the parameters w_0, w_1, w_2, w_3 and w_4 denote the weights of the corresponding constraints $C_{cover}, C_{treat}, C_{damage}, C_{overlap}$ and C_{tDis} . Finding the proper positions for the individual needle targets then corresponds to minimizing E_{Med} . As shown in Alg. 1, P and R respectively denote the centers and radii of the spherical ablation regions in 3D space. In our method the positions and radii are initialized randomly, while in every iteration we update the positions and radii only if the energy decreases. In our implementation, the minimization function we used in Alg. 1 is the ‘‘interior-point’’ method [Byrd et al., 1999, Byrd et al., 2000, Waltz et al., 2006].

2.2.4 Constraint-based Optimization of Needle Insertion Paths

After the computation of suitable needle target locations that allow a suitable ablation of the tumor, we have to optimize the the insertion paths $P_i = \overrightarrow{q_i p_i}$ for the i involved electrodes ($i = 1, \dots, N$) from their insertion points q_i on the skin to their corresponding target locations p_i . Here, we have to consider constraints imposed by surrounding structures like bones, tissue, other organs or vessels as well as inadequate electrode insertion based on crossing insertion paths to keep the caused damage as low as possible. For this purpose, we formulate the task of computing the insertion paths in terms of an energy optimization of the energy function E_{Geo} with

$$E_{Geo} = \Lambda_1 \sum_{i=1}^n E_{single,i} + \Lambda_2 E_{multi} \quad (2.11)$$

Input: Electrode number N , Shape of treatment zone S_{Tz}
Output: Electrode positions $\mathbf{P} = [p_1, p_2, \dots, p_N]$, Radii of individual electrodes' ablation region $\mathbf{R} = [r_1, r_2, \dots, r_N]$
Start:
Initialize \mathbf{P} with N random position in S_{Tz} ;
Initialize \mathbf{R} with r_{max} ;
Compute $E_{Med,0}$ with \mathbf{P}, \mathbf{R} ;
Sample $\mathbf{P}_{temp}, \mathbf{R}_{temp}$ around \mathbf{P}, \mathbf{R} ;
while not having reached the maximum number of iterations **do**
 Compute $E_{Med,temp}$ with $\mathbf{P}_{temp}, \mathbf{R}_{temp}$;
 if $E_{Med,temp} < E_{Med,0}$ **then**
 Update \mathbf{P}, \mathbf{R} with $\mathbf{P}_{temp}, \mathbf{R}_{temp}$;
 Update $E_{Med,0}$ with $E_{Med,temp}$;
 end
 Update $\mathbf{P}_{temp}, \mathbf{R}_{temp}$ by sampling around \mathbf{P}, \mathbf{R} ;
end

Algorithm 1: Optimization of needle target locations

where $E_{single,i}$ denotes the cost of inserting electrode i to its target location and E_{multi} denotes the relevance of the configuration of multiple electrodes with respect to each other. We estimate the insertion paths by minimizing E_{Geo} .

Optimizing the Insertion Paths of Single Electrodes

Each electrode is inserted on a position q_i on the skin from where it is guided to a the corresponding target p_i . In the following, we formulate the cost of each of the insertion paths $\overrightarrow{q_i p_i}$ in terms of a geometric constraint E_{single} , which is defined as

$$E_{single} = v_1 E_{plaus} + v_2 E_{obs} + v_3 E_{len} + v_4 E_{dir}, \quad (2.12)$$

where v_1, v_2, v_3 and v_4 are the weights for $E_{plaus}, E_{obs}, E_{len}$ and E_{dir} , which penalize different aspects as also illustrated in Fig. 2.4.

To ensure that the insertion is as safe as possible, we label regions through which the electrodes can pass as *plausible*. Respective regions include regions not occupied by bones or other critical organs. Structures such as bones or critical structures like organs or vessels, where the electrodes cannot be passed inserted, in turn, are labeled as *not plausible* or *obstacle* respectively. We then compute the signed distance field for the abdomen region, so that regions with positive value denote *plausible* regions and regions with negative value denote *obstacle* regions. We combine these hard constraints in the energy E_{plaus} , where we set $E_{plaus} = \infty$ for regions

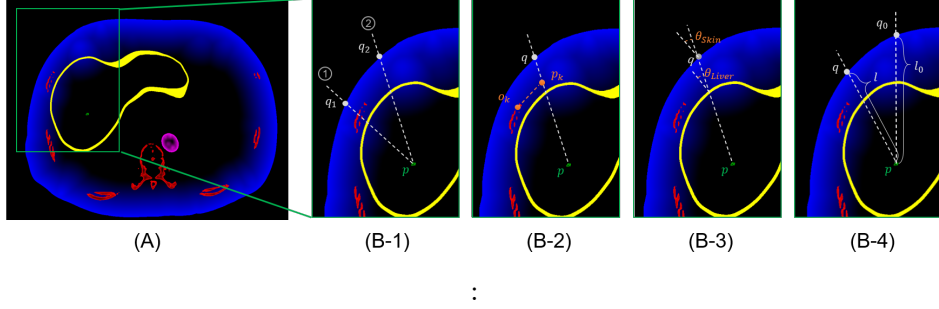


Figure 2.4: 2D illustration of the different types of constraints we used for the optimization of insertion paths of individual electrodes. (A) shows the border of anatomical structure on the axial plane of the patient abdomen with colors (Red: bones (ribs and spine), Yellow: liver boundary, Magenta: vessel, Green: tumor in the liver). (B-1) illustrates E_{plaus} the path \vec{pq}_1 shows an example for $E_{plaus} = \infty$, the path 2 shows an example of $E_{plaus} = 0$. (B-2) illustrates E_{obs} : position p_k is a point on path \vec{pq} and the position o_k is the point on the nearest obstacle. (B-3) illustrates E_{dir} and (B-4) shows E_{len} . Here, we depict the underlying idea in the 2D axial plane of the abdominal region for illustration purposes, while our approach applies this concept in 3D.

where we cannot let the needle pass through and $E_{plaus} = 0$ for regions where the needle can be passed through.

Furthermore, E_{obs} encourages insertion paths being more distant to *obstacle* regions, i.e.:

$$E_{obs} = Dist(p, q) / \sum^k Dist(p_k, o_k), \quad p_k \text{ is on } P \quad (2.13)$$

where p_k denotes the position of a discrete point on the insertion path and o_k denotes the respectively closest point on the nearest obstacle.

In addition, E_{len} penalizes insertion paths with a larger insertion depth and ensures the paths to be larger than the minimum insertion depth θ_{nee} :

$$\begin{aligned} E_{len} &= (Dist(p, q) - l_0) / l_0, \text{ when } Dist(p, q) \geq \theta_{depth} \\ E_{len} &= 100 * l_0 / Dist(p, q), \text{ when } Dist(p, q) < \theta_{depth} \end{aligned} \quad (2.14)$$

where l_0 denotes the length of the initial insertion (i.e. the point on the skin where an orthogonal insertion would lead to the respective target position) and θ_{depth} denotes the minimum length that has to be met in order to sufficiently anchor the electrode in the tissue while performing the ablation.

Finally, E_{dir} , which is specified as

$$E_{dir} = (1 - \cos \theta_{skin}) + (1 - \cos \theta_{liver}), \quad (2.15)$$

penalizes insertion paths according to their insertion direction on the skin and the liver surface, where θ_{skin} denotes the angle of the insertion path and the normal direction at the insertion point on the skin and θ_{liver} denotes the angle between the insertion path and the normal direction at the insertion point on liver surface. These two angles should be as small as possible to ensure that the needle can properly pierce into the tissue without slipping.

Additional Constraints in the Presence of Multiple Electrodes

The ablation of large tumors involves multiple electrodes. For their insertion into the respective target location, additional constraints have to be met as e.g. the insertion paths should not inter-cross or be too close to each other to ensure that the surgery can be performed in a convenient manner. Besides, according to doctors' experience, the surgery can be performed easier when the electrodes have a similar insertion direction.

We define E_{dist} and E_{para} to constrain the configurations of multiple insertion paths for multiple electrodes according to

$$E_{multi} = u_1 E_{dist} + u_2 E_{para}, \quad (2.16)$$

where E_{dist} denotes the distance between any of the two electrodes of the planning and E_{para} denotes their relevant direction between the planned paths, thereby awarding insertion paths with similar direction that are easier to handle for the doctor performing the percutaneous insertion. u_1 and u_2 are weights for E_{dist} and E_{para} .

E_{dist} as defined by

$$E_{dist} = \frac{Dist(p_i, p_j)}{\min(Dist(p_{i,k}, p_{j,k}))} \quad (2.17)$$

penalizes configurations where electrodes have a distance smaller than the target distance from each other, while E_{para} with

$$E_{para} = 1 / \left(\prod_{\substack{1 \leq i, j \leq N \\ i, j}} 1 + \frac{P_i \cdot P_j}{\|P_i\| \cdot \|P_j\|} \right) \quad (2.18)$$

awards the treatment planning with electrodes having similar directions, where P_i and P_j denotes a pair of insertion paths. Here, $p_{i,k}$ denotes a point on the insertion path P_i and $p_{j,k}$ denotes its nearest point on the insertion path P_j . $Dist(p_i, p_j)$ denotes the distance of the electrode tips of paths i and j . The distance between insertion paths should at any position not be below the corresponding final tip distance, i.e. the smallest distance should exactly occur between the needles' target positions and the value of E_{dist} should always be smaller than 1. In Alg. 2 we provide pseudocode for the implementation of our needle insertion approach.

Input: Needle target: $\mathbf{P} = [p_1, p_2, \dots, p_N]$,
 Shape of the Liver, Skin and the Obstacles in abdomen:
 $S_{Liver}, S_{Skin}, S_{Obs}$
Output: Optimal puncture direction $\mathbf{D} = [\vec{d}_1, \vec{d}_2, \dots, \vec{d}_N]$
Start:
 Initialize insertion directions \mathbf{D}_0 within axial plane, perpendicular
 to the operation bed;
 Compute E_{Geo} with $\mathbf{P}_0, \mathbf{D}_0, S_{Liver}, S_{Skin}, S_{Obs}$;
 Sample \mathbf{D}_{temp} around \mathbf{D}_0 ;
while *not having reached the maximum number of iterations* **do**
 | Compute $E_{Geo,temp}$ with $\mathbf{P}, \mathbf{D}_{temp}, S_{Liver}, S_{Skin}, S_{Obs}$;
 | **if** $E_{Geo,temp} < E_{Geo,0}$ **then**
 | | $\mathbf{D} \leftarrow \mathbf{D}_{temp}$;
 | | $E_{Geo,0} \leftarrow E_{Geo,temp}$;
 | **end**
 | Update \mathbf{D}_{temp} by sampling around \mathbf{D} ;
end

Algorithm 2: Determination of needle insertion paths.

2.3 Results

2.3.1 Experimental Materials

The data we used in this paper is composed of the pre- and post-surgery 3D CT-scans of 5 different patients with hepatic tumors, including both male and female patients. The medical data is provided by The First Affiliated Hospital, Sun Yat-sen University. According to the expert consensus, both RFA and MWA are feasible for the treatment of tumors with a diameter up to 5cm. Therefore, all of the tumors involved in our dataset are no larger than 5cm. The size and the location of tumors according to Couinaud's segmentation [Couinaud, 1999] are listed in Figure 2.5. The anatomical structures of the five patients with organs are marked in different colors. All labels in this work are sketched by a senior clinician from The First Affiliated Hospital of the Sun Yan-sen University.

For RFA, we choose the common ablation needle Medtronic COOL-TIPTM [Medtronic, 2020] RFA single electrode for our pre-operative planning. We can see from the user manual that the needle ACT2030 has an effect region with diameter $d = 30 \pm 5mm$ while the needle ACT2020 has an effect region with diameter $d = 20 \pm 3mm$. The shape of the ablation region around an electrode depends on the electrode type, the used energy, the heating time as well as the surrounding tissue characteristics. Compared with RFA, MWA gives an anisotropic ablation region, i.e. when the ablation energy or ablation time increase, the ablation region grows faster

along the electrode direction in comparison to the perpendicular direction with respect to the electrode. To validate the ablation radius of the MWA electrode, we employed an isolated bovine liver model as experimental material. The doctor inserts the ablation needle into the liver, applies ablation with different energy and time and observes the created ablation zone. Here the used ablation energy and time to achieve a certain ablation region are determined based on the doctors' experience and the effect region of the microwave ablation needle varies from $r = 12mm$ to $r = 21mm$ (see Fig. 2.7). Thus, in our experiments, we used the effective radius $r \in [r_{min}, r_{max}]$ with $r_{min} = 8.5mm$ and $r_{max} = 21mm$.

2.3.2 Result

Our method first determines the treatment zone and then computes the range of the number of electrodes required for completely ablating the cancerous area. After that, the method computes the candidate planning results for the electrode target and the trajectory path. Doctors can select the target combination and trajectory path they prefer for performing the surgery.

The needle target position optimization implemented via Matlab and the optimization of the needle insertion paths is implemented via C++. We design this planning algorithm as an independent module, so libraries like VTK, ITK, etc. are not involved in the present development.

Electrode Placement Initialization

The determination of the electrode target is based on the optimization of medical constraints. We first determine the treatment zone of the target tumor. Then, we select the number of electrodes with the method described in Sec. 2.2.2. After that, our method initializes the position of the needle targets randomly around the principal axis.

The size and shape of the treatment zone depends on the tumor location. In our experiments, the safety margin is set to the value of 5mm according to the consensus by experts in literature. Fig. 2.6 shows the treatment zone of our three clinical cases with a safety margin of $\theta_s = 5mm$.

Our algorithm is suitable for plannings with different numbers of electrodes, so that doctors can choose their preferred insertion for applying the surgery. In Sec. 2.2.2, the determination of the needle number sometimes may lead to multiple solutions. For example, for the medical cases 3-1 and 3-2, the number of required electrodes via our approach varies from 2 to 4 and 1 to 3 respectively. However, in practical situations, ablations with more than three electrodes are rare, while ablations with more than four electrodes are not recommend in the expert consensus. Therefore, our algorithm suggests the surgeon to consider the planning with no more than four needles.

As shown in Tab. 2.1, even though this planning leads to different numbers of electrodes, all of these pre-planned electrode target combinations have 100% coverage rate of the tumor region together with over 96% ablation rate of the region inside the safety margin. The result also shows that the planning with different needles causes different coverage rates of the cancerous and healthy tissue. Doctors can apply the algorithm and adjust the weights of the factors and choose a reasonable plan among the obtained results. We recommend doctors to choose the plan with the lowest damage to healthy tissue among the results fulfilling the medical requirements.

Needle Target Optimization and Determined Insertion Trajectories

The computation for the target position is performed with the method described in Sec. 2.2.3. In our experiment, the weights of the medical constraints are set to $w_0 = 1, w_1 = 3, w_2 = 1, w_3 = 1/3, w_4 = 1$.

The resulting needle electrode targets determined for each of the experimental cases are shown in Tab. 2.1. From the table we can see that all the plannings have an ablation radius inside the range of $[r_{min}, r_{max}]$ and the combined ablation zone completely covers the tumor region, i.e. $E_{cover} = 1$. Furthermore, over 96.9% of the safety margin is covered by the ablation region with only a damage rate of 26.3% on average.

For the tumors in the cases 2 and 3, plannings for multi-electrode based ablation are taken into consideration as well. The results show that both types of plannings can fulfill the treatment requirements. Thus, when the doctor decided to apply a single needle based ablation on these tumor cases, the electrode with a larger effect region is the preferable choice. The illustrations of the electrode target plannings are shown in Fig. 2.8 and Fig. 2.9.

The trajectory planning results are shown in Tab. 2.2. From the table we can see that all the trajectory planning results have an insertion depth l that is larger than the minimum insertion depth $\theta_{depth} = 50mm$ required so that the tissue can support the needle while applying the thermal ablation. Besides, according to the doctors' practical experience, the insertion is hard to process when the angle between the insertion path and the skin normal θ_{skin} and the angle between the insertion path and the liver surface normal θ_{liver} are larger than 60° . Therefore, all results in Tab. 2.2 fulfill the requirements encountered in practice.

For the geometry constraints we use for trajectory planning, we use the weights $v_1 = v_2 = v_3 = v_4 = 1$ and $u_1 = u_2 = 1$. The corresponding illustrations of the trajectory planning are shown in Fig. 2.8 and Fig. 2.9.

When the method leads to multiple results, we recommend doctors to choose the planning result that results in less damage to the patient, i.e. with a lower number of electrodes and lower C_{damage} among those plannings

Table 2.1: Resulting number of electrodes and ablation regions.

Case	Plan	Ablation radius (mm)	NeeNr	$C_{cover}, C_{treat}, C_{damage}, C_{overlap}$
1	1	r1 = 10.93	1	100%, 98%, 51%, 0%
2	2	r1 = 12.97	1	100%, 97%, 21%, 0%
	3	r1=11.20 r2=10.60	2	100%, 92%, 9%, 31%
3-1	4	r1 =14.25, r2=14.51	2	100%, 97%, 21%, 27%
	5	r1 =13.76 r2=13.71, r3=13.29	3	100%, 98%, 25%, 39%
3-2	6	r1=16.04	1	100%, 98%, 32%, 0%
	7	r1=14.02, r2=13.43	2	100%, 95%, 24%, 30%
	8	r1=11.74, r2=11.88, r3=13.66	3	100%, 94%, 22%, 41%
4	9	r1=16.65, r2=17.12, r3=16.10, r4=16.87	4	100%, 100%, 27%, 41%
5	10	r1=16.92, r2=17.33, r3=17.98, r4=17.49	4	100%, 100%, 31%, 43%
AVG	-	-	-	100%, 96.9%, 26.3%, -

Plan: Index number of the planning result; NeeNr: number of used needles; C_{cover} the coverage rate of the tumor region, $C_{treat}, C_{damage}, C_{overlap}$ are the parameters specifying coverage of the treatment zone, the zone of damaged tissue and the involved redundancy as defined in Sec. 2.2.2. AVG: average $C_{cover}, C_{treat}, C_{damage}$ of our planning result. From the result we can see that all the plans covered the tumor region to 100% with $C_{treat} = 96.9%$ and $C_{damage} = 26.3%$ on average.

that fulfill the treatment requirements. In practice, the conditions may vary greatly for each patient, thus the constraints can have different priorities. Under these circumstances, we design a flexible optimization approach for doctors to adjust the weight of different constraints, which can help the doctor to design the most suitable plan for each patient. In the future work, with an increasing number of available patient data, we will explore the selection of optimal parameter configurations and for different cases.

Planning for Multiple Tumors

In many cases, the patient has more than one tumor inside the liver. For this type of special cases, our method addresses this issue from the following two perspectives:

If the tumors are adjacent to each other with a distance smaller than the safety margin, i.e. the treatment zone for the tumors are overlapping and form a single large treatment zone, we can directly apply the planning method for one large treatment zone.

When the tumors have a large distance from each other (like in case 3 in Fig. 2.5), our planning method should be applied in two steps. First, we apply the ablation target planning for each of the tumors to identify the target position and ablation radius of the electrodes. Then, we perform the trajectory planning for all the target positions together with our path optimization method. This way, we can ensure that the final result fulfills both the medical and geometric constraints.

Table 2.2: Results for trajectory planning.

Case	Plan	Depth (mm)	θ_{skin}	θ_{liver}
1	1	75.68	9.86°	18.88°
2	2	54.56	1.03°	19.54°
	3	52.36	5.05°	26.25°
		56.57	48.26°	22.28°
3-1	4	75.57	23.99°	35.56°
		80.01	12.24°	51.96°
	5	74.96	21.20°	36.72°
		80.65	21.75°	42.34°
		74.46	21.98°	47.36°
3-2	6	50.30	14.68°	30.43°
	7	60.12	2.12°	39.21°
		65.84	16.82°	35.77°
	8	59.79	44.02°	39.05°
		71.73	20.48°	34.89°
		68.58	20.11°	39.24°
4	9	52.00	13.75°	4.45°
		50.00	25.76°	13.73°
		50.00	16.83°	14.84°
		50.43	27.18°	22.26°
5	10	50.00	25.90°	39.39°
		56.00	33.85°	51.42°
		50.00	30.23°	51.37°
		52.00	20.50°	32.48°
AVG	–	61.36	20.76°	32.58°

Case: index of medical cases; Plan: index of trajectory planning; Depth: insertion depth for each electrode; θ_{skin} : angle between the insertion direction and the normal direction on the skin at the insertion position. θ_{liver} : angle between the insertion direction and the normal direction on the liver surface at the insertion position. AVG: average of the Depth, θ_{skin} and θ_{liver} .

2.3.3 Multi-electrode Plannings

In order to evaluate our approach for the multi-electrode liver tumor ablation treatment planning, we compared the result with the clinical outcome shown in Fig. 2.10. Tab. 2.3 quantitatively compares results of our approach with the clinical outcomes, which illustrates that our planning results cause lower damage than the clinician’s experimental planning. The result shows that both of the plannings have an insertion depth larger than the minimum insertion depth θ_{depth} for supporting the electrode during the surgery and both θ_{liver} and θ_{skin} fulfill the requirements regarding practicability, which makes the puncture process comfortable for doctors.

Furthermore, Tab. 2.3 shows that our results have a shorter insertion depth and a lower ablation of healthy tissue, which causes less damage than the clinical result. We showed the results to the surgeons and they agreed that our method can generate a better path planning than the paths they had chosen based on their experience.

We also compared our method with the state-of-the-art method [Liang et al., 2019a]. We apply both methods on the multi-electrode planning case 3-1. The comparison of the planning results are shown in Tab. 2.4. As the approach by Liang et al. [Liang et al., 2019a] only considers the same effective radius for each of the RFA electrodes, the planning result leads to either an incomplete ablation or a higher damage, while our method can avoid this issue and finds a good trade-off.

Specifically, our method shows great flexibility in pre-operative planning from the following two perspectives: First, we allow the doctors to use the ablation needles from different ablation devices in the surgery, which allows a higher flexibility for surgical requirements. Second, our algorithm allows doctors to adjust the empirical coefficients, which can achieve the best fitting for the planned ablation region. In this regard, our algorithm can generate multiple results with different numbers of ablation electrodes, which allows surgeons to choose their preferences regarding the planning for the surgery.

From the data-driven nature of our method we can know that when multiple electrode based ablation is applied, the distance of the electrodes’ tip has an influence on the ablation region. Our algorithm presented in this paper considers only the situation that all the electrode tips work at the same time with a distance smaller than r_{max} to ensure that ablation regions of the electrodes are merged together without gaps. However in some practical cases, this procedure is not necessary. Therefore, our future work will improve this to achieve a more precise planning.

2.3.4 Computational Time

In the following, we report computation times for our (unoptimized) implementation for a system with portable computer (Thinkpad P14s with

Table 2.3: Comparison between our target planning and the manual planning performed by doctors.

Case	Plan	E_{cover}	E_{treat}	E_{damage}	$Depth(mm)$
1	1-our	100%	98%	51%	75.68
	Doc	100%	-	74%	73.74, 75.71
2	2-our	100%	97%	21%	54.56
	3-our	100%	92%	9%	52.36, 56.57
	Doc	96%	-	57%	59.44, 58.45
3-1	4-our	100%	97%	21%	75.57, 80.01
	5-our	100%	98%	25%	74.96, 80.64, 74.46
	Doc	99%	-	28%	78.51, 81.70
3-2	6-our	100%	98%	32%	50.30
	7-our	100%	95%	24%	60.12, 65.84
	8-our	100%	94%	22%	59.79, 71.73, 68.58
	Doc	100%	-	31%	53.96
4	9-our	100%	100%	27%	52, 50, 50, 50.43
	Doc	100%	-	42.38%	70.8, 86.9, 55.8, 61.9
5	10-our	100%	100%	31%	50, 56, 50, 52
	Doc	100%	-	36.46%	73.5, 65.6, 50.6, 58.5

Case: index of medical cases; Plan: index of trajectory planning, "Doc" denotes the planning extracted from the clinical outcome; E_{cover} : coverage rate of the tumor region; E_{treat} : coverage rate of the treatment zone inside the safety margin. E_{damage} : percentage of the healthy tissue that has been damaged inside the ablation region; $Depth$: insertion depth for each electrode.

Table 2.4: Comparison between our target planning result and the planning according to the method by Liang et al. [Liang et al., 2019a].

neeNr	Radius(mm)	E_{cover}	E_{treat}	E_{damage}	Method
2	r1=14.25, r2=14.51	100%	97%	21%	Ours
	r1=r2=10	99%	56%	0%	[Liang et al., 2019a]
	r1=r2=15	100%	97%	35%	[Liang et al., 2019a]
3	r1=13.76, r2=13.71, r3=13.29	100%	98%	25%	Ours
	r1=r2=r3=10	100%	69%	1%	[Liang et al., 2019a]
	r1=r2=r3=15	100%	99%	49%	[Liang et al., 2019a]

neeNr: number of involved electrodes; Radius: ablation radius of each electrode in the planning; E_{cover} : coverage rate of the tumor region; E_{treat} : ablation rate of the treatment zone inside the safety margin; E_{damage} : percentage of the healthy tissue that has been damaged inside the ablation region.

Intel(R) Core(TM)i7-10510U CPU, 8 core 1.80GHz, 16.0G RAM, NVIDIA Quadro P520).

The planning for an ablation with four needles takes 2 to 50 minutes for the optimization of the needle positions and no more than 3 minutes for optimizing of the insertion path. Considering that doctors have to prepare several days before the ablation treatment of large hepatic tumor, this processing time can fulfill the clinical requirement.

2.4 Discussion

We presented an automatic and versatile percutaneous puncture planning for thermal ablation of liver tumor. With the optimization of insertion target locations and insertion paths, our planning allows completely ablating the tumor region with a safety margin while causing less damage than the experimental clinical puncture paths. Besides, our algorithm offers a great flexibility for the doctors regarding the adjustment of empirical parameters for each step.

So far, our method only considered the configuration of multiple single-tip-electrodes that perform the thermal ablation simultaneously. Further strategies for thermal ablation surgery include the sequential ablation based on single-tip-electrodes or the ablation with cluster electrodes. While we did not focus on these strategies, our approach can also be adapted to the sequential ablation by adjusting the remaining treatment zone and the current needle position. As the RFA cluster electrode has a larger exposure than a single electrode, it is an alternative for the treatment of large tumors. Our ablation planning algorithm can be applied in this case by considering the cluster electrode as one single-tip needle with a large effect region. The needle target planning can therefore use the method in Sec. 2.2.3 and the needle path optimization method in Sec. 2.2.4 that are both still suitable for this case. In future work, with an increasing number of available patient data, we will explore the selection of optimal parameter configurations for different cases.

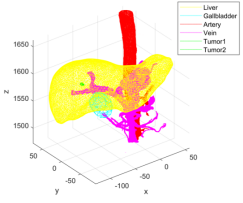
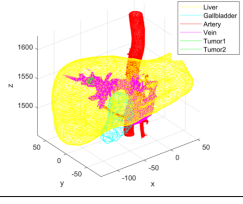
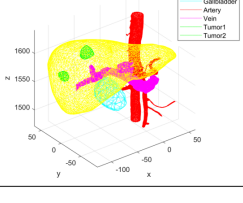
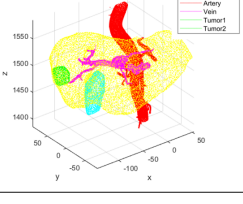
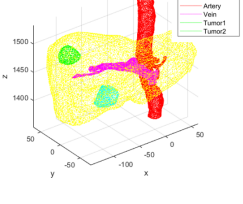
case	3D anatomical structure extracted from CT images	Tumor number	Tumor size (mm)	Tumor position	Image size (pixels)	Voxel size (mm)
1		1	[7.72, 9.13, 11.20]	VII	359 359 190	0.70 0.70 1.00
2		1	[17.84, 12.74, 15.20]	VIII	326 326 170	0.63 0.63 1.00
3		2	[21.42, 17.8, 19.20] [19.99, 20.70, 17.60]	IV, VI	365 365 170	0.71 0.71 1.00
4		1	[29.74, 26.90, 31.20]	VI	362 362 200	0.63 0.63 1.00
5		1	[28.56, 33.32, 28.00]	VIII	348 348 180	0.68 0.68 1.00

Figure 2.5: The anatomical structure of three clinical cases reconstructed from the medical data. (Case 1, 2, 4, 5) all have one tumor in the liver while (Case 3) has two tumors in the liver (Yellow: Liver; Cyan: Gallbladder; Red: Artery; Magenta: Vein; Green: Tumor). The size and position of the tumor according to Couinaud segmentation [Couinaud, 1999] are also listed.

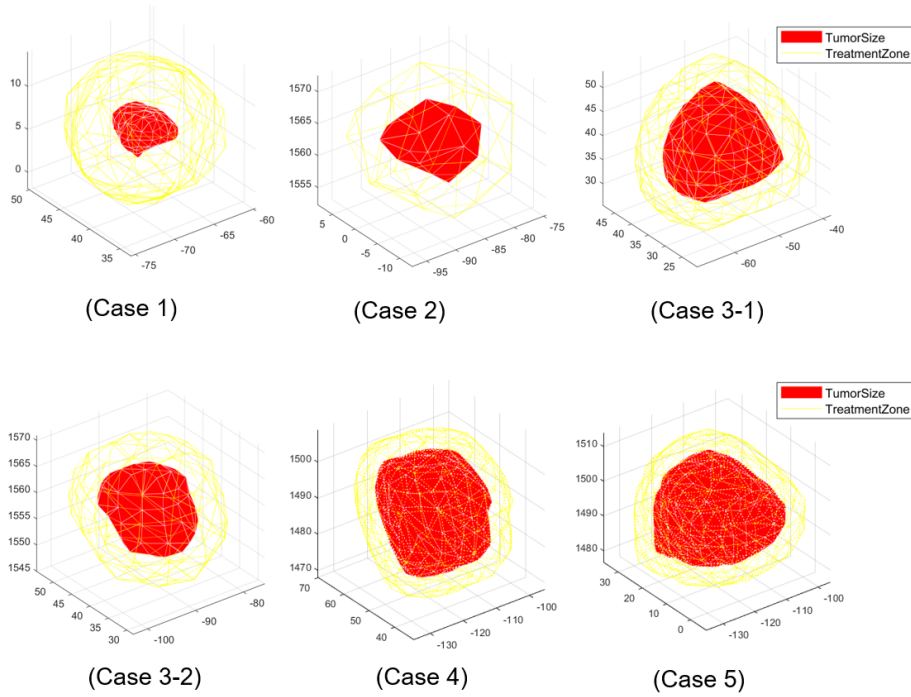


Figure 2.6: The treatment zone of the 4 tumors in the five medical cases shown in Fig. 2.5 with a safety margin of $\theta_s = 5mm$. Red: Region covered by the tumor; Yellow: Treatment zone for completely ablating the tumor. The units of the plot in this figure is mm.

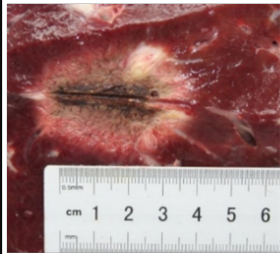
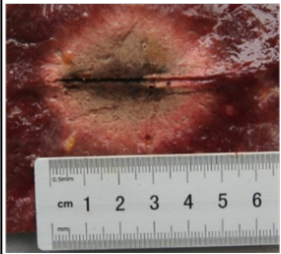

60W, 10min	60W, 15min	100W, 15min
		
d1=2.4, d2=4.4cm d1/d2: 0.5	d1=4.2, d2=4.6cm d1/d2: 0.9	d1=4.2, d2=6.5cm d1/d2: 0.65

Figure 2.7: MWA electrode ablation region validation on isolated bovine liver. The three images illustrate diameter of the microwave ablation needle when applying different ablation time and effect.

case	Plan	Target planning	Trajectory planning
1	1		
2	2		
2	3		
3-1	4		
3-1	5		

Figure 2.8: The needle target and trajectory planning result for the cases 1 to 3-1. The third column shows the tumor region (red), treatment zone of the tumor with a safety margin of $\theta_s = 5mm$ (yellow) and the ablation zone for each electrode tip (green sphere). The last column shows the corresponding trajectory planning for the insertion where different parts such as ribs/spine (blue), liver (yellow), artery (red), vein (magenta), gallbladder (cyan) and the tumor (black) are marked with different colors. The ablation zone for each electrode tip is marked with a green sphere and the insertion path trajectory is marked as a green line.

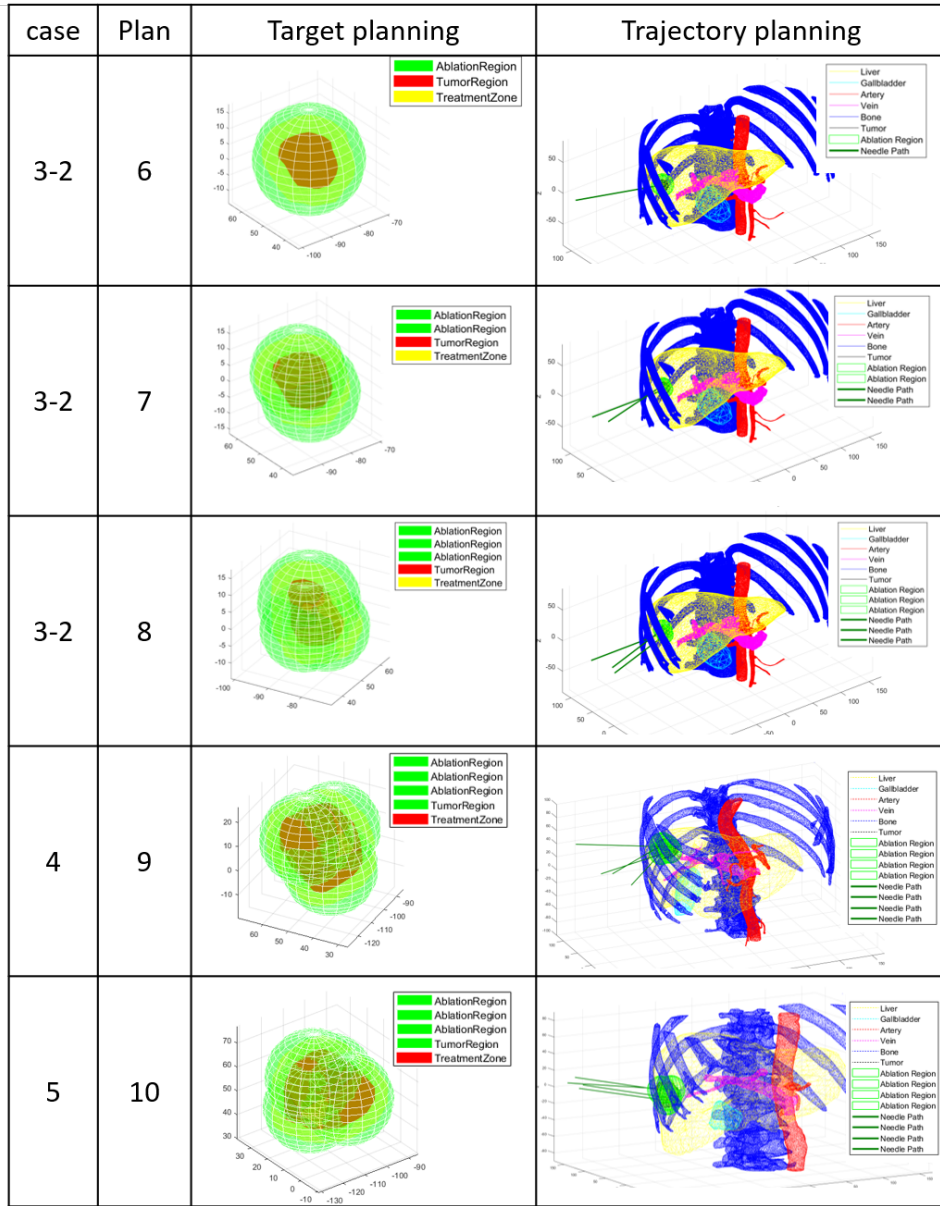


Figure 2.9: The needle target and trajectory planning result for the cases 3-1 to 5. The third column shows the tumor region (red), treatment zone of the tumor with a safety margin of $\theta_s = 5mm$ (yellow) and the ablation zone for each electrode tip (green sphere). The last column shows the corresponding trajectory planning for the insertion where different parts such as ribs/spine (blue), liver (yellow), artery (red), vein (magenta), gallbladder (cyan) and the tumor (black) are marked with different colors. The ablation zone for each electrode tip is marked with a green sphere and the insertion path trajectory is marked as a green line.

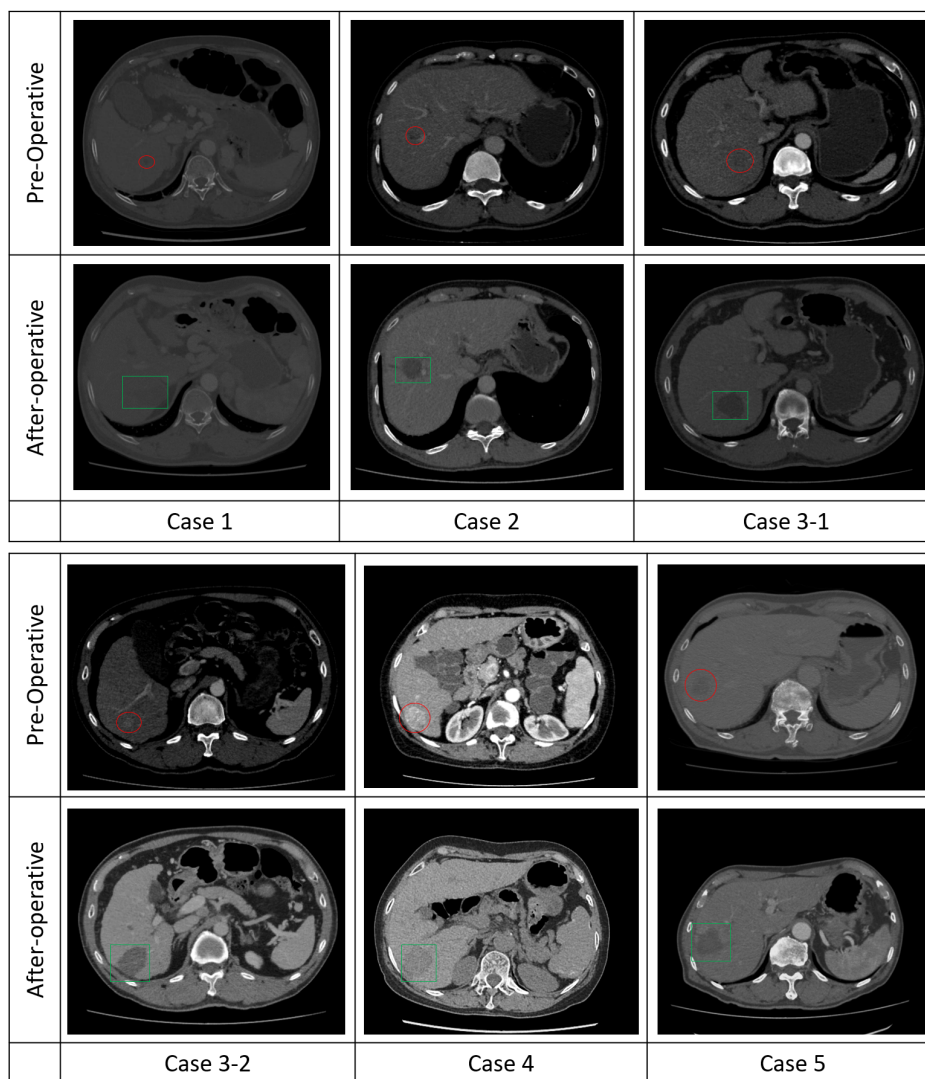


Figure 2.10: The CT images of the clinical outcome by surgeons. The upper row in both upper and bottom table shows the pre-operative CT images of the six tumors, where we applied our path planning. The lower row shows the CT images after the surgeons performed the ablation. The red circles highlight the tumor region, while the green squares highlight the ablation region after surgery.

Part III

Dynamic tumor puncture

AR-Guided Respiratory Liver Tumors Punctures

Augmented Reality Guided Respiratory Liver Tumors Punctures: A Preliminary Feasibility Study

Liver tumor puncture is the key step for both liver biopsy and the thermal ablation treatment. Even though the puncture procedure is performed in only a short time, the breathing motion of the patient will still cause a dynamic movement of the target. This movement improves the difficulty for surgeons to puncture the needle towards the pre-planned target. Besides, the puncture accuracy under traditional CT-guided modality is highly dependent on the surgeon's experience as its high requirement for the imagination of 3D anatomical structures and hand-eye coordination, i.e. performing puncture process while looking at the pre-planned puncture path displayed on a monitor. Thus, an intuitive and friendly navigation modality, which can display the dynamic position of the liver tumors under respiration, is necessary for improving the accuracy and efficiency of puncture.

This chapter aims to improve the puncture accuracy and efficiency problem via a method that solves the dynamic puncture target localizing problem. In order to solve the dynamic puncture problem, our method organized the reconstruction of respiratory motion based on the attribute of the patient's respiration. This work is done under the assumption that a respiratory cycle of the patient after anesthesia can be considered as a regular repeat period that contains always an exhalation-inhalation stage and an inhalation-exhalation stage. At the same time, this work also assumes that at a specific time, the internal tumor displacement and the external skin movement are at the same respiration state. In this way, this task can be organized as a question that computes the corresponding internal tumor position according to the observed movement of the external skin marker. Therefore, our method set up a correlation model between the internal tumor motion and external skin movement. By attaching optical markers to the patient's abdomen skin, the optical tracking system can observe the skin movement under breath during the puncture. As the markers' and tumor's displacement under respiratory motion can be reconstructed by CT scanned medical image, the tumor position at a specific time can be therefore computed from the real-time optical marker's position. In order to show the

navigation information in an intuitive way, our method calibrates the OST-HMD Epson MoveRio BT300 and the optical tracking system NDI in our pipeline. Therefore, the real-time position of the tumor can be shown in the holographic augmented reality way.

The validation experiment is done at Shenzhen People's Hospital. In the animal experiment, an artificial lesion is implemented into the liver of a healthy beagle dog. In the pre-operative stage, the displacement of the artificial tumor and the optical markers under the beagle dog's respiratory cycle are constructed. The puncture experiments are performed by experienced surgeons in both CT-guided and the holographic AR-guided way. The puncture result showed that the process with guidance using our augmented reality modality gives higher precision and less needle adjustment than the traditional puncture modality with CT-guided information. The method in this chapter is a preliminary feasibility study, which shows the potential possibility for applying the augmented reality surgical navigation method in the general surgery, in which the operation target has a movement under the patient's respiratory.

Content of this chapter is published as a peer reviewed technical brief paper in conference ACM SIGGRAPH Asia 2019:

Ruotong Li, Tianpei Yang, Weixin Si, Xiangyun Liao, Qiong Wang, Reinhard Klein, Pheng-Ann Heng: Augmented Reality Guided Respiratory Liver Tumors Punctures: A Preliminary Feasibility Study. ACM SIGGRAPH Asia Technical Briefs 2019: 114-117. <https://doi.org/10.1145/3355088.3365166>

All the medical experiment was approved by the local ethics committee. Shenzhen People's Hospital provides the medical data and the experiment animal used in this article. Jianxi Guo and Yanfang Zhang are responsible for the medical image labeling, medical knowledge consulting and animal experiment performing.

Contribution of the thesis author: Conceptualization, Methodology, literature review, algorithm implementation and validation, results interpretation and visualization, manuscript composition, validation experiment design.

Abstract

CT-guided radiofrequency ablation (RFA) has evolved rapidly over the past decade and become a widely accepted treatment option for patients with liver tumors. However, it is hard for doctors to locate tumors precisely while avoid damaging the surrounding risk structures with 2D CT images, which only provides limited static information, especially in case of respiratory motion. This paper presents a novel augmented reality guidance modality for improving the precision of liver tumors punctures by providing

visual cue of 3D personalized anatomy with respiratory motion. Optical see-through display devices Epson MoveRio BT300 and Microsoft HoloLens are used to mix pre-operative 3D personalized data and intra-operative physical scene. Here an augmented reality based surgical navigation pipeline is proposed to achieve the transformation from raw medical data to virtual guidance information and precisely superimpose this information onto real experimental animal. In addition, to alleviate the difficulty during needle placement induced by respiratory motion, we proposed a correlation model to real-time predict the tumor position via regression based respiration state estimation and the statistical tumor motion model. We experimentally validated the proposed system on in vivo beagle dogs with artificial lesion, which can effectively improve the puncture efficiency and precision. The proposed augmented reality modality is a general strategy to guide the doctors perform precise percutaneous puncture under respiration conditions and has the potential to be used for other surgical navigation tasks.

Keywords: Augmented Reality; Surgical Navigation; Virtual-real Alignment; Correlation Model, Statistical Motion Model

3.1 Introduction

Radiofrequency ablation (RFA) therapy for liver tumor is a widely used local mini-invasive percutaneous puncture treatment technology. Traditionally, surgeons in RFA surgery are guided by the ultrasound and computed tomography (CT) imaging to place the needle into the target tumor. However, the ultrasound is too fuzzy for the surgeons to distinguish the tumor with the surrounding tissues during percutaneous puncture, while CT images can provide more clear guidance images, but it cannot provide real-time intra-operative guidance [Lee et al., 2010, Kim et al., 2012]. Besides, the “Heads up” display of 2D intra-operative guided images further increases the operation difficulty and reduces the operation precision, since it lacks direct coordinating of surgeons’ hands with the vision [Crocetti et al., 2016, Cazzato et al., 2016].

Beyond the traditional 2D image-guided modality, augmented reality (AR) is a promising technology for surgical navigation and attracts widespread attentions from academy and industry communities since it can integrate virtual objects into the users perception of reality by graphics technologies. Philips developed an augmented-reality surgical navigation system to assist traditional image-guided minimally-invasive surgical guidance by combination of 3D X-ray imaging and optical imaging to provide surgeons with a unique augmented-reality view of the inside and outside of a patient during surgical procedures. However, it is still not convenient enough for doctors since hand-eye coordination is also a prerequisite conditions for doctors. Optical see-through head-mounted

display (OST-HMD) can well tackle this issue, it can provide the on-patient see-through guidance modality and enhance the surgeon’s perception of the depth and spatial relationships of surrounding structures through the augmented reality-based fusion of 3D virtual objects with real objects [Bernhardt et al., 2017b, Guha et al., 2017a]. Nowadays a lot of researchers have developed augmented reality navigation system for different medical application [Xie et al., 2017, Qian et al., 2018], but their guidance information is in static mode, which is not suitable for applications in dynamic conditions, especially for the free breathing.

This paper presents a comprehensive workflow for augmented reality based surgical navigation of needles in respiratory liver tumor targeting for RFA or other therapies where 2D images is not precisely enough to locate the lesion. In our prototype, we develop a collocation mechanism for all utilities to precisely align the coordinate system of optical measurement system, the augmented reality visualization system with the real objects, including puncture needle, tumor and liver on the animal. Besides, for respiratory motion, We propose a internal-external correlation model to associate the motion of surface makers on animal abdomen with that of internal tumors, here regression model is proposed to estimate the respiration state and then predict the respiratory tumor position according to the statistical tumor motion model. With our augmented reality guidance modality, surgeons can more intuitively locate the target tumors in a more efficient and accurate manner. The overview of our system is shown in Fig. 3.1.

3.2 Methodology

3.2.1 Raw medical data acquisition and processing

We employ a Beagle dog to perform the animal experiment. To accurately construct the spatial information between liver, tumor and ribs, we place 6 NDI surface marker as landmarks on the skin that near the ribs of it, shown in Figure 3.2. The ground truth of the respiratory motion is obtained via 4D-CT imaging, which records the deformation and displacement of the internal organ together with the surface marker under the free-breathing respiratory motion. At the same time, we continuous tracking the surface marker with the optical tracking system.

The Materialise Mimics software is used for manually segment the CT images of the abdomen into different tissues and accurately reconstruct the 3D geometric of the patient-specific model, including the liver, tumor and the surface marker on the dog’s skin. The 3D models denotes with $M = (V, E)$, where V is the set of vertices (in CT-image coordinate) on the model surface and E is the set of edges (forming the triangles).

Marker locations $S_M(t) = \{s_1(t), \dots, s_n(t) | s_i(t) \in \mathbb{R}^3, t \in \mathbb{R}_+\} (n = 6)$ and the tumor location $S_T(t) \in \mathbb{R}^3, t \in \mathbb{R}_+$ under the CT coordinate are cal-

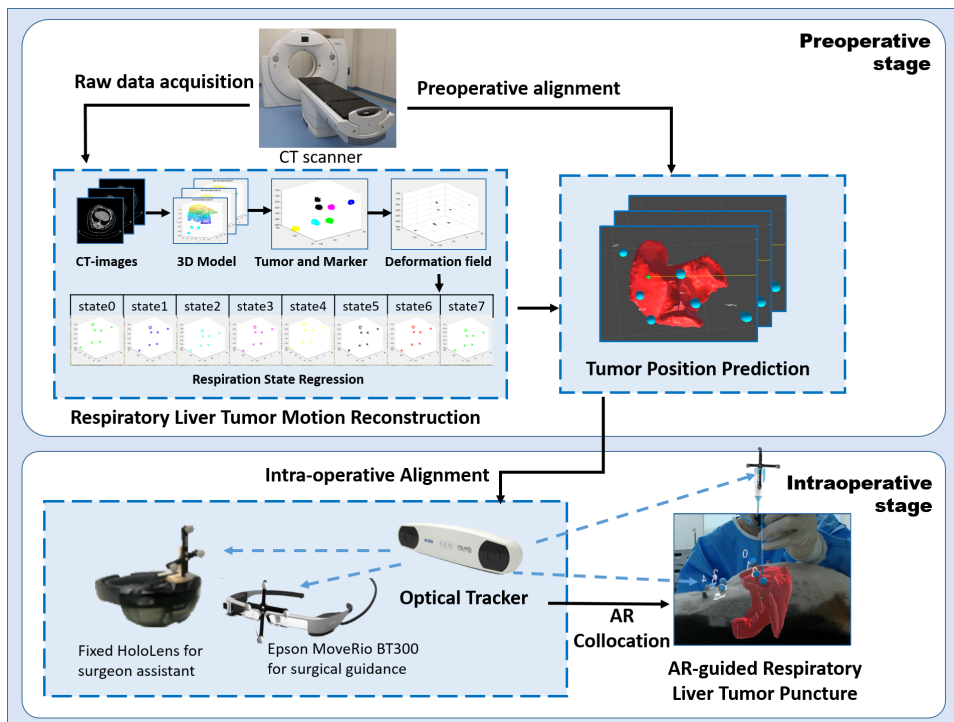


Figure 3.1: The pipeline of our augmented reality based surgical navigation system.

culate from the center of the patient specific 3D model. The surface marker position $O_M(t) = \{o_1(t), \dots, o_n(t) | o_i(t) \in \mathbb{R}^3, t \in \mathbb{R}_+\} (n = 6)$ under world coordinate is directly get from the optical tracker. With this procedural, we acquired the marker movement in both CT-device and world coordinate. The marker locations obtained by CT can map into the world coordinate by apply the transformation T_{CT}^{Tra} .

We analyze the continuously captured periodical marker movement with tracker tracked location data $O_M(t)$ to get the average marker movement period $\bar{O}_M(t)$. Then we sort the CT-extracted marker position $S_M(t)$ and its corresponding tumor position $S_T(t)$ by placing its mapping $S'_M(t)$ in the proper order which follows the movement in $\bar{O}_M(t)$. Then we perform the data augmentation via spline interpolation, which allows generating complete respiration sequences for surface marker and tumor.

3.2.2 Respiratory motion reconstruction

In order to provide precisely navigation information to the surgeon, we reconstruct the respiration surface marker motion and tumor motion via statistical motion model. In present stage, we only consider the correlation between liver tumor and surface markers during respiration.

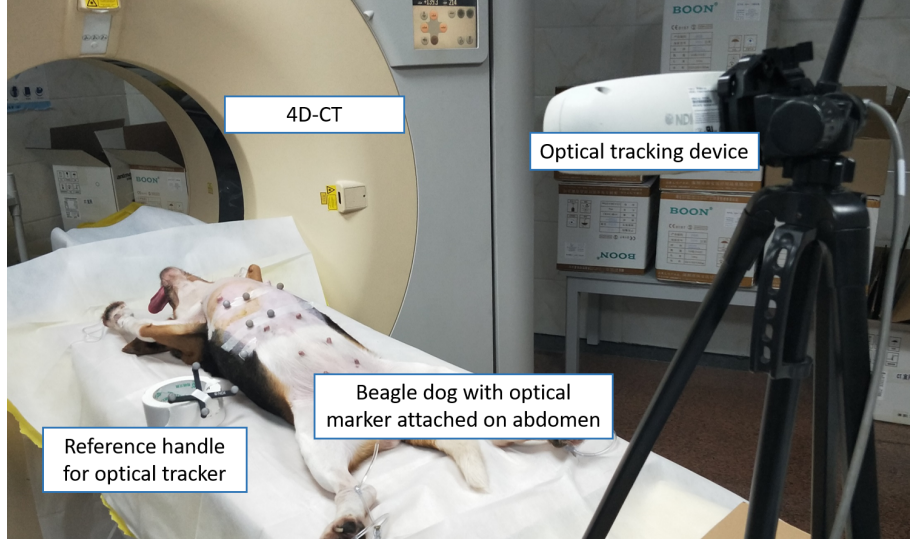


Figure 3.2: Raw medical data acquisition.

We assume that the respiration cycle is a regular repeat consists the state an exhalation-inhalation stage and the inhalation-exhalation stage. Calculate the mean state $\bar{s}_{M,T}(t_{ref})$ as reference state, we can calculate the deformation field of the tumor and markers position set. The deformation field therefore can represent as vectors between a reference state $\bar{s}_{M,T}(t_{ref})$ and the rest position in the displacement sequence.

$$\Delta s = s_{M,T}(t) - \bar{s}_{M,T}(t_{ref}) \quad (3.1)$$

We assume the position of the tumor and surface markers at specific respiration state follow the Gaussian distribution. Thus their displacement can be represented as a mixture of Gaussian distributions of different respiration states. Which can be represented as following:

$$p(\mathbf{x}) = \bar{s}_{M,T}(t_{ref}) + \sum_{n=1}^8 p(\Delta s_{M,T}(t_n)) p(\mathbf{x} | \Delta s_{M,T}(t_n)) \quad (3.2)$$

where $\Delta S_{M,T}$ is the set of marker and tumor displacement in the respiration states. In our work, we regress the respiration cycle to eight state $\{\Delta s_{M,T}(t_1), \dots, \Delta s_{M,T}(t_8)\}$ (shown in Figure 3.1).

3.2.3 Tumor Position Prediction

Based on the previous statistically motion modeling, we can represent the periodic motion of liver tumor and surface markers as a linear combination of the eight respiration states.

$$\Delta s_{M,T}(t) = s_{M,T}(t_0) + \mathbf{c} \cdot \Delta S_{M,T}(t_n) \quad (3.3)$$

where the $s_{M,T}(t_0)$ is a reference state of the intra-operative respiration. $c_i \in \mathbf{c} = (c_1, \dots, c_n), n = 8$ is a component in the vector of coefficients represents the current breathing state.

We assume that the internal-external respiration motion has a correlation that at a specific time, the tumor and the surface marker displacement are at the same respiration state.

For a intra-operative tracking state of surface marker $O_M(t)$, the breathing state \mathbf{c} can compute easily by least square regression:

$$O'_M(t) = S_M(t_0) + \mathbf{c} \cdot \Delta S_M(t_n) \quad (3.4)$$

$$O'_M(t) = T_{Tra}^{CT} \cdot T_{CTInt}^{CTpre} \cdot O_M(t) \quad (3.5)$$

where T_{Tra}^{CT} is the transformation from tracker to the CT device coordinate, which we used for motion modeling. T_{CTInt}^{CTpre} is the transformation from patient intra-operative pose to the pre-operative pose in the medical data acquisition phase. Thus the tumor position at the corresponding time is predict as:

$$s_T = s_T(t_0) + \mathbf{c} \cdot \Delta s_T(t_n) \quad (3.6)$$

Where the $s_T(t_0)$ is the tumor position at the intra-operative reference state, and c_i is the component of the linear coefficient.

In the end, the predicted tumor position needs to map the world coordinate in order to provide the proper information for the navigation system via transformation $s'_T(t) = T_{CT}^{Tra} \cdot s_T(t)$

3.2.4 Dynamic virtual-real alignment

Here Epson MoveRio BT300 is employed to display the virtual guidance information superposed on real objects, while HoloLens is equipped with the surgeon assistant to wear in a fixed position, monitoring the overall puncture process to provide surgeon with supplementary information in other perspective and recording the video.

System Calibration Figure 3.3 illustrates the collocation process of our AR prototype. Here we define the coordinate of optical tracker as the world coordinate, while attach optical markers on every utility in surgical scenario and holographic display devices. For each utility, we adopt two steps to achieve the precise system calibration, which are global and local transformation.

We first perform global transformation from utility coordinate to the world coordinate by $T_{Uti}^{Tra} = \{T_{Nee}^{Tra}, T_{Ani}^{Tra}, T_{Dis1}^{Tra}, T_{Dis2}^{Tra}\}$, denoting transformation from marker coordinate fixed on utilities to the world coordinate.

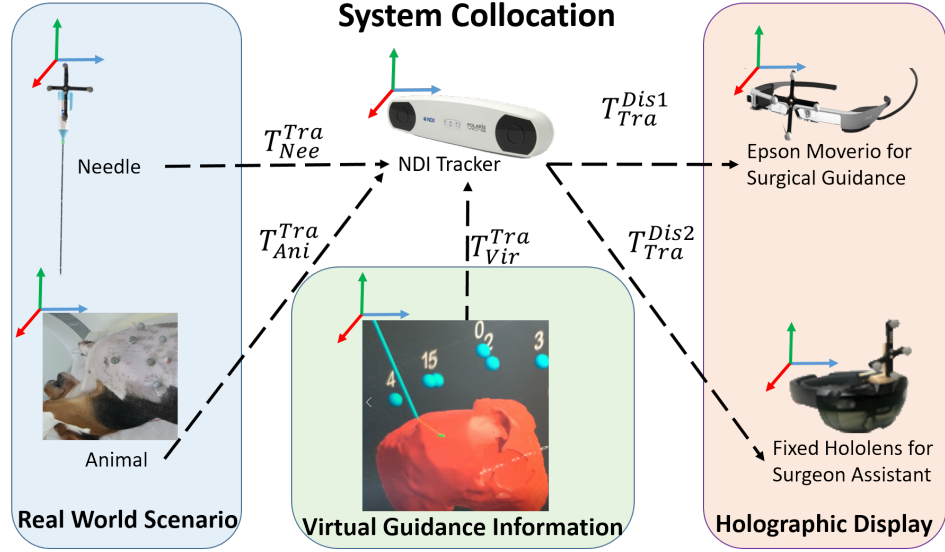


Figure 3.3: Coordinate transformation

Then we apply a local transformation from the utility coordinate to the optical marker via:

$$T_{Uti}^{Tra} = T_{dev}^{Opt} \cdot T_{dev} \quad (3.7)$$

Finally, we calculate the transformation $T_{Tra}^{Dis} \in \{T_{Tra}^{Dis1}, T_{Tra}^{Dis2}\}$ from global coordinate to the device display coordinate, which is the inverse of T_{Dis}^{Tra} .

Dynamic alignment Considering that doctors equipped with OST-HMD need to observe the respiratory liver tumor from different views, while manipulate the needle targeting the tumor, we present an accurate dynamic alignment method to perfectly superimpose 3D images of the needle, liver, tumor, surface markers onto the surgical region in situ. The specific implementation can be divided into pre-operative process and intra-operative process.

Pre-operative process:

- Scan a frame of CT image of animal and get the positions of body surface trackers in the CT coordination system $S_M(t)$.
- Record the location of six body surface trackers in the optical tracker coordination system $O_M(t)$ at the same time.
- Calculate T_{Vir}^{Tra} according to the Eq. 3.8 and send it to correlation model.

$$T_{Vir}^{Tra} = O_M(t) \cdot S_M(t)^{-1} \quad (3.8)$$

Intra-operative process:

- NDI tracker captures transformation of optical markers on needle and surface markers in real time T_{Nee} , T_{Ani} .
- Take a frame of CT scan, calculating T_{CTInt}^{CTpre} with Eq. 3.5 for the patient pre- and intra-operative alignment.
- Display the virtual guidance information on MoveRio and HoloLens according to:

$$Dispalys = T_{Tra}^{Dis} \cdot T_{Vir} \quad (3.9)$$

where $T_{Vir} \in \{T_{Nee}, T_{Ani}, O_{M,T}(t)\}$.

3.3 Experiment

To validate the effectiveness of our navigation system, an experienced surgeon was invited to adopt both traditional CT-guided and augmented reality guided modalities to insert the ablation needle into the dog respiratory liver tumor. According to suggestions from the surgeon, we define only a puncture no further than $3.50mm$ from the tumor center as an “accurate” puncture, needle adjustment is allowed for achieving the accurate puncture.

3.3.1 Material

Experiment animal: beagle dog, female, 36months, 12kg. Percutaneous liver puncture of experimental animal was performed after general anesthesia.

Animal tumor model was build by implanting the iodine oil in animal liver. We first scan the dog abdomen to determine the appropriate position of tumor implantation, and then use the sticky tape to attach the locator on the animal abdomen skin around liver. Besides, we can choose the optimal needle insertion path (7th subcostal), insertion angle (perpendicular to the skin) and distance (8cm) from the puncture point on the skin. Last, the surgeon injected the prepared iodine oil (2ml) into the liver.

3.3.2 Result

In the augmented reality navigation modality, we use the NDI Polaris to track all the utilities in surgical scenario, so that the operation region is limited in the tracking region of NDI Polaris. Besides, the surgeon wears the Epson MoveRio to locate the moving tumor while the assistant wears the HoloLens to monitor the overall process and record the video. The operations can be seen in the Fig. 3.4.

The percutaneous puncture results of traditional CT guided modality and our augmented reality modality can be seen in Fig. 3.5 and Table 3.1, which illustrates that compared with traditional navigation modality, our method allows surgeon intuitively targeting the lesion from different insert

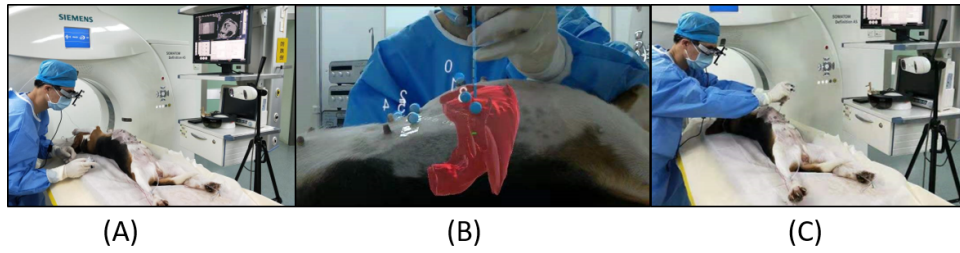


Figure 3.4: The surgeon performed AR-guided needle insertion.

angles with high accuracy, while it can also reduce the number of needle adjustments.

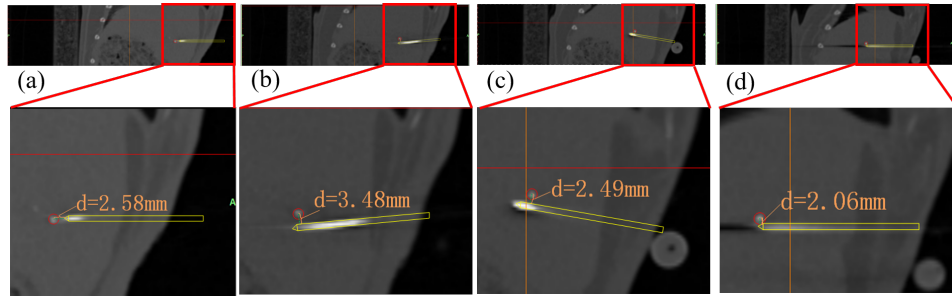


Figure 3.5: The sagittal plane of the needle insertion result in CT. (a) traditional CT-guided puncture, (b), (c) and (d) AR-guided puncture from three different insertion angles.

3.3.3 Discussion

In our current prototype, the ablation needle is modeled as rigid body. However, the deformation of ablation needle cannot be ignored, we now require the surgeons hold the needle in a proper way to keep the puncture direction along the needle direction in order to reduce the errors induced by needle deformation.

3.4 Conclusion

This paper presented a preliminary feasible study of using the augmented reality guidance modality to achieve the respiratory liver tumor puncture. The performance of this novel navigation modality is validated on a beagle dog with artificial lesion. Experimental results demonstrate that surgeons with AR-guided information can target the lesion more easily, more efficiently and more accurately than using the traditional 2D CT images guided modality.

Table 3.1: Accuracy comparison of AR-guided and traditional CT-guided modalities.

Nr.	1st	Adjust 1	Adjust 2	Adjust 3
Tr	9.02mm	7.02mm	3.81mm	2.58mm
AR 1	4.89mm	3.48mm	-	-
AR 2	9.79mm	6.08mm	2.49mm	-
AR 3	8.04mm	2.06mm	-	-

Considering that our current correlation model can only predict the tumor moves along with the surface markers, which can't provide the information of other key structures in target region, such as vessels. Thus, our immediate plan is to achieve the non-rigid registration of such key structures in order to provide more comprehensive navigation information for the surgeons. Besides, we will be also interested in investigating the modeling method of flexible needle during puncture. Furthermore, we will extend this promising guidance modality to other challenging surgical scenarios, such as deep brain stimulation, where electrode needs to be placed in a high-precision target region.

Errata

The sentence in 3.2.1 on page 55 should be:

The surface markers' position $O_M(t) = \{o_1(t), \dots, o_n(t) | o_i(t) \in \mathbb{R}^3, t \in \mathbb{R}_+\}$ ($n = 6$) under world coordinate are directly get from the optical tracker. With this ~~proeedural~~ procedure, we acquired the marker movement in both CT-device and world coordinate.

The Equation 3.1 on page 56 should be:

$$\Delta s_{M,T}(t) = s_{M,T}(t) - \bar{s}_{M,T}(t_{ref})$$

The explanation of Equations in 3.2.3 on page 56 are update as:

- $c_i \in \mathbf{c} = (c_1, \dots, c_n), n = 8$ is a component in the vector of coefficients ~~presents~~ presenting the current breathing state.
- For a intra-operative tracking state of ~~surface marker~~ the surface markers $O_M(t)$, the breathing state \mathbf{c} can ~~compute~~ be computed easily by least square regression:

$$O'_M(t) = S_M(t_0) + \mathbf{c}(t) \cdot \Delta S_M(t_n)$$

- Thus the tumor position at the corresponding time is ~~prediet~~ predicted as:

$$s_T(t) = s_T(t_0) + \mathbf{c}(t) \cdot \Delta s_T(t_n)$$

The Equation 3.9 on page 59 and its corresponding explanation updated as:

$$Dispaly = T_{Tra}^{Dis} \cdot T_{Vir}$$

where $T_{Vir} \in \{T_{Nee}, T_{Ani}, O_{M,T}(t)\}$. The T_{Tra}^{Dis} presents the transformation that virtual information convert from the tracker coordinate to the display coordinate of the corresponding display devices.

MR Based Respiratory Liver Tumor Puncture Navigation

Mixed Reality Based Respiratory Liver Tumor Puncture Navigation

Puncture of the liver tumor under the patient's respiration is the key challenge for both liver biopsy and the thermal ablation treatment. This is because not only the target tumor but also the structure around the tumor is moving along with the breath. Therefore, not only puncturing the dynamic target is difficult, but also avoiding the moving risk area around the target while performing the puncture is difficult.

In this chapter, our work aims to propose an intuitive guidance modality that helps doctors puncture the dynamic liver tumor without touching the risk structure. Our method constructed the statistic motion model of the 3D liver structure that was reconstructed from the expert segmented pre-operative CT images. With this statistical motion model, the liver deformation and tumor displacement at eight respiration states are pre-computed. Our method assumes that the target tumor movement, the liver displacement, and the surface marker motion are always in the same respiratory state. In this work, the respiration of a patient after anesthesia is considered a regular repeat period. Therefore, at a specific time, the deformation and displacement of the liver and tumor are always knowable after determining the respiratory state. Our algorithm computes the respiratory state during the liver tumor puncture from the optical skin markers' movement obtained by the NDI optical tracking system. With the computed respiration state, this method can therefore estimate the corresponding tumor position and deformation of the liver according to the pre-computed statistical motion model. In order to show the navigation information intuitively, An OST-HMD, i.e. Microsoft HoloLens, and the optical tracking system NDI are involved in our prototype. After calibration, the devices and the surgical instruments attached with optical tracking markers are all converted into the same coordinate. HoloLens therefore can show the real-time interaction of the puncture needle and the liver motion compensation at the correct position on the patient with respect to the coordinate in the real scene. In this way, surgeons can see the target movement information superimposed on the patient and perform the puncture intuitively.

The validation experiment is done at Shenzhen Second People's Hospital. In the animal experiment, 10 optical markers are attached to the skin near the ribs of a vivo pig, who had equipped with an artificial tumor in the liver. The displacement of the liver, tumor and optical markers is constructed from the pre-operative CT scanned images. The calibration accuracy of the augmented reality visualization has been validated on a 3D printed skull. With the display for the liver compensation information on HoloLens, doctors can observe the target tumor and liver movement directly and intuitively. The result shows that doctors performing the tumor puncture with a mixed reality guided modality gives higher precision than it with traditional free-hand puncture guided by CT images. In general, the method present in this chapter shows the efficiency and accuracy of a mixed reality-based tumor puncture navigation modality, which involves the motion compensation of the liver region. Experimental result shows the potential for applying this mixed reality surgical navigation method to guided needle insertion for liver RFA/MWA surgery, which can assist surgeons to perform the operation simpler, more efficient and more precise.

Content of this chapter is published as a peer reviewed paper in the journal Computational Visual Media:

Ruotong Li, Weixin Si, Xiangyun Liao, Qiong Wang, Reinhard Klein, Pheng-Ann Heng: Mixed reality based respiratory liver tumor puncture navigation. Computational Visual Media 5(4): 363-374 (2019). <https://doi.org/10.1007/s41095-019-0156-x>

All the medical experiment was approved by the local ethics committee. Shenzhen Second People's Hospital provides the medical data and the experiment animal used in this article. Xuesong Deng is responsible for the medical image labeling, medical knowledge consulting and animal experiment performing.

Contribution of the thesis author: Conceptualization, Methodology, literature review, algorithm implementation and validation, results interpretation and visualization, manuscript composition, validation experiment design.

Abstract

This paper presents a novel mixed reality based navigation system for accurate respiratory liver tumor punctures in radiofrequency ablation (RFA). Our system contains an optical see through head mounted display device (OST-HMD), Microsoft HoloLens for perfectly overlaying the virtual information on the patient and a optical tracking system NDI Polaris for calibrating the surgical utilities in the surgical scene. Compared with traditional navigation method with CT, our system aligns the virtual guidance information and real patient and real-time update the view of virtual guidance

via a position tracking system. In addition, to alleviate the difficulty during needle placement induced by respiratory motion, we reconstruct the patient-specific respiratory liver motion through statistical motion model to assist doctors precisely puncture liver tumors. The proposed system has been experimentally validated on vivo pigs with an accurate real-time registration approximately 5-mm mean FRE and TRE, which has the potential to be applied in clinical RFA guidance.

Keyword: Mixed Reality; Human Computer Interaction; Statistical Motion Model

4.1 Introduction

Radiofrequency ablation (RFA) therapy is a widely used mini-invasive treatment technology for liver tumor. Doctors insert a radiofrequency electrode into the target tissues of patient, and the increasing temperature (greater than 60 °C) will produce degeneration and coagulation necrosis on the local tissues [Wang et al., 2012]. RFA has become a widely and clinically accepted treatment option for destruction of focal liver tumors with several advantages, such as low trauma, safety, effectiveness, and quick postoperative recovery [Flaherty and Bilchik, 2017, Cai et al., 2016].

Traditional RFA surgery are navigated by the computed tomography (CT), ultrasound or magnetic resonance (MR) image for surgeons to insert the needle into the target tumor. Then the tumor can be completely coagulated with a safety margin and non-injury of critical structures during energy delivery. Thus, the navigation imaging information plays a key role in the safe and precise RFA planning and treatment for the target tumor [Clasen and Pereira, 2008]. In general, much surgical experience and skill are required to perform safe and accurate needle insertion with 2D navigation images, because current 2D image-based navigation modality can only provide limited information without 3D structural and spatial information of the tumor and surrounding tissues. Besides, the display of 2D guided images showed on the screen further increases the operation difficulty. As it lacks direct coordinating of hands and vision, the precision is quite depending on surgeons' experience [Crocetti et al., 2016, Cazzato et al., 2016].

Mixed reality (MR) can provide the on-patient see-through navigation modality and enhance the surgeon's perception of the depth and spatial relationships of surrounding structures through the Mixed reality-based fusion of 3D virtual objects with real objects [Bernhardt et al., 2017b]. In this regards, surgeons can directly observe the target region with the on-patient see-through 3D virtual tumor registered and overlaid on the real patient, thus enabling the surgeons still remain cognizant of and engage in the true surgical environment and greatly benefit the surgeons' operation efficiency and precision. As an optical see-through head-mounted displays

(OST-HMD), Microsoft HoloLens has been significantly used in recent years in various fields, including the medical education and surgical navigation. The HoloLens can project the 3D personalized virtual data in specified position of patients, which can well support the on-patient see-through modality for medical guidance. Compared with the traditional 2D image-based navigation modality, the surgeons are able to comprehensively and intuitively recognize the characteristics of liver and tumor, which can benefit the surgeons in needle path planning for liver punctures more efficiently and accurately.

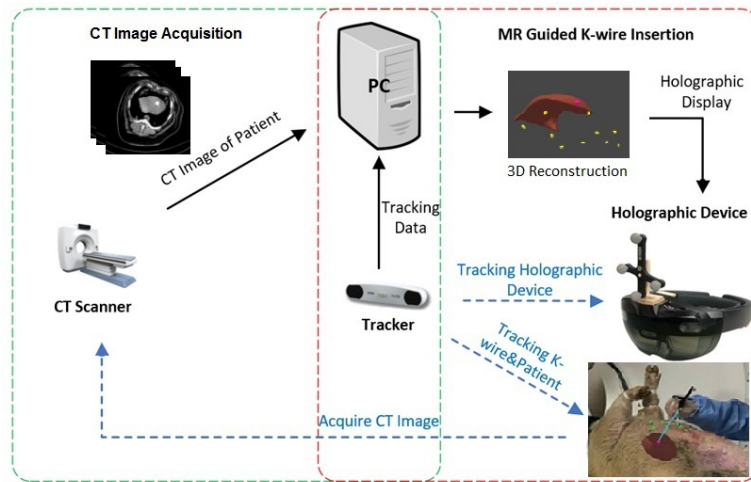


Figure 4.1: Mixed reality based needle insertion navigation.

Another challenge for safe and precise RFA liver therapy is the respiratory liver motion, which is an inevitable issue in clinical practice and has a great impact during the RFA procedure for liver tumors punctures. Doctor may encounter difficulties in locating the target tumor area induced by respiratory liver motion, as the pre-operative imaging is severely different from that during the RFA therapy due to the organ movement induced by the respiratory. In clinical practice, it is also worth noticing that there exists techniques to physically or physiologically ease the respiratory liver motion issue in a straightforward way, such as respiratory gating [Nicolau et al., 2007], anesthesia with jet ventilation [Biro et al., 2009] and active breathing control (breathing holding) [Wunderink et al., 2008]. However, these methods induce either extra cost or psychological burden to the patient, and are not a universal way to be practical enough for every patient. For example, it is hard and unrealistic for the patients to hold their breath too long in the breathing holding method [Wunderink et al., 2008]. Therefore, it is in an urgent need to develop a new method to tackle this issue, allowing patients to breathe freely during the whole RFA procedure for liver tumor. In this regards, analyzing the patient-specific respiratory organ motion based

on 4D liver CT images and compensating the respiratory motion with the mathematical model would be a promising way to achieve both time- and cost-effective and absolutely accurate delivery for each patient.

To enable the patient breath freely during the RFA procedure and achieve safe and accurate RFA operation, we developed a Mixed reality based navigation platform via Microsoft HoloLens for RFA liver therapy with respiratory motion compensation, which provides a real-time on-patient see-through display, navigating exactly where the surgeon should insert the needle during the whole RFA procedure. By reconstructing the patient-specific organ motion using 4D CT images, we adopt a precise statistical motion model to describe the respiratory motion and its variability in 4D for compensating the respiratory motion of liver tumors. In our platform, we propose a new calibration procedure to properly align the coordinate system of rendering with that of the tracker, and then automatically register rendered 3D graphics of liver and tumor with tracked landmarks, liver and tumor in the vivo pig, assisting surgeons in accurately approaching the target tumors, making the operation simpler, more efficient and accurate. The overview of our system is as shown in Fig. 4.1.

4.2 Related work

Many researchers have explored image-base navigated ablation of tumors and evaluated the accuracy of 2D image navigation modalities which have evolved considerably over the past 20 years and are increasingly used to effectively treat small primary cancers of liver and kidney, and it is recommended by most guidelines as the best therapeutic choice for patients with early stage hepatocellular carcinoma [Breen and Lencioni, 2015]. To achieve accurate pre-procedural planning, intra-procedural targeting, and post-procedural assessment of the therapeutic success, the availability of precise and reliable imaging techniques would be the essential premise [Tiong and Maddern, 2011, Ahmed et al., 2011]. Among all 2D image navigation modalities, ultrasound (US) is the most widely used imaging technique for navigating percutaneous ablations for its real-time visualization of needle insertion and monitoring of the procedure [Livraghi et al., 2011]. However, the ultrasound images are not clear enough for distinguish the target area. Other 2D image navigation modalities, including the computed tomography (CT), magnetic resonance imaging (MRI), or positron emission tomography (PET), can provide more clear navigation images [Kim et al., 2012], but cannot provide real-time navigation information for intra-operative process in the RFA therapy. Besides, Amalou et al. adopted another modality of electromagnetic tracking by referencing to pre-operative CT imaging, which utilizes miniature sensors integrated with RFA equipment to navigate tools in real-time. They have

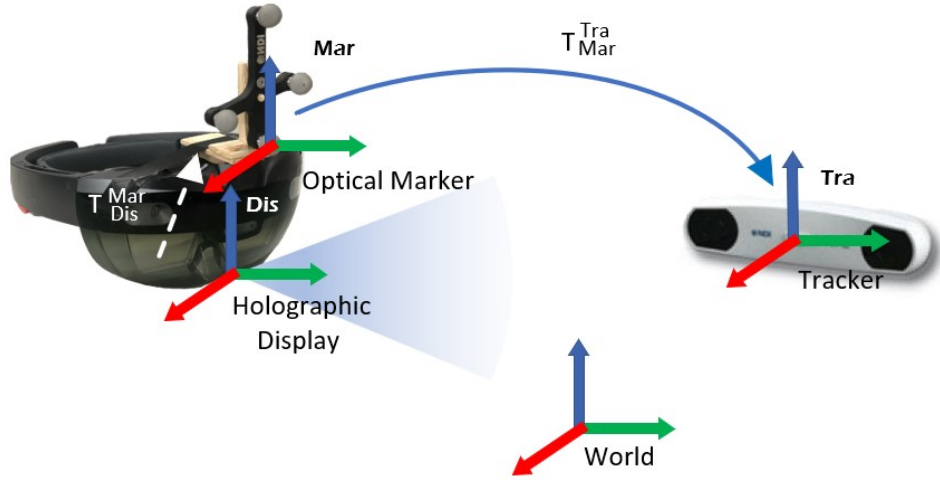


Figure 4.2: Coordinate calibration between Microsoft HoloLens and NDI tracking system.

achieved successfully during a lung tumor ablation with the accuracy of 3.9 *mm* [Amalou and Wood, 2012].

To overcome the disadvantages of 2D image based navigation, mixed reality approaches have been proposed to navigate the physician during the intervention in recent years. To display virtual models of anatomical targets as an overlay on the patient's skin, Sauer et al. [Sauer et al., 2003] use a head-mounted display (HMD) for the physician to wear, providing the mixed reality-based navigation for the surgery. In other cases, Khan et al. [Khan et al., 2006] projected the 3D virtual objects with a semi-transparent mirror, thus the surgeons can manipulate the needle behind the mirror which shows the overlay 3D virtual objects floating inside or on top of the patient's body, providing a relative spatial information and mixed reality navigation for the surgeons. Ren et al. [Ren et al., 2014a] realized the semi-transparent overlays for overlapping ablation zones and surrounding essential structures, and they projected the current needle trajectory and the planned trajectory onto the different anatomical views, thus navigating the surgeons' operation in an mixed reality environment. Chan and Heng [Chan and Heng, 2014] introduced a new visualization method, which adopts a volumetric beam to provide depth information of the target region for the surgeons, and they also offered information about the orientation and tilting by combining a set of halos.

To ease the negative impact on accuracy of liver punctures induced by respiratory motion, many approaches has been proposed to tackle this issue in radiation therapy [Schweikard et al., 2004, Ren et al., 2007]. Thought numerous approaches for motion-adapted 4D treatment planning and 4D radiation have been reported, the clinical implementation of 4D guidance of

tumor motion is currently still in its infancy. However, most existing methods lack qualitative and quantitative analysis of respiratory motion-related effects. By introducing the 4D CT images of respiratory liver and tumor, the variations in depth and frequency of breathing effect can be numerically reconstructed with the statistical model. Besides, simulation-based flexible and realistic models of the human respiratory motion have the potential to deliver valuable insights into respiration-related effects in radiation therapy. This model can offer the possibility to investigate motion-related effects for variable anatomies, for different motion patterns and for changes in depth and frequency of breathing, and finally can contribute to the efficient, safe and accurate RFA therapy.

4.3 Methodology

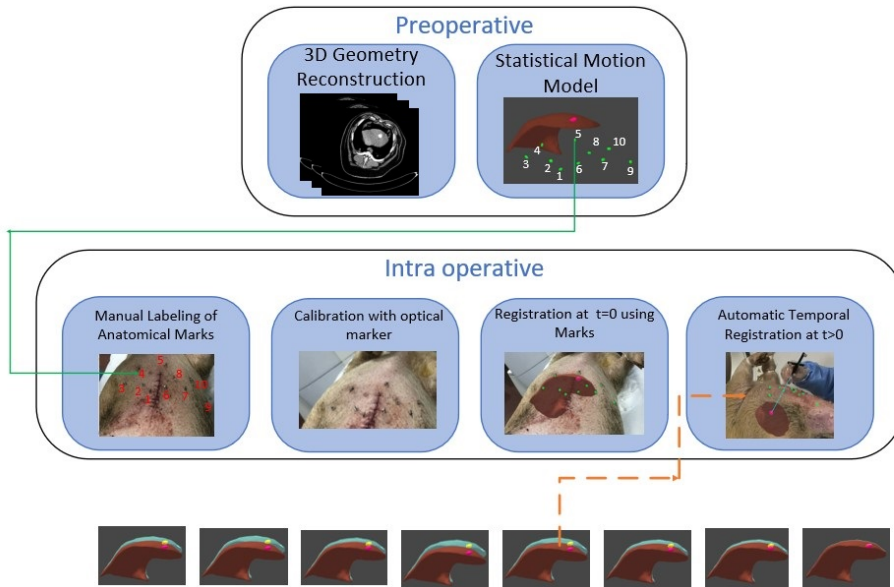


Figure 4.3: Statistical model based respiratory motion compensation.

4.3.1 Method overview

To achieve high precision RFA, we propose mixed reality based navigation for respiratory liver tumor puncture to provide surgeons with virtual guidance of personalized 3D anatomical model. High matching degree between the real patient and virtual geometry model is prerequisite to achieve our goal. The match requirements are in two aspects. First, the virtual anatomical model must be with the same shape and deform under in the same way as that of the real patient. Secondly, the virtual geometry should be displayed

aligning with the real patient in operation. To fulfill the requirements, we design the system with the workflow as illustrated in Fig. 4.3. In a preparation step the 3D virtual liver structures are reconstructed from CT images and a statistical motion model is estimated for respiratory motion compensation with assistance of landmarks. Then, during the surgery, the liver structure is updated and registered to the real patient timely with motion estimated from positions of landmarks.

4.3.2 Medical Data Acquisition and Preprocessing

We employ a vivo pig to perform the needle insertion operation. The accuracy of needle insertion is greatly impacted by the anatomic structures of the abdomen, which is the working area of the liver RFA procedure. Here, we adopt the Materialise Mimics software to manually segment the CT images of the abdomen, extracting different types of tissues and accurately reconstructing the 3D geometric model of the patient-specific liver and tumor. In addition, 10 metal landmarks are placed on the skin near the ribs before CT scanning for further anatomical motion modeling.

4.3.3 Virtual-real spatial information visualization registration

During needle-based interventions, the surgeons cannot observe the internal structure of liver anatomy directly. Thus, landmark structures have to be remembered from the pre-interventional planning image to guess the correct insertion direction via the limited information. This procedure highly depends on personal experience and may lead to a significant miscalculation in needle placement and thus failed tumor ablation. To solve this problem, we propose a manual registration method for accurately overlaying the 3D virtual structures of the liver on patient, as shown in Fig. 4.1. The NDI tracking system is adopted to acquire the transform of virtual liver structure in the rendering space. Each objects' transformation matrix in the rendering can be decomposed into two components, namely the transformation matrix from object's local coordinate system to local NDI coordinate system and transformation matrix from local NDI coordinate system to the view coordinate of the display device. Finally, by registering virtual objects to real objects, we can render the virtual structure using the HoloLens to provide needle insertion guidance for surgeons.

To acquire the transformation matrix from NDI system to HoloLens system, we fix a k-wire of NDI system on the HoloLens and statically bind the HoloLens system with a fixed virtual coordinate system of the k-wire. We can easily get the transformation matrix from k-wire markers to the HoloLens, denoted as T_{Dis}^{Mar} . Meanwhile, we can acquire the transformation matrix of the k-wire to the space of NDI Tacker, denoted as T_{Mar}^{Tra} . These

two matrices together form the transformation matrix from NDI coordinate system to the view coordinate in rendering space.

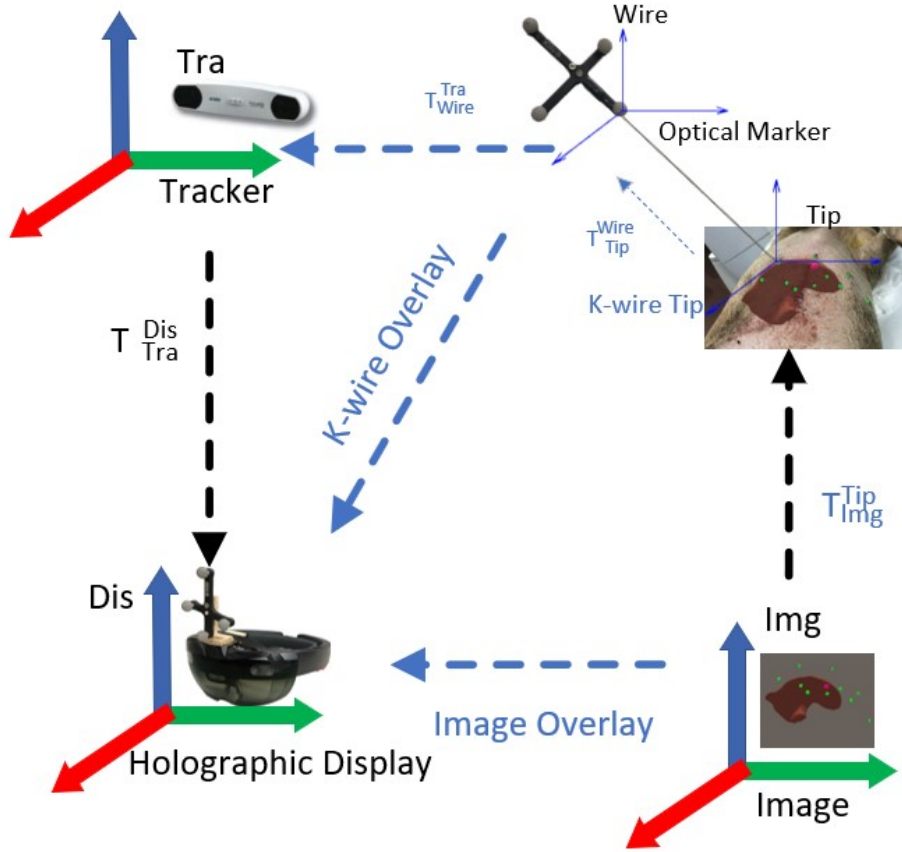


Figure 4.4: Registration of 3D virtual structure and real object.

After calibrating the coordinates between the Microsoft HoloLens and NDI tracking system, we can easily acquire the position of the landmarks via the tip of the k-wire. To accurately overlay the 3D virtual liver structure on the real object, we need to ensure the precise transformation between HoloLens, markers and NDI tracking system.

As shown in Fig 4.4, the position of the markers (optical tracking spheres) can be acquired with the NDI tracking system, denoted as T_{Mar}^{Tra} . As the position of k-wire's tip is known to the k-wire, by moving the tip of k-wire to the landmarks of the patients, we can acquire the landmarks' position via the optical markers of k-wire, denoted as T_{Tip}^{Mar} . The transformation matrix between the Microsoft HoloLens and optical trackers is,

$$T_{Tip}^{Dis} = T_{Dis}^{Tra} \cdot T_{Tra}^{Mar} \cdot T_{Mar}^{Tip} \quad (4.1)$$

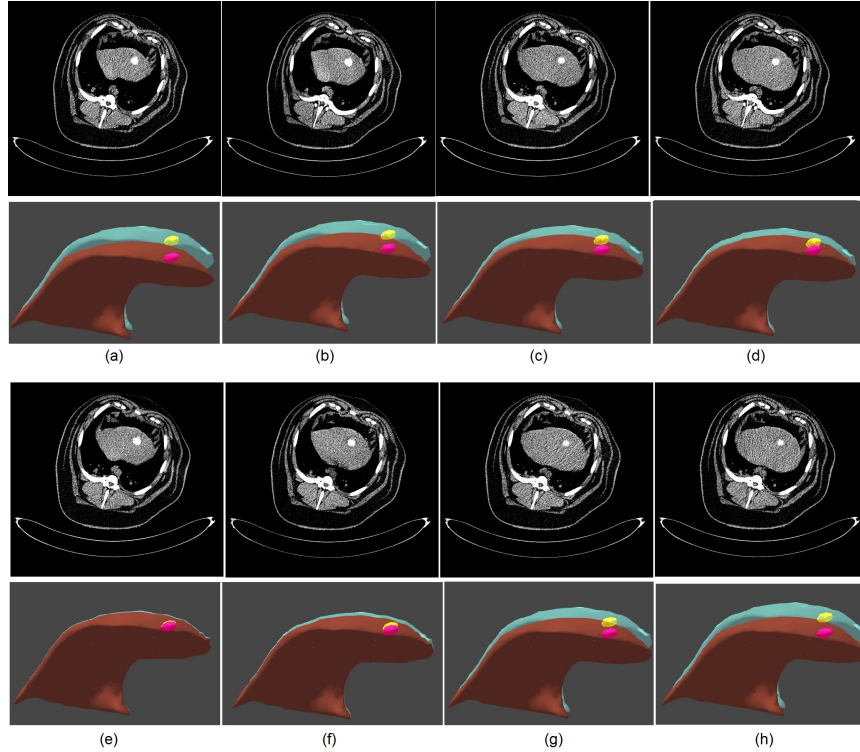


Figure 4.5: Patient-specific respiratory motion reconstruction. The red region shows the shape of the liver at the fully inhalation stage, while the light blue part region shows the shape of the liver at different respiration stage.

The 3D virtual liver structures reconstructed by the CT images can overlay on the real object via the following transformation matrix

$$T_{Tip}^{Img} = T_{Dis}^{Tip} \cdot T_{Tip}^{Img} \quad (4.2)$$

4.3.4 Statistical model based respiratory motion compensation

To overcome the respiratory liver motion during the needle insertion, we reconstruct the patient-specific organ motion via statistical motion model to describe the breathing motion and its variability in 4D images, for compensating the respiratory motion of liver tumors.

4D-CT based Statistical Modeling

The first step to perform statistical model based respiratory motion compensation is to acquire the ground truth of the respiratory motion via 4D-CT imaging, which records the deformation or displacement of the internal organ

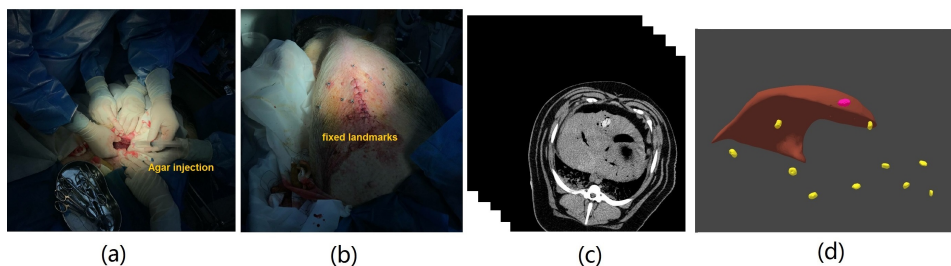


Figure 4.6: Animal experiment setting and 3D reconstruction results. (a). Tumor implantation using agar. (b). Metal landmarks placement. (c) CT imaging. (d). 3D reconstruction of liver, tumor and 10 metal landmarks.

under the free-breathing respiratory motion. Fig. 4.5 illustrates some typical slices of the 4D-CT images during respiratory motion and the reconstructed patient-specific 3D anatomy of liver and tumor at the corresponding time.

In essence, we need to build the statistical model by analyze the dynamic shape deformations of the target liver shape during the short term of the respiratory motion. In this work, we adopt the 4D-CT based statistical motion in [Jud et al., 2017] to estimate the respiratory motion of liver. The model assumes that the shape of 3D reconstructed liver anatomy in exhalation state obeys Gaussian distribution $p(\mathbf{r}^s | \mathbf{r}_\mu, \Sigma_{\mathbf{r}}) \sim N(\mathbf{r}_\mu, \Sigma_{\mathbf{r}})$ and deforms with respect to previously observed shape \mathbf{r}^s .

Except the shape changes modeling in the same time of exhalation state, we also need to consider the shape changes over time. In the 4D-CT images acquisition, we reconstruct the 3D liver anatomy for several times, and assume the shape changes to be a mixture of Gaussian distributions.

$$p(\mathbf{x}) = \sum_s p(s) p(\mathbf{x} | s) = \sum_s \pi^s p(\mathbf{x} | s) \quad (4.3)$$

where $\sum_s \pi^s = 1, \pi^s \in (0, 1), \forall 1, \dots, S$. For each observed shapes with a amount of time τ , suppose each component follows the Gaussian mixture distribution $p(\mathbf{x}^s) \sim N(\mathbf{x}_\mu^s, \Sigma_{\mathbf{x}^s})$.

$$\mathbf{x}_\mu^s = \frac{1}{\tau_s} \sum_t^{\tau_s} \mathbf{x}_t^s \quad (4.4)$$

$$\Sigma_{\mathbf{x}^s} = \frac{1}{\tau_s - 1} \sum_t^{\tau_s} (\mathbf{x}_t^s - \mathbf{x}_\mu^s) \otimes (\mathbf{x}_t^s - \mathbf{x}_\mu^s) \quad (4.5)$$

The first two moments of the mixture $p(\mathbf{x})$ is

$$\mathbf{x}_\mu = \pi^s \mathbf{x}_\mu^s \quad (4.6)$$

$$\sum_{\mathbf{x}} = \sum_s^S \pi^s \left(\sum_{\mathbf{x}^s} + \mathbf{x}_\mu^s - \mathbf{x}_\mu \right) \otimes (\mathbf{x}_\mu^s - \mathbf{x}_\mu) \quad (4.7)$$

Finally, the shape changes is parameterized by $\mathbf{x} = \mathbf{x}_\mu + \sum_{i=1}^N \beta_i \phi_i$, here ϕ_i are N orthogonal basis vectors. By combining of the above shape and motion modeling, the liver shape at a specific time can be represented by

$$\mathbf{r}_\beta^\alpha = \mathbf{r}_\mu + \sum_{i=1}^M \alpha_i \psi_i + \mathbf{x}_\mu + \sum_{i=1}^N \beta_i \phi_i \quad (4.8)$$

Liver Correspondence Establishment

Before applying statistical model-based liver shape analysis in intra-operation phase, we need to establish the correspondence between all shapes of the reconstructed pre-operative 4D-CT images during the respiratory motion by defining a common topology, then apply the intra-operative data to compute the correct shapes for all time steps via non-rigid registration to navigate the surgery.

In the first step, we aim to establish the liver mechanical correspondence for each shape during the respiratory motion. Here we select the reference shape at full expiration status as the start (reference shape). Then, we align all the surface points of the reconstructed 3D shape using rigid registration at each time step during respiratory motion. The translation matrix T_s and rotation matrix R_s for each shape s can be computed by:

$$\arg \min_{T_s, R_s} \sum_{s=1}^n \|T_s R_s \check{\mathbf{r}}_s - \mu_0\|_2 \quad (4.9)$$

where μ_0 is the mean of all aligned points.

After aligning the shapes via rigid registration, we need to perform non-rigid registration to establish the correspondence among individual shapes during the respiratory motion. To reduce the bias of mean shape to the reference shape, we adopt an iterative group-wise registration [Jud et al., 2017] of the shape to establish the correspondence.

As the above liver correspondence is established for the shape s and time t , which is a temporal correspondence and must be along the motion sequence for each shape during the respiratory motion. For all individual time steps, we can register the reference shape using the deformation field obtained from non-rigid registration. Thus, the position of the surface point for each reconstructed shape can be obtained over time. Here, the final liver correspondence can be represented by the following registered shape vector:

$$\check{\mathbf{r}}_s = (\check{x}_{s,1}, \check{y}_{s,1}, \check{z}_{s,1}, \dots, \check{x}_{s,m}, \check{y}_{s,m}, \check{z}_{s,m})^T \quad (4.10)$$

Statistical Motion Modeling

After establishing the liver correspondence for all time step, we can replace the shape model term $\mathbf{r}_\mu + \sum_{i=1}^M \alpha_i \psi_i$ with a fixed reference vector:

$$\mathbf{r}_\beta^\alpha = \check{\mathbf{r}} + \mathbf{x}_\mu + \sum_{i=1}^N \beta_i \phi_i \quad (4.11)$$

By applying the offset between each sample shape and the reference shape, the motion model can be computed by:

$$\mathbf{x}_s(t) = \mathbf{r}_s(t) - \check{\mathbf{r}}_s \quad (4.12)$$

The arithmetic mean is:

$$\mu_s = \frac{1}{n} \sum_{i=1}^n \mathbf{x}_s(t) \quad (4.13)$$

The motion of liver shape can be represented as the data matrix by factoring the mean-free data of all liver shapes during the respiratory motion.

$$\mathbf{y}_i = \mathbf{x}_1(1) - \mu \quad (4.14)$$

$$\mathbf{Y} = [\mathbf{y}_1(1), \dots, \mathbf{y}_1(n), \dots, \mathbf{y}_{n_s}(1), \dots, \mathbf{y}_{n_s}(n)] \quad (4.15)$$

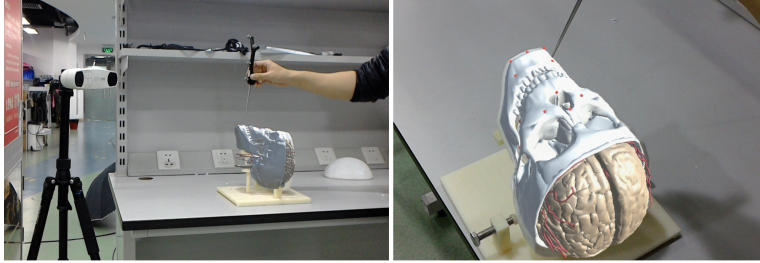


Figure 4.7: Automatic registration accuracy validation, red points are landmarks.

To compensate the respiratory motion, we need to acquire each landmarks' position at different time in the 4D CT images and use these position to model the inter-position during the movement of the liver. As shown in Fig. 4.3, we have labeled each landmark and correlate them to the landmarks on the 3D virtual model. By acquiring the markers' positions with the NDI tracking system, we can trigger synchronization and then predict the current time and shape of the liver via the estimated statistical model with respiratory motion compensation. By displaying the real-time position of the target tumor in the mixed reality environment, our system enables the "see through" navigation for the surgeons to accomplish the needle insertion.

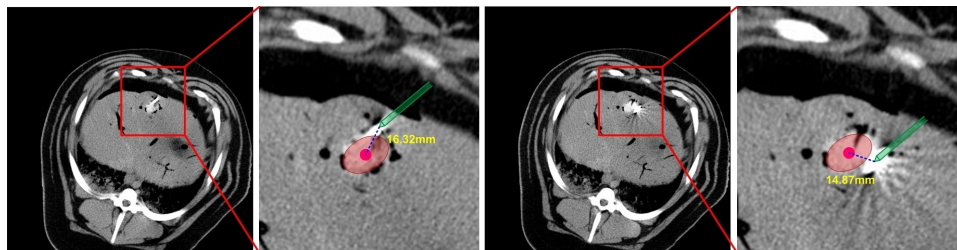


Figure 4.8: The results of traditional CT-navigated needle insertion.

4.4 Results

In the experiment, we conduct an animal comparison experiments between mixed reality-navigated needle insertion and traditional pre-operative CT imaging-navigated freehand needle insertion for liver RFA. The center of the tumor is set as the accurate target position for needle insertion. The animal experiment setting is as shown in Fig. 4.6 All experiments are conducted on a Microsoft HoloLens, NDI Polaris and a notebook equipped with Intel(R) i7-4702MQ CPU, 8G RAM and NVIDIA GeForce GTX750M.

4.4.1 Registration accuracy validation

In this section, we design an accurate 3D printed template and skull to validate the registration accuracy and verify the accuracy of our mixed reality-based navigation. In preparation, we build a 3D-printed skull with 10 landmarks which lies at a standard distance with high precision, and correspondingly label the 10 landmarks on the virtual skull model. In experiments, we first put the 3D-printed skull on the tracking area of the 3D tracking and positioning system. Based on the real and virtual scene registration by the HoloLens, the position of the landmarks on the 3D-printed skull and the virtual skull can be obtained. Here we check whether the virtual skull model is aligned with the 3D-printed skull, and calculate the relative position of the landmarks both by the tracking system and the virtual markers on the virtual skull. The distance between these two positions can be used to validate the accuracy of our system. Supposing the positions of the markers on the 3D-printing skull and template are C_1, C_2, \dots, C_n , the calculated positions of these markers with our method are C'_1, C'_2, \dots, C'_n . Then, the registration error can be computed by:

$$TRE = \sqrt{\frac{\sum_{i=1}^n \|C_i - C'_i\|^2}{n}}, i = 1, 2, \dots, n \quad (4.16)$$

The accuracy validation experiment is shown in Fig. 4.7, the real position and the registration position of all feature points are as shown in Tab. 4.1. The average target registration error (TRE) is 2.24 mm.



Figure 4.9: Mixed reality-navigated needle insertion.

4.4.2 Needle Insertion Comparison

In this section, we conduct an animal experiment of needle insertion. Based on real needle insertion for liver RFA procedure, we measure and compare the needle insertion accuracy using traditional CT-guided freehand operation and our mixed reality-navigated operation.

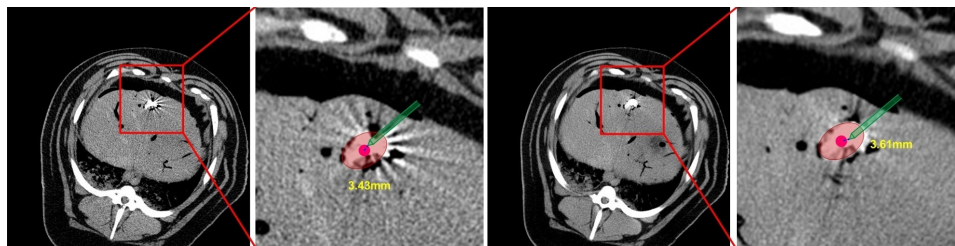


Figure 4.10: The results of our mixed reality-based needle insertion navigation.

Table 4.1: Performance statistics of automatic registration (*mm*).

Landmarks number	Real position of landmarks	Registered position of landmarks	Registration error
1	(57.31,-81.97,-808.93)	(57.12,-81.19,-809.26)	0.87
2	(59.25,-61.99,-808.53)	(59.53,-61.01,-809.87)	1.68
3	(60.05,-40.90,-809.51)	(63.21,-40.72,-811.14)	3.56
4	(59.52,-84.09,-833.63)	(60.80,-86.32,-832.86)	2.68
5	(60.65,-39.85,-834.71)	(60.78,-40.03,-835.77)	1.08
6	(41.02,-65.90,-882.98)	(41.59,-66.40,-880.14)	2.92
7	(83.00,-119.77,-902.75)	(82.02,-120.13,-903.07)	1.09
8	(43.72,-89.05,-895.05)	(44.63,-89.15,-892.14)	3.05
9	(45.77,-42.38,-891.80)	(46.54,-45.32,-892.44)	3.10
10	(34.41,-65.06,-905.00)	(33.64,-65.30,-907.25)	2.39

Fig. 4.8 demonstrates the traditional freehand needle insertion navigated by the CT images for 2 times. The surgeons need to observe and measure the position of the liver tumor in the pre-operative CT image, and then performs freehand needle insertion on the animal. The results in Fig. 4.8 demonstrate the needle insertion accuracy, which is 16.32 *mm* and 14.87 *mm*, respectively. The CT image navigation could only provide 2D images without visual cue of the internal structure of liver and tumors.

Fig. 4.9 illustrates the mixed reality-based navigation for needle insertion for liver RFA. By reconstructing the 3D model of animal abdomen and registering it to the real animal, we can clearly observe the internal structure of the animal abdomen, including the target tumors, which greatly facilitates needle insertion operation and reduces the operation difficulty. Also, surgeons can insert the needle via "See through" display, which benefits the surgeon to directly coordinate their vision and operation, and thus raising the needle insertion precision. Since the tip of the needle is invisible when it inserts into the liver, we display the tip of the k-wire in the holographic environment to clearly demonstrate the tip's position during the needle insertion, to provide accurate guidance for the surgeons. Fig. 4.10 illustrates the accuracy results of mixed reality-guided needle insertion for 2 times, which are 3.43 *mm* and 3.61 *mm*. With our mixed reality guidance, the surgeon can precisely insert the needle into the liver tumor.

Besides, for free-hand CT-guided insertion, the surgeon takes 25 minutes to finish the pre-operative CT scanning, tumor measurement and needle insertion. With our mixed reality method can achieve fast registration, and the surgeon takes only 5 minutes to finish the registration and needle insertion. This result demonstrates the effectiveness of our mixed reality-guided needle insertion.

4.5 Conclusion

In this paper, we propose a novel mixed reality-based surgical navigation modality to optimize the traditional image-based navigated modality for respiratory liver tumors punctures. The proposed mixed reality based navigation system enables us visualize a 3D preoperative anatomical model on intra-operative patient, thus providing direct visual navigation information and depth perception for the surgeons. Besides, with the aid of statistical motion model based respiratory motion compensation, surgeons can accurately insert the needle into the tumor, avoiding the error induced by the respiratory liver motion. We perform a comparison on an animal to show the difference between mixed reality based navigation and traditional CT imaging based navigation for needle insertion in in-vivo animal test. The experimental results showed the advantages of the mixed reality guided needle insertion for liver RFA surgery, which can assist the surgeons with simpler,

more efficient and more precise operation.

Errata

The Equation 4.2 to 4.2 on page 72 are updated as:

$$T_{Dis}^{Img} = T_{Dis}^{Tip} \cdot T_{Tip}^{Img}$$

The Equations 4.4 to 4.8 on page 74 and their corresponding explanations are updated as:

For each observed shapes with a amount of time τ , suppose each component follows the Gaussian mixture distribution $p(\mathbf{x}^s) \sim N(\mathbf{x}_\mu^s, \Sigma_{\mathbf{x}^s})$.

$$\mathbf{x}_\mu^s = \frac{1}{\tau_s} \sum_{t=1}^{\tau_s} \mathbf{x}_t^s$$

$$\Sigma_{\mathbf{x}^s} = \frac{1}{\tau_s - 1} \sum_t^{\tau_s} (\mathbf{x}_t^s - \mathbf{x}_\mu^s) \otimes (\mathbf{x}_t^s - \mathbf{x}_\mu^s)$$

The first two moments of the mixture $p(\mathbf{x})$ are estimated by

$$\mathbf{x}_\mu = \sum_{s=1}^S \pi^s \mathbf{x}_\mu^s$$

$$\Sigma_{\mathbf{x}} = \sum_s^S \pi^s (\Sigma_{\mathbf{x}^s} + (\mathbf{x}_\mu^s - \mathbf{x}_\mu) \otimes (\mathbf{x}_\mu^s - \mathbf{x}_\mu)), \text{ where } \pi^s = \frac{\tau^s}{\sum_s^S \tau^s}$$

Finally, the shape changes is parameterized by $\mathbf{x} = \mathbf{x}_\mu + \sum_{i=1}^N \beta_i \phi_i$, here ϕ_i are N orthogonal basis vectors of $\Sigma_{\mathbf{x}}$. By combining of the above motion model with a shape model, the liver shape at a specific time can be represented by

$$\mathbf{r}_\beta^\alpha = \mathbf{r}_\mu + \sum_{i=1}^M \alpha_i \psi_i + \mathbf{x}_\mu + \sum_{i=1}^N \beta_i \phi_i$$

where $\mathbf{r}_\mu + \sum_{i=1}^M \alpha_i \psi_i$ states for the shape model, and $\mathbf{x}_\mu + \sum_{i=1}^N \beta_i \phi_i$ represents the motion model.

Part IV

Surgical navigation based on holographic augmented reality

System for AR-based intuitive liver tumor puncture

Towards Quantitative and Intuitive Percutaneous Tumor Puncture via Augmented Virtual Reality

This chapter clarifies how the augmented virtual navigation system supports doctors in applying the tumor puncture precisely and efficiently in a quantitative and intuitive way. In the former chapters, Part II propose the method for percutaneous liver tumor thermal ablation planning with multi-constraints. Part III discussed how to involve the dynamic motion of the target region in the mixed reality pipeline. However, only if the mixed reality tumor puncture navigation system involves both the pre-planned path and the dynamic motion of the target region, can it support the surgeon in a quantitative and intuitive way.

In order to involve the path planning information in our augmented virtual reality pipeline, we determine the puncture feasible region for patients via merging the risk area of all the states in their respiratory cycle. And therefore, this feasible region is used for the intra-operative puncture path adjustment. For the puncture navigation, our system involves also the dynamic information and thus can apply both to the static phantom and the in-vivo animal. In the dynamic situation, the puncture navigation information, i.e. the pre-planned insertion path, is overlaid on the patient corresponding to a dynamic alignment strategy. This strategy contains both local and global transformation of all the utilities inside the surgical scenario. In order to guide the puncture needle intuitively and enhance the surgeon's depth perception of the needle insertion procedure, our system involves a user interface that offers variable vision cues for guiding the puncture starting at the correct insertion point and direction and towards the correct direction and depth. In the end, all the virtual navigation information displayed on OST-HMDs is aligned with the real surgical scenario and therefore supports the doctor performing the puncture along with the pre-operative surgical planning.

Each module in this system is validated either in a static phantom or

using in vivo data. Shenzhen People's Hospital provides the medical data for this work and performs the animal experiment under ethical approval. With the 4D-CT scanning of the anesthesia beagle dog, our method validates the artificial tumor position prediction result with k-fold cross-validation and leave-one-out cross-validation. The result shows that the pre-operative data is feasible to be used for the intra-operative tumor position prediction. The medical data and the experiment result also show that the quantitative needle trajectory optimization via constraint-based path planning method can compute feasible pre-operative planning that fulfills the medical requirement as well as the doctor's manually sketched ones. In addition, the pre-operative virtual surgical planning information can be precisely overlaid on surgical scenarios via a dynamic virtual-real alignment method with an error lower than the treatment needs. Besides, a user-friendly collaborative holographic interface for real-time 3D respiratory tumor puncture navigation is involved, so that our prototype can effectively assist surgeons in fast and accurately locating needles to the target step-by-step. Furthermore, as the time-consuming computations of the pre-operative planning and the real-time intra-operative tumor position estimation are performed on PC while only the well-organized navigation information is transferred to the HoloLens for visualization, our proposed system can reduce the computational burden on commercial OST-HMDs and extends their computational power via network transfer. Therefore, it gives more flexibility for clinicians and provides the potential for integrating more clinical information into the navigation.

Content of this chapter is published in the peer reviewed journal *Computerized Medical Imaging and Graphics*:

Ruotong Li, Yuqi Tong, Tianpei Yang, Jianxi Guo, Weixin Si, Yanfang Zhang, Reinhard Klein, Pheng-Ann Heng: Towards Quantitative and Intuitive Percutaneous Tumor Puncture via Augmented Virtual Reality. *Computerized Medical Imaging and Graphics*, 90(2021): 101905. <https://doi.org/10.1016/j.compmedimag.2021.101905>

Shenzhen People's Hospital provides the medical data and the experiment animal used in this article. Jianxi Guo and Yanfang Zhang are responsible for the medical image labeling, medical knowledge consulting and animal experiment performing. All the medical experiment was approved by the local ethics committee.

Contribution of the thesis author: Conceptualization, Methodology, literature review, algorithm implementation and validation, results interpretation and visualization, manuscript composition, validation experiment design.

Abstract

In recent years, the radiofrequency ablation (RFA) therapy has become a widely accepted minimal invasive treatment for liver tumor patients. However, it is challenging for doctors to precisely and efficiently perform the percutaneous tumor punctures under free-breathing conditions. This is because the traditional RFA is based on the 2D CT Image information, the missing spatial and dynamic information is dependent on surgeons' experience. This paper presents a novel quantitative and intuitive surgical navigation modality for percutaneous respiratory tumor puncture via augmented virtual reality, which is to achieve the augmented visualization of the pre-operative virtual planning information precisely being overlaid on intra-operative surgical scenario. In the pre-operation stage, we first combine the signed distance field of feasible structures (like liver and tumor) where the puncture path can go through and unfeasible structures (like large vessels and ribs) where the needle is not allowed to go through to quantitatively generate the 3D feasible region for percutaneous puncture. Then we design three constraints according to the RFA specialists consensus to automatically determine the optimal puncture trajectory. In the intra-operative stage, we first propose a virtual-real alignment method to precisely superimpose the virtual information on surgical scenario. Then, a user-friendly collaborative holographic interface is designed for real-time 3D respiratory tumor puncture navigation, which can effectively assist surgeons fast and accurately locating the target step-by step. The validation of our system is performed on static abdominal phantom and in vivo beagle dogs with artificial lesion. Experimental results demonstrate that the accuracy of the proposed planning strategy is better than the manual planning sketched by experienced doctors. Besides, the proposed holographic navigation modality can effectively reduce the needle adjustment for precise puncture as well. Our system shows its clinical feasibility to provide the quantitative planning of optimal needle path and intuitive in situ holographic navigation for percutaneous tumor ablation without surgeons' experience-dependence and reduce the times of needle adjustment. The proposed augmented virtual reality navigation system can effectively improve the precision and reliability in percutaneous tumor ablation and has the potential to be used for other surgical navigation tasks.

Keyword: Augmented Virtual Reality; Optimal Path Planning; Collaborative Holographic Navigation; Respiratory Tumor Puncture

5.1 Introduction

Radiofrequency ablation (RFA) is a minimal-invasive treatment for liver tumor ablation therapy. Doctors insert the ablation needle into the target

tumor and damage the lesion with high temperature. Such a procedure contains the steps of medical image acquisition, puncture path planning and puncture navigation [Lee et al., 2010, Kim et al., 2012].

Typically, the RFA treatment is guided by the medical images like computed tomography (CT), which can only provide 2D information with no spatial information. Besides, during the process of inserting the ablation needle into the target tumor, the surgeon needs to “looking up” the medical image displayed on the screen and imaging the spatial structure of the target area at the same time [Crocetti et al., 2016, Cazzato et al., 2016]. Moreover, CT can only provide the static structural information, while the dynamic information is in urgent need for real-time navigation. Although the other guided image modality, ultrasound, can provide dynamic information, the image quality is hard for surgeons to locate ablation needle in the target region. Therefore, the intra-operative dynamic information, such as the organ movement caused by physiological activities in the patient body, is hard for doctors to recognize.

Percutaneous puncture is a crucial step for RFA. Reasonable path planning in the preoperative stage can reduce the damage to the surrounding tissues and decrease the occurrence of complications after surgery. The optimal puncture trajectory should satisfy multiple clinical constraints, so that it is very challenging for doctors to mentally resolve this multi-objective optimization problem precisely, especially under the respiratory motion. Researchers has tried to use the constraint-based method for planning the surgical path by defining the hard and soft constraints [Seitel et al., 2011a]. Also the deformation of the needle and target region are took into consideration in the recent work [Hamz e et al., 2016]. However both of them apply this path planning result on an the respiratory patient.

Augmented reality technique, especially the invention of the optical see-through head-mounted display (OST-HMD) such as Microsoft HoloLens, Epson MoveRio or Google Glasses, makes it possible to align the virtual information with real-world scenario [Microsoft, 2016, Google, 2020, Seiko Epson Corp., 2020]. It is nowadays getting even more popular as it can enhance the depth perception. Employing the augmented reality technique into surgical navigation can provide the surgeon intuitive spatial information of the target area and resolve the hand-eye coordination problem at the same time [Wang et al., 2011, Grubert et al., 2018]. Therefore, the research on developing augmented reality based surgical navigation system attracts high attention from both academia and industry [Bernhardt et al., 2017b, Guha et al., 2017a].

In addition, considering that the visual system of human perceives the depth sense in surgical scenario via vision cues [Teittinen, 1993], for a safety tumor ablation, the depth of the needle tip during the puncture should be carefully perceived by the doctors. Incorporating reasonable vision cues in the surgical navigation system can help the doctor improve puncture ac-

curacy. In this regards, it is necessary to integrate appropriate user interface for surgical navigation system. There are many factors influencing on depth perception of human vision system, including accommodation, convergence, binocular parallax, monocular movement parallax, overlapping, etc[Teittinen, 1993]. Thus, researchers designed vision cues in augmented reality navigation system in order to enhance the depth perception. Besides, a user-friendly interface should also allow users to interactively select their preferred cues.

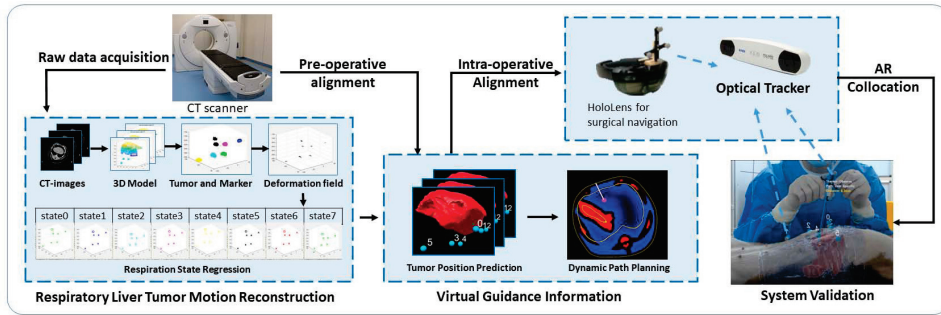


Figure 5.1: The pipeline of our augmented virtual reality based respiratory liver tumor puncture. In the pre-operative stage, we build up the patient-specific anatomical model during the respiration and compute the correlation model between the internal tumor position and the position of the external marker. Then we real-timely predict the tumor position, planning the insertion path and dynamically overlaying the virtual guidance information on the patient body at expected position. Thus the surgeon can apply the tumor puncture while wearing HoloLens.

This paper presents an augmented virtual reality technique for liver tumor puncture under respiratory activity. The overview of our system is shown in Fig. 5.1. In our prototype, we first construct patient-specific anatomical structures and predict tumor position with an internal-external correlation model. Then we generate the tumor puncture path automatically with a 3D signed distance field fusion method together with multi-objective optimization. Besides, to precisely provide the navigation information in the augmented reality system, all the utilities in the operation scenario are attached with the optical tracker and coordinated under the optical tracking system. With the virtual-real alignment, the virtual guidance information can be superimposed onto the corresponding area of patient body. For quantitatively measuring the puncture process and enhancing the depth perception, we also integrate way-point visual cue into our guidance information. With our augmented reality guidance modality, surgeons can more intuitively locate the target tumors in a more efficient and accurate manner. Further more, as we perform the time-consuming computations of

pre-operative planning and intra-operative tumor position estimation on PC and then transfer the well-organized target information to HoloLens, our system can effectively reduce the computational burden on present commercial HMDs and extend their computational power via network transfer. Besides, this strategy allows us providing more complex but intuitive navigation information for clinicians. Our main contributions in this paper are:

- We propose a constraint-based puncture path planning method to quantitatively define the optimal needle trajectory.
- We propose a dynamic virtual-real alignment method to achieve the precise augmented visualization of virtual information being overlaid on surgical scenario.
- We design a user-friendly collaborative holographic interface for real-time 3D respiratory tumor puncture navigation, which can effectively assist surgeons fast and accurately locating the target step-by-step.

5.2 Related Work

In the traditional image-based RFA navigation, doctors have to place the needle into the target tumor with the guided 2D image. CT images can provide more clear guidance images, but cannot provide real-time intra-operative guidance. Ultrasound is quite popular for intra-operative monitoring as it is possible to observe the operation process and providing real-time medical images [Rhim et al., 2008, Lee et al., 2010, Kim et al., 2012], however the shortage is also quite obvious as the image of ultrasound is not clear enough to distinguish the tissue structure and the artifacts induced by the needle can also interfere the surgeon’s judgment [Livraghi et al., 2011]. Besides, the “Heads up” display of 2D intra-operative guided images further increases the operation difficulty and reduces the operation precision, since it lacks direct coordinating of surgeons’ hands with the vision [Crocetti et al., 2016, Cazzato et al., 2016].

In the traditional RFA therapy, surgeons employ the pre-operative medical image for surgical planning. The pre-operative planning is done based on these medical images by finding the appropriate path for the percutaneous puncture, which will be recorded in doctors’ mind. In the surgery, the surgeons perform the percutaneous puncture based on this pre-planned puncture path. Thus, the outcome of this surgery is quite dependent on the experience of the doctors [Mauri et al., 2015, Crocetti et al., 2016, Cazzato et al., 2016].

In recent years, to improve the accuracy of image-guided surgery, the augmented reality technology is introduced in surgical navigation. Among these, Philips developed an augmented-reality surgical navigation system to assist traditional image-guided minimally-

invasive surgical guidance by combination of 3D X-ray imaging and optical imaging to provide surgeons with a unique augmented-reality view of the inside and outside of a patient during surgical procedures [Swiss Society of Virtual and Augmented Reality, 2017]. However, it is still not convenient enough for doctors since hand-eye coordination is another requirement for doctors. Optical see-through head-mounted display (OST-HMD), can well tackle this hand-eye coordination issue, as it can provide the on-patient see-through guidance modality and enhance the surgeon’s perception of the depth and spatial relationships of surrounding structures through the augmented reality based fusion of 3D virtual objects with real objects [Bernhardt et al., 2017b, Guha et al., 2017a]. Novarad’s Open-Sight augmented reality system is the first solution for Microsoft HoloLens cleared by the FDA for medical use [Novarad Healthcare Imaging, 2019]. Scopis also developed an augmented reality guided operation navigation system for spine and dental operations [Scopis Inc., 2017]. Nowadays, a lot of researchers have developed augmented reality navigation systems for different medical applications [Xie et al., 2017, Qian et al., 2018], but their guidance information is in static mode, which is not suitable for applications in dynamic conditions, like free breathing.

With the development of human-computer interaction techniques, researchers designed different user interfaces in the augmented reality surgical navigation system, for improving the surgical precision used in augmented reality based surgical scenario. Especially for minimal invasive operation, the vision cues are chosen aims to provide more intuitive information of the operation starting position, operation instrument pose and the needle insertion depth of the operation utilities. The vision cue for accurate puncture contains the information for measurement accuracy of insertion position and direction, which are usually denoted in different color code [Liu et al., 2018]. The puncture direction and utility depth information is another task that vision cue should represent after the needle being inserted into the patient body [Zhou et al., 2019, De Paolis and De Luca, 2019]. Most of the vision cues give the color to denote the direction different. However, this kind of cue cannot guide surgeons locate the correct path. The task will become even more challenging when the needle tip being away from the target.

5.3 Virtual Reality Based Optimal Puncture Path Planning

We proposed the constraint-based method to quantitatively plan the virtual puncture path. This planning process determines the needle insertion position on the external skin, through which doctors can safety approach to the target tumor without hurting the critical regions. In this paper, we automatically planning the puncture path at a specific static state that chosen

as the reference state for pre-operative planning.

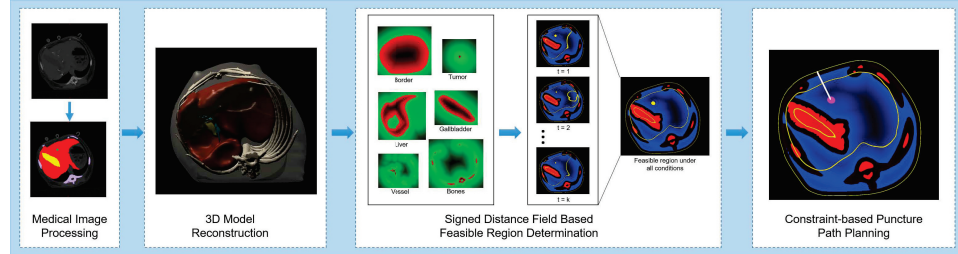


Figure 5.2: The process of virtual puncture path planning. First, we process the medical images and reconstruct the 3D model of the patient abdominal region. Then compute the signed distance function parts and determine the feasible region under all conditions. The last step performs the result of constraint-based puncture path planning. 3D Model Reconstruction: Dark red denotes the liver, yellow object illustrates the gallbladder and the green object shows the vessel that goes into liver. Signed Distance Field: Green denotes plus value (point outside the structure), and red denotes the minus value (point inside the structure). In the feasible region determination step: Red is Obstacle, Blue is Feasible region for puncture path, dark gap between red and blue is the unfeasible region for puncture. Yellow denotes the boundary of phantom structures and the tumor.

As shown in Fig. 5.2, the process starts with medical image processing for the 3D anatomical model reconstruction of the patient abdominal region, with which we can define the signed distance field (SDF) for each anatomy. Then, we fuse the feasible region for puncture based on the 3D signed distance field at different time. After that, the optimal puncture path in this feasible region is calculated via a constraint-based optimization. In the intra-operation stage, the puncture path is discretely presented with way points, the small points evenly located between the percutaneous insertion position and the puncture target point.

5.3.1 Patient Specific 3D Model Reconstruction

For planning a patient-specific path for percutaneous puncture, we first build up the 3D anatomical model. In this paper, we planned puncture path for both the static 3D abdominal phantom equipped with artificial liver tumors and the vivo beagle dog with artificial liver tumor. The CT-images are used for 3D reconstruction for structures in the phantom and dog.

Here we employ the Materialise Mimics software to manually segment the CT images of the abdomen into different tissues and accurately reconstruct the 3D geometries of the patient-specific model, including the liver, tumor, spine, ribs, gallbladder and the vessels in liver. The 3D models are denoted

with $M = (V, E)$, where V is the set of vertices (in CT-image coordinate) on the model surface and E is the set of edges (forming the triangles). After this, we rasterized the 3D meshes into voxels for the next step of computing.

5.3.2 SDF-based Feasible Region Determination

Here the structures are labeled with three different types: target Tar , obstacle Obs and safety tissue $Safe$. The artificial tumor in phantom and in the experimental animal are labeled as Tar . The structures that needle cannot insert are labeled as Obs , including the hard obstacles like bones and the critical region for punctures, such as gallbladder, large vessel. $Safe$ denotes the other tissues that the needle can insert, like the liver itself, skin and the muscles in the surrounding area.

We define the feasible region as the safe region for needle insertion, here we follow the doctors' suggestion and define the larger region with a threshold θ_{safe} from the Obs structures. The feasible region is determined via SDF fusion of the $Safe$ and Obs structures. The signed distance field of a structure is computed with the signed distance function, which measures the distance from each voxel to its nearest boundary of a 3D object. For a voxel inside the object, its corresponding distance is marked with a sign of minus and for the voxel outside the object vice versa. The Feasible Region $R_{feasible}$ is a compute as:

$$SDF_{region} = \begin{cases} \min(SDF_{Obs}) & \min(SDF_{Obs}) \leq 0 \\ \min(SDF_{Obs}) - \theta_{safe} & \min(SDF_{Obs}) > 0 \end{cases}$$

$$R_{feasible} = \begin{cases} true & \text{if } SDF_{region} > 0 \\ false & \text{if } SDF_{region} \leq 0 \end{cases} \quad (5.1)$$

The fusion of the SDF takes the value for each voxel from the SDF of the feasible and unfeasible structures respectively and the value of each voxel takes the minimum value among those in the SDF for the same type of structures.

However, for the vivo beagle dog, the position and shape of the obstacle and the critical region are changing with the respiratory motion. In order to take all the risk into consideration, a voxel is considered as feasible only if it is feasible under all of the conditions. In this case, the feasible region is computed from the fusion of feasible sequence of the target area at different moment t_i :

$$R_{feasible} = R(t_1)_{feasible} \& R(t_2)_{feasible} \& \dots \& R(t_n)_{feasible} \quad (5.2)$$

5.3.3 Constraint-based Puncture Path Optimization

We define the puncture path $\vec{d} = (P_{In}, P(t)_T)$, a vector from the insertion position P_{In} on the external skin to the tumor position $P(t)_T$ at time t . As

Input: Feasible region $R_{feasible}$, tumor position $P(t)_T$.

Output: optimal puncture direction \vec{d} for needle insertion.

1: **Needle Pose Initialization:**

initialize the path direction \vec{d}_0 in axial plane, perpendicular to the skin.

2: **Initial variables:**

$dSet, List_d = empty, List_E = empty$

3: **Iteratively find the optimal puncture path:**

For each \vec{d}_i **in** $dSet$:

If $C_{Obs} = \text{infinity}$:

next \vec{d}_i ;

Else if $C_{Obs} = 1$:

$List_d \leftarrow \{List_d; \vec{d}_i\}$;

If $E(d_i) < E(d_0)$:

$List_E \leftarrow \{List_E; < E(d_i), \vec{d}_i >\}$;

4: **Update $dSet$ until reach the maximum iteration:**

$dSet \leftarrow sampling_around(List_d)$;

goto Step. 3;

5: **Return result:**

The puncture direction in $List_E$ with a minimum energy value $E(d)$ is the result direction \vec{d} .

Algorithm 3: Puncture Path Optimization.

the tumor location at a specific time is fixed, our optimal algorithm aims at finding the optimal direction of the puncture path, so that the corresponding insertion position on the external skin has to be determined.

As shown in the Algorithm. 3, we start from initializing the puncture direction \vec{d}_0 . According to doctors' experience, the direction perpendicular to the external skin on axial plane (0°) is the most convenient puncture direction. Then the algorithm traverses the directions in an initial candidate direction set $dSet$, which contains different puncture directions at angles from -90° to 90° with step size of 1° on the axial plane. The algorithm calculates the energy for each puncture path in the candidate direction set and then updates the $dSet$ with the feasible path for the next round of iteration. In iterative process, we only store the directions whose energy (calculate by Eq. 5.3) smaller than initial direction's into the energy list $List_E$. The direction with smallest energy in the list is our optimal puncture direction.

The calculation of energy function is based on our defined feasible region (Sec. 5.3.2). The puncture path passes through the phantom from the external insertion position to the target tumor center. Therefore, it can be considered as a combination of a set of voxels $vPath$. We defined energy function with constraints to evaluate the quality of the puncture path as

following:

$$E = C_{Obs} \cdot \sum_{i=N_{type}(1)}^{N_{type}} \lambda_i \cdot C_i \quad (5.3)$$

Where C_{Obs} evaluate the feasibility and safety of a puncture path. Our motivation is to optimize any voxels on puncture path achieving at least the distance of θ_{safe} from the Obs region in order to have a safe puncture, which is determined by checking the value $R_{feasible}$ of each voxel along the puncture path. If any of the voxel on the needle path is inside the non-feasible region, the path is invalid.

$$C_{Obs} = \begin{cases} 1 & \text{if } R_{feasible}(vPath) = true \\ \text{infinity} & \text{if } R_{feasible}(vPath) = false \end{cases} \quad (5.4)$$

The N_{type} is an enumerated type for the type of the constraints including $\{len, pAbd, dir, \dots\}$, which indicates the type of different constraints that involves into the energy function. Here i denotes its index, λ_i is the corresponding weight for each type of constraint C_i . In our method, the following constraints are taken into consideration:

C_1 is the needle length constraint C_{len} , which penalizes the path with longer insertion and makes sure it is no smaller than the threshold θ_{length} at the same time.

$$C_{len} = \begin{cases} \frac{\|\overrightarrow{P_{In}P(t)_T}\|}{\|\vec{d}_0\|} & \text{if } \|\overrightarrow{P_{In}P(t)_T}\| \geq \theta_{length} \\ \text{infinity} & \text{if } \|\overrightarrow{P_{In}P(t)_T}\| < \theta_{length} \end{cases} \quad (5.5)$$

Where $\|\overrightarrow{P_{In}P(t)_T}\|$ is the length of the puncture path from insertion position to the tumor center at time t . $\|\vec{d}_0\|$ is the length of the initial path with puncture direction \vec{d}_0 . The threshold θ_{length} is the minimum insertion length that the tissue can hold up the needle. This constraint makes sure that the length of the puncture path should be as small as possible, after it fulfills the θ_{length} requirement.

C_2 is the abdominal penetration constraint C_{pAbd} , which represents the passes of abdominal cavity that ablation needle passes through.

$$C_{pAbd} = \frac{\|\overrightarrow{Path_{AbdCavity}}\|}{\|\overrightarrow{P_{In}P(t)_T}\|} \quad (5.6)$$

In order to avoid damaging other organs inside the patient's abdomen, the line from insertion point to liver surface $\|\overrightarrow{Path_{AbdCavity}}\|$ should be as small as possible.

The C_3 is the puncture direction constraint C_{dir} . It rewards the needle direction closer to the perpendicular direction to the external skin, and

penalizes the puncture path which is not parallel to the axial plane of the Phantom.

$$C_{dir} = \frac{\overrightarrow{P_{In}P(t)_T} \cdot \vec{d}_0}{\|\overrightarrow{P_{In}P(t)_T}\| \cdot \|\vec{d}_0\|} \quad (5.7)$$

For the respiratory condition, we compute the puncture path for a specific state and remark the state as a reference state for the starting navigation. Later in the intra-operative navigation, this pre-planned path will be aligned with the corresponding intra-operative reference state and updated dynamically with the changing of tumor position. Details for dynamic alignment for the respiration state in the intra-operative stage is explained in Sec. 5.4.3.

5.4 Augmented Reality Based Respiratory Tumor Puncture Navigation

In order to achieve the precise augmented visualization of the virtual navigation information, we first calibrate our system with optical tracking devices so that the virtual anatomical model can correctly be superimposed onto the patient. After that, we predict the dynamic organ behavior under free-breathing conditions via correlation model. Finally, we dynamically align the guidance information on the surgical scenario.

5.4.1 Static Virtual-Real Alignment

The surgical navigation system is calibrated by the optical tracking system NDI Polaris. In the surgical scenarios, each operation utility is attached with an optical marker, which can identify the position and rotation of each tools. In this way, we can unify the coordinates from different utilities.

Fig. 5.3 illustrates the collocation process of our AR prototype. For each utility, we adopt two steps to achieve the precise system calibration, which are global and local transformation.

We first perform global transformation from utility to the world coordinate. The world coordinate of the utilities in surgical scenario can be computed by applying the projection from tracking devices to the platform coordinate T_{Tra}^{Pla} , which can be computed according to the coordinate definition.

Then we compute local transformation from device coordinate to the optical tracking coordinate by calculating $T_{Uti}^{Tra} = \{T_{TNe}^{Tra}, T_{TAni}^{Tra}, T_{TDev1}^{Tra}, T_{TDev2}^{Tra}\}$, which is the transformation between the utility and optical marker. For each of the utilities, their pose in the world coordinate can be represented as:

$$T_{Uti}^{World} = T_{Tra}^{Pla} \cdot T_{Uti}^{Tra} \cdot T_{Uti} \quad (5.8)$$

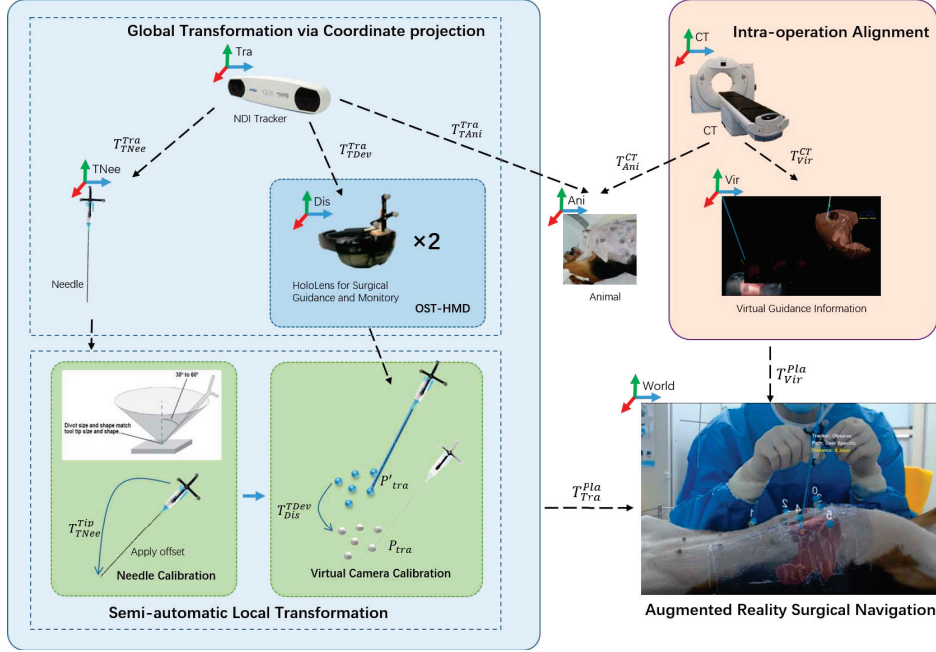


Figure 5.3: Coordinate transformation for system configuration.

Since each of the utilities has different properties, the calculation of T_{Uti}^{Tra} is performed in different ways. The ablation needle is fixed with a tracking marker on the needle tail, thus T_{TNe}^{Tip} denotes the offset from needle tip to the optical marker. The offset is obtained by tracking the marker pose while applying a needle pivot behavior with needle tip fixed.

The virtual scenario displayed on the OST-HMD can be considered as the shooting of the virtual environment via virtual camera moving under the world coordinate. Since the display devices are equipped with tracking markers fixed on them, the pose and location of the virtual cameras can be obtained by a coarse-to-fine alignment process. Such an alignment contains the transformation from the tracking marker pose to the camera pose T_{Tra}^{Dis} and an error ϵ which can be fixed by manually adjustment step.

Consider a set of optical sphere markers in the real environment with position $P_{tra} = \{p_1, p_2, \dots, p_n\}$ and their position observed by the virtual camera is $P'_{tra} = \{p'_1, p'_2, \dots, p'_n\}$. The position of the needle tip is known after needle calibration, so that we can get the markers position in both scenarios by touching the marker point in both real and virtual environment with the needle tip respectively. We calculate the transformation T_{Dis}^{TDev} from the P'_{tra} to P_{tra} , thus the virtual camera transformation T_{Tra}^{Dis} is its inverse. To precisely superimpose the virtue scenario on the reality scene, we perform a manually delicate step after the calibration in order to eliminate the influence by user difference, like pupil distance or focal length of eyes.

5.4.2 Respiratory Motion Modeling of Target Region

The physiological activities causes dynamic motion of the organs and tissue all the time. A precision puncture should take this affection into consideration. In this regards, we construct a statistical model [Jud et al., 2017] to represent the organ motion. In order to model the complicated practical surgical scenario, our framework is defined under following assumptions based on doctor’s experience:

- Dynamic motion of the organ is caused by the respiration.
- The animal’s respiration motion after anesthesia can be regarded as periodical cycle.
- We consider the position and displacement of the tumor, liver and surface markers at a specific time always following the Gaussian distribution.
- The internal-external respiration motion has a correlation, i.e. at a certain time, the internal tumor position and the external surface marker displacement should at the same respiratory state.

We predict the motion with a correlation model between the external skin markers and the internal tumor movement [Jud et al., 2017]. During the navigation, we use the state which we used for path planning as the reference state and then align the respiration cycle with this state as starting point.

Raw medical data acquisition and processing

We employ a Beagle dog to perform the animal experiment. To accurately construct the spatial information between liver, tumor and ribs, we place 6 NDI surface marker as landmarks on the skin (near the ribs) shown in Figure 5.4. The ground truth of the respiratory motion is obtained via 4D-CT imaging, which records the deformation and displacement of the internal organ together with the surface marker under the free-breathing respiratory motion. At the same time, we continuous tracking the surface marker with the optical tracking system.

Then we reconstruct the patient-specific liver, tumor and the surface marker on the dog’s skin under CT image coordinate, which is the coordinate of the captured medical images. Marker locations $S_M(t) = \{s_1(t), \dots, s_n(t) | s_i(t) \in \mathbb{R}^3, t \in \mathbb{R}_+\} (n = 6)$ and the tumor location $S_T(t) \in \mathbb{R}^3, t \in \mathbb{R}_+$ under the CT device coordinate are calculated from the center of the patient-specific 3D model. The surface marker position $O_M(t) = \{o_1(t), \dots, o_n(t) | o_i(t) \in \mathbb{R}^3, t \in \mathbb{R}_+\} (n = 6)$ under the world coordinate is obtained from the optical tracker. With this procedure, we acquired the marker movement in both CT image coordinate and world coordinate.

The marker locations obtained by CT can map into the world coordinate by applying the transformation T_{CT}^{Pla} .

We analyze the continuously captured periodical marker movement with tracker tracked location data $O_M(t)$ to get the average marker movement period $\bar{O}_M(t)$. Then, we sort the CT-extracted marker position $S_M(t)$ and its corresponding tumor position $S_T(t)$ by placing its mapping $S'_M(t)$ in the proper order which follows the movement in $\bar{O}_M(t)$. After that, we perform the data augmentation via spline interpolation, which allows generating complete respiration sequences for external makers and tumor.

$$\left\{ \begin{array}{l} \dots \\ p(t_i) = a_i * t_i^2 + b_i * t_i + c_i \\ p(t_i) = a_{i+1} * t_i^2 + b_{i+1} * t_i + c_{i+1} \\ p(t_{i+1}) = a_{i+1} * t_{i+1}^2 + b_{i+1} * t_{i+1} + c_{i+1} \\ p(t_{i+1}) = a_{i+2} * t_{i+1}^2 + b_{i+2} * t_{i+1} + c_{i+1} \\ \dots \\ 2 * a_i * t_i + b_i = 2 * a_{i+1} * t_i + b_i + 1 \\ 2 * a_{i+1} * t_{i+1} + b_{i+1} = 2 * a_{i+2} * t_i + 1 + b_i + 2 \\ \dots \end{array} \right. \quad (5.9)$$

Where $p(t_i)$ is the position of marker or tumor at time t_i the parameter a_t , b_t and c_t is the corresponding parameter for spline. Traditionally, second order derivative of both ends on the 2nd order spline equals to 0, which leads to none smoothness of both ends. But in our case, the movement of markers and tumor in respiration is a repeated process, which makes sure that our interpolation of our spline is smooth at every central point including both ends. We solve the system of simultaneous equations for the parameters. Then, we sample points uniformly on the spline to get the data $s_{M,T}(t)$ for next step of computation.

Tumor position prediction via internal-external correlation

In order to provide precise navigation information to the surgeon, we construct the respiratory motion of surface markers and tumor via statistical motion model. In this paper, we build up the correlation between liver tumor movement and the surface marker displacement in respiration, so that the tumor position can be predicted by observing the external markers movement.

We assume that the respiration motion is a regularly alternating exhalation and inhalation process. Our algorithm computes the mean state of the states in the respiratory cycle as a reference $\bar{s}_{M,T}$. Thus the movement of the tumor and markers at any moment t can therefore be represented as a vector field from this reference state to their real-time position.

Since we assume the position of the tumor and markers at each state follows the Gaussian distribution, their position displacement can be rep-

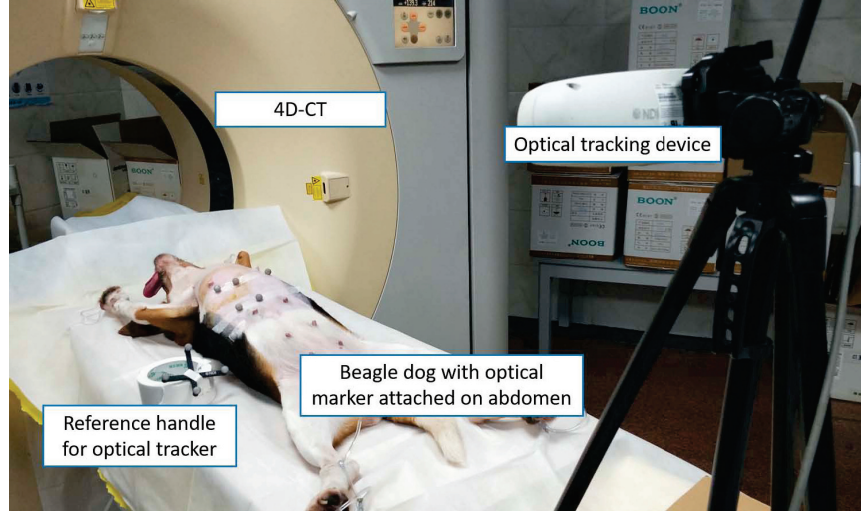


Figure 5.4: The scenario for raw medical data acquisition of the experimental animal.

resented as a mixture of Gaussian distributions of different respiration states. In our work, the respiration cycle is regressed into eight states $\{\Delta s_{M,T}(t_1), \dots, \Delta s_{M,T}(t_8)\}$ (shown in Figure 5.1). Therefore, we can represent the periodic motion of liver tumor and surface markers as a linear combination \mathbf{c} of these states.

$$\Delta s_{M,T}(t) = s_{M,T}(t_0) + \mathbf{c} \cdot \Delta S_{M,T}(t_n), \quad t_n \in \{1, 2, \dots, 8\} \quad (5.10)$$

$$\mathbf{c} = (c_1, \dots, c_n), \quad n = 8$$

where the $s_{M,T}(t_0)$ is a reference state of the intra-operative respiration, \mathbf{c} is a vector of coefficients to represent the current breathing state and $\Delta s_{M,T}$ is a vector of 8 respiratory states.

As we assumed that the tumor position and the external skin markers displacement are always at the same respiration state, so that the breathing state of the intra-operation tumor can be computed easily by least square regression of the external marker position:

$$O'_M(t) = S_M(t_0) + \mathbf{c} \cdot \Delta S_M(t_n) \quad (5.11)$$

where $O'_M(t)$ is the real time position of the skin markers that observed by the optical tracking system and $S_M(t_0)$ is the intra-operation reference position of the external markers. Thus, the tumor position at the corresponding time is predicted as:

$$s_T = s_T(t_0) + \mathbf{c} \cdot \Delta s_T(t_n) \quad (5.12)$$

where the $s_T(t_0)$ is the tumor position at the intra-operative reference state, and \mathbf{c} is the breathing state computed with Eq.5.11.

5.4.3 Intra-operative Dynamic Alignment

Considering that it is safer for surgeon and surgical assistant being equipped with OST-HMD to observe the respiratory liver tumor from different views, we present a dynamic alignment method for each of the OST-HMD to perfectly superimpose pre-planned navigation information onto the surgical region in situ. This specific implementation contains a model adjustment step and a navigation information dynamic update step.

As the surgical navigation information is built up depend on the pre-operative CT-scanning data, the pre- and intra- operative alignment is necessary in our system. In order to resolve the pose difference of the patients and adjust the pre-operative model to suit the intra-operative scenario, a transformation from the patients pre-operative pose in the medical data acquisition phase to the intra-operative pose $T_{CTPre}^{CTIntra}$ is applied to the motion model. This transformation can be easily achieved using the intra-operative CT scanning data.

While doing the inter-operative tumor prediction, the markers displacement captured with the optical tracking system needs to transfer to the coordinate of the constructed model. We apply T_{Tra}^{CT} , which is the transformation from intra-operative observing tracker to the CT device coordinate that we used for motion modeling.

In order to dynamically update the navigation information of the pre-planned puncture path, use the average state of the intra-operative as the reference state for surgical staring. Then aligned the pre-planned puncture path at the corresponding state. During the navigation, the insertion position P_{In} is fixed, while the target position P_T updates with the tumor position prediction result.

In the end, all the navigation information needs to map the world coordinate in order to provide the proper information for the navigation system via transformation T_{CT}^{Tra} . Display of the virtual guidance information on HoloLens according to $Display = T_{Pla}^{Dis} \cdot T_{Vir}$ where $T_{Vir} \in \{T_{Nee}, T_{Ani}, O_{M,T}(t)\}$.

5.5 User-friendly Collaborative Interface Design

In order to effectively assist surgeons in inserting the ablation needle into target, our system designed a user-friendly collaborative holographic interface, which integrates several visual cues to enhance the depth perception.

5.5.1 Vision cue for accurate insertion

In order to give surgeons intuitive navigation information during the puncture, we design several visual cues that provides quantitative navigation

information for improving the precision of needle insertion including the cues for insertion position, direction and puncture depth.

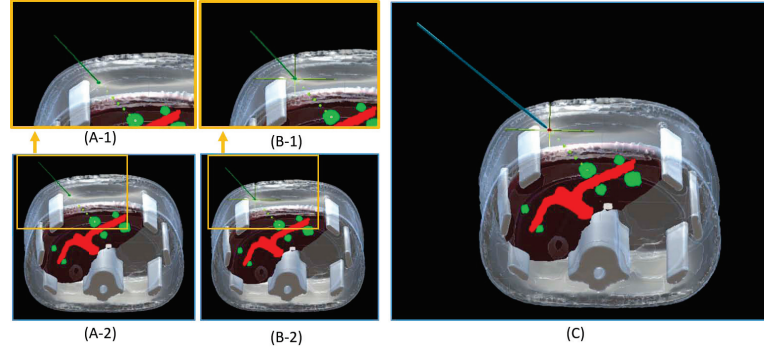


Figure 5.5: Blue pole: virtual needle; Green pole: reference for insertion direction. A: The insertion position illustrates with a green sphere with delimiter $d = 1mm$ the green line attached to it denotes the puncture direction. B: The fine green lines intersecting at the insertion point are the reference lines, which provides users with more intuitive spatial information. Users can hide the line if they prefer to have a cleaner interface. C: The color of the sphere changes into red, when users locate the needle tip accurately at the insertion point.

Needle Tip Localization

The first step for an accurate puncture is to localize the needle tip on the correct insert position. In our augmented reality navigation system, the insertion position is illustrated as a sphere with perpendicular intersection lines (shown in Fig. 5.5). It can help surgeons determine the needle direction by changing the color from green to red when the needle tip approaches the center sphere with an error lower than $1mm$.

Puncture Direction Navigation

In order to help surgeons insert the needle along the planned path precisely, our navigation system involves different type of visual cues for pre- and intra-puncture process. Before needle is inserted into the external skin, the insertion direction line and virtual protractor can help the surgeon find the accurate insertion direction (see Fig. 5.6). While in the intra-puncture process, the way point is used for needle direction correction and puncture monitoring (shown in Fig. 5.7).

When the needle tip is located at the insert position, a protractor appears to quantitatively display the precise puncture direction. The center of this protractor aligns with the insert position and locates on the plan the same

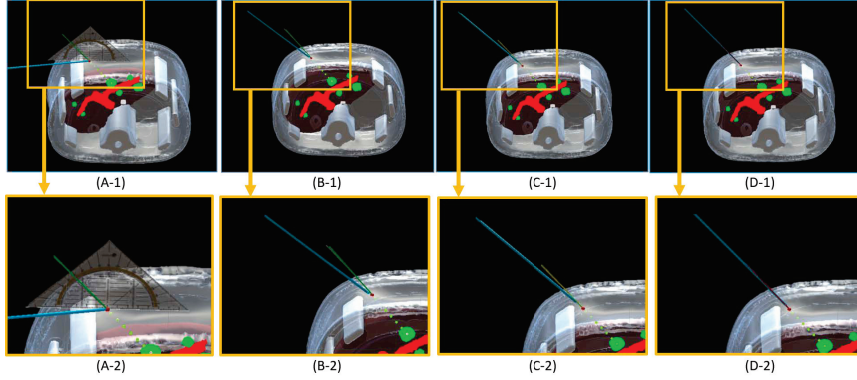


Figure 5.6: Blue pole: virtual needle; Green pole: reference line for insertion direction that pre-planned. (A): A virtual protractor displays when the needle tip approaching the target position, which shows the explicit direction of the puncture path. This virtual protractor can be hidden by users when they prefer a cleaner interface. (B-D): The color of the insertion direction line changes while the needle direction approaching closer to the pre-planned insertion direction. The color of the insertion reference line is quantitatively determined with 5.13. The lower row is the zoom in of the yellow squared region of the upper row image.

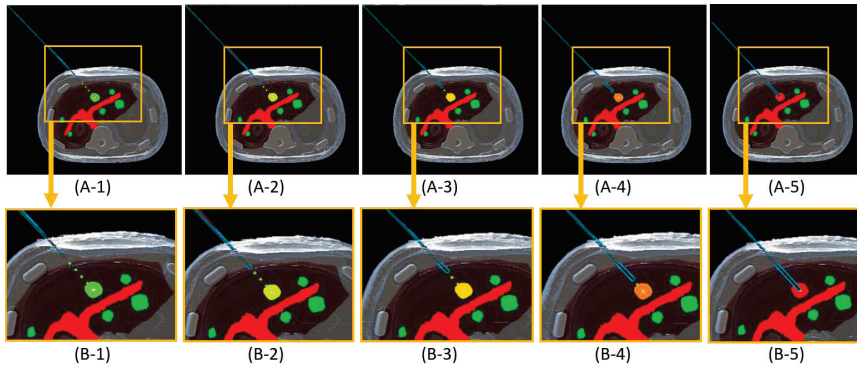


Figure 5.7: Blue pole: virtual needle. The monitoring of the puncture using way point. The way points are located on the puncture path with distance of 1cm. When the needle tip passes through a way point, the color of this way point changes from green into red. The color of the target tumor changes from green to red based on the color code corresponding to the distance from needle tip to tumor center. The lower row is the zoom in of the yellow squared region of the upper row image. The needle inside the liver is rendered only the outline.

as the puncture direction line. The color of the direction line corresponds to the direction accuracy of the needle puncture. The angle between needle and the direction of the planned puncture ΔA determines the color of the direction line shows in the vision:

$$color = \begin{cases} red & \Delta A < \theta_{near} \\ yellow & \theta_{near} < \Delta A < \theta_{far} \\ green & \Delta A > \theta_{far} \end{cases} \quad (5.13)$$

here we define θ_{near} as the acceptable threshold for puncture and θ_{far} as the threshold that when the needle direction is too far away from the pre-planned path. In our system we choose the value $\theta_{near} = 2^\circ$ and $\theta_{far} = 5^\circ$.

During the intra-puncture process, the needle direction is monitored with way-point. The way-points are a sequence of sphere with diameter of 1mm which locates on the path between insert position and the center of target tumor. The way points locates either evenly with distance of 1cm between each other or at a specific anatomy structure. Surgeons can easily monitor the needle direction and check whether the direction of needle is aligned with the way point sequence.

Intuitively Percutaneous Puncture Navigation

For giving surgeons intuitive depth information of the needle puncture, the system use transparent material for the model rendering, which makes the user easily to observe the anatomic structures inside the model. A special rendering effect of needle shows in Fig. 5.7 also enhance the depth perception. This effect makes the needle rendered only boundary while it is inside the tissue. Therefore gives intuitive puncture depth for user.

Besides, the way-point can also help the user determine the puncture result. While puncturing, the needle tip go through the way points one after another. When the needle tip go through these points, the corresponding way point will switch the color from green to red. As the way points either locates evenly with distance of 1cm or at specific anatomy structure, the surgeon can easily measure the needle insertion depth by counting the number of way point it goes through or checking if it arrives a specific anatomic structure.

Other than these, the tumor colors green when it further than the tumor-insertion distance. During the needle tip towards to the tumor, the tumor color change from green to red clockwise along the HSV color wheel.

5.5.2 User Interface Integration

Our navigation system integrates all of these visual cues into the collocated user interface. For providing more intuitively real-time navigation information, more user-friendly elements are integrated into the visualization

interface. For example, the device mode gives information of the view point of the device, which can switch viewing point between the surgeon and the surgical assistant. Path label tells doctors pick among the paths which is generated by different parameter in Sec. 5.3.

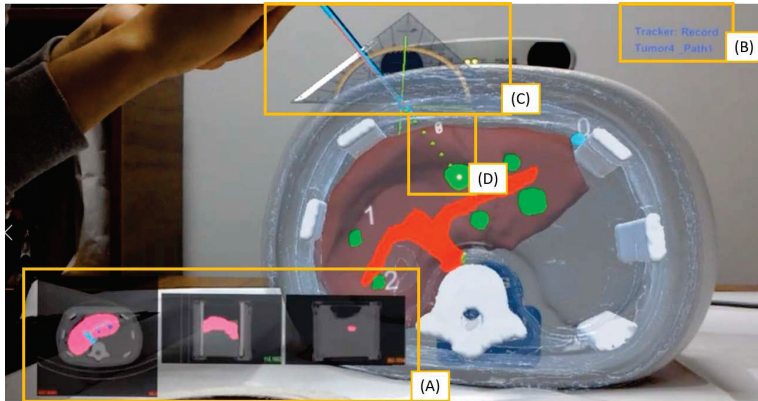


Figure 5.8: This is the illustration of the integration of visual cues in our augmented reality surgical navigation interface. The lower left corner (A) shows the corresponding pre-operative CT-images of the axial, sagittal and coronal plane at the needle tip location. The upper right corner (B) displays the puncture information. The “tracker” label shows the device mode (either “record” mode or “navigation” mode). The path label demonstrates the selected target and puncture path for current insertion. (C) denotes the vision cue for accurate puncture. (D) shows the way point that intuitively provides the surgeon quantitative insertion depth information.

Furthermore, the corresponding pre-operative CT-images of the the axial, sagittal and coronal plane of the needle tip location are accessible at any time during puncture. It can intuitively display either on the corner of the display view or on the corresponding position on the phantom, which can enhance the depth perception at the same time. Besides, our system allows the surgeon hiding any of the visual cues they don’t need at anytime.

The two HoloLens collaboratively work together can not only provide more intuitive navigation information, but also provide different viewing points for surgeon and surgical assistant to precisely perform the puncture operation.

5.6 Experiments

In order to validate the effectiveness of our AR-navigation system and quantitatively evaluate the accuracy and efficiency of the puncture, we conduct several experiments with our navigation modality. In this section, we first

evaluate the puncture path planning and then validate the puncture accuracy. We apply the puncture operation on an abdomen phantom to test our navigation system before performing the animal experiment. Besides, we also validate the tumor prediction accuracy using two different types of cross-validation.

The proposed prototype consists of a CT scanner(Siemens), an optical tracker (Polaris, Northern Digital, Inc.), two OST-HMD devices (Microsoft HoloLens) and a portable computer (Dell Precision 7530 with 12* Xeon E-2176M 12 core 2.70GHz, Intel and Quadro P3200, NVIDIA).

5.6.1 Path planning result evaluation

According to the doctors' suggestions, we set $\theta_{safe} = 10mm$, and take the value of $\theta_{length} = 50mm$ for static abdominal phantom and $\theta_{length} = 35mm$ for beagle dogs.

The second column in Fig. 5.9 shows the needle feasible region of the static abdominal phantom, while the feasible region for a vivo dog under free breathing is shown in Fig. 5.2. In both of the figures, the pixel is marked as red when $R_{feasible} = false$ and marked as blue when when $R_{feasible} = true$. The color saturation corresponds to the value of SDF_{region} . In order to clearly show the structure, the boundary of the tissue structure is colored in yellow and the region outside the patient model is colored in black.

The illustration of the path planning result for abdomen phantom are shown in the Fig. 5.9, from which we can see that the angle difference from our constraint-based optimal path and the path sketched by doctors are quite close to each other. Furthermore, the result also shows that our planned path is more perpendicular to the phantom border, which can reduce the puncture difficulty. Besides, our path is shorter than the ground truth, which can reduce the damage to the patients. Numerical comparison is shown in the Tab. 5.1. The illustration of the path planning result of beagle dog is shown in Fig. 5.2. The puncture along the pre-planned path for phantom tumor insertion are shown in Fig. 5.10.

5.6.2 System Calibration

The calibration process using a coarse-to-fine process aligning the virtual scenario perfectly onto the real scenario. Before calibration, the virtual model is in correct relative position but far away from their corresponding utility in real world. A coarse transformation can be calculated by using the configuration needle tip picking up the points in corresponding real and virtual environment. Then we apply delicate adjust the registration until the virtual information precisely aligned with the real scene. After calibration, the virtual information and the practical real world scenario are acceptable aligned, like shown in Fig. 5.8.

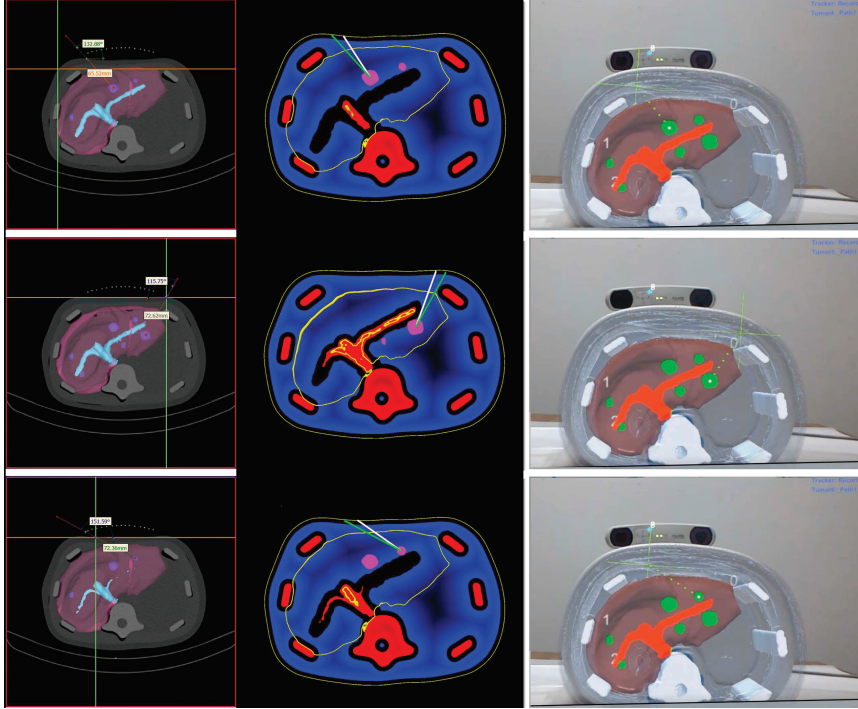


Figure 5.9: Path planning result for static multi-targets abdominal phantom. 1-a to 3-a: the path in the 3d reconstruction model aligned on the CT-images. 1-b to 3-b: the pre-planned puncture path for the liver tumor in the abdomen phantom with method Sec. 5.3. Magenta: Tumor. Green: Puncture path sketched by doctors. White: Our optimal puncture path. 1-c to 3-c: visualization of planned puncture path effect under AR.

Table 5.1: Path planning result compared with ground truth

Nr	(A)	(B)	(C)
P_T	(-15.9, -152.8, -947.5)	(35.9,-138.9,-940.2)	(19.7, -164.9, -945.9)
P_{In} (GT)	(-60.0, -201.2, -947.0)	(70.5, -201.5, -940.0)	(-45.3, -199.5, -946.0)
P_{In} (Ours)	(-47.0, -200.6, -947.5)	(59.5,-203.7,-940.2)	(-30.3, -199.9, -945.9)
$Length_{GT}$	65.5mm	71.5mm	73.6mm
$Length_{Ours}$	57.0mm	69.0mm	61.0mm

Note: The puncture path planning result for three different tumor position: (A), (B) and (C). $P_{In}(GT)$ is the ground truth needle insert position that pre-planned by doctors and $P_{In}(Ours)$ is the insert position of our algorithm. $Length_{GT}$ and $Length_{Ours}$ is the length of the corresponding puncture path.

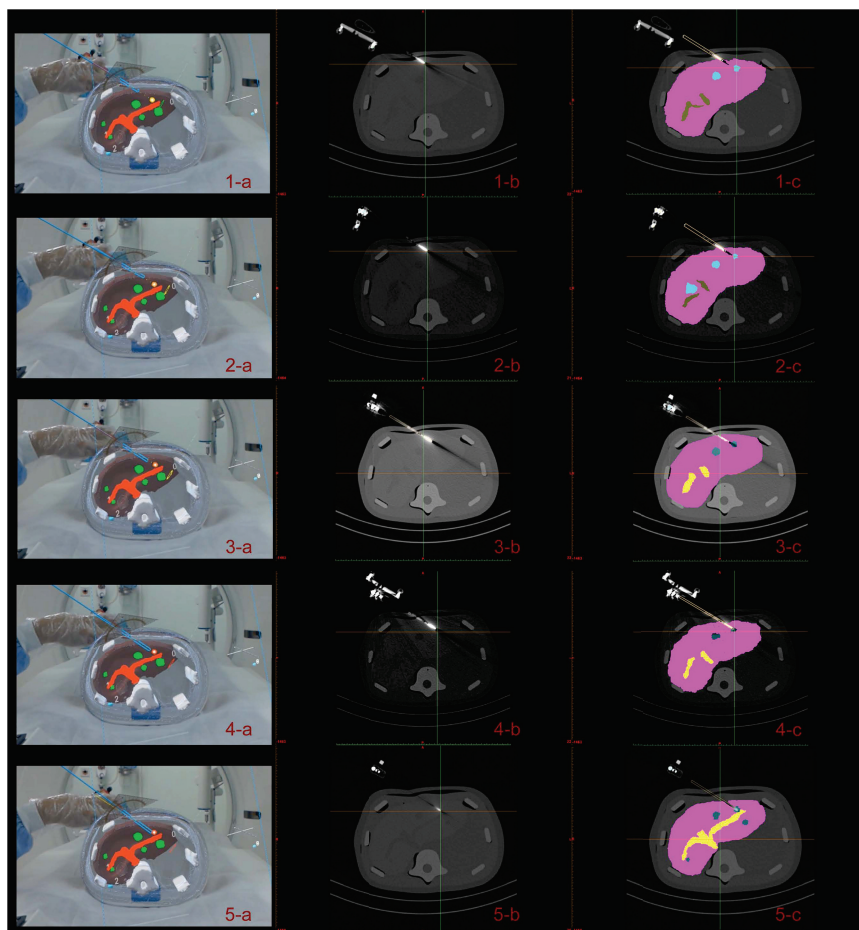


Figure 5.10: The puncture result of static phantom under our augmented virtual reality navigation system. Row 1-5 represent the state when needle stuck one-way-point deeper into the phantom. 1-a to 5-a: The augmented reality navigation of surgical procedure. 1-b to 5-b: The CT scan of the puncture result in the axial plane. 1-c to 5-c: The semantic segmentation of the result overlaid onto the corresponding CT-scanned images, in which the pink denotes for liver, yellow denotes vessels in liver, green denotes the artificial tumor in liver.

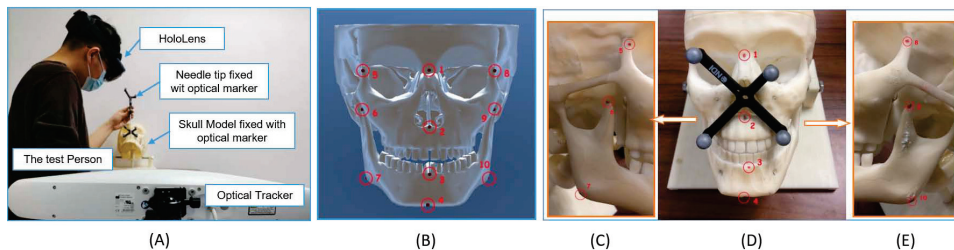


Figure 5.11: (A) The scenario for calibration accuracy test. (B) The virtual 3d model that shown on HoloLens. (C) to (E) The real model for experiment. The red circle marked the locator used for evaluate the calibration result.

In this section, we validate the calibration accuracy of our AR-guided navigation system with the 3D printed skull as experimental object. In preparation step, we label $n = 10$ landmarks L_1, L_2, \dots, L_n on the skull model and label the corresponding landmarks L'_1, L'_2, \dots, L'_n on the virtual model.

Fig. 5.11 shows the experiment scenario of the calibration validation. In the experiment, we first put the skull model inside the tracking region of the optical tracking system and then apply the registration method that described in Sec. 4.1 for virtual-real alignment. In order to validate the alignment, we asked the test person wearing the HoloLens and holding a calibrated needle fixed with optical marker to point the landmarks L_i on skull model and landmarks L'_i on the virtual model respectively with the needle tip. When the test person clicked on the landmarks with the needle tip, we recorded the position of the landmarks P_L and P'_L via the NDI optical tracking system. Thus, the quality of the calibration result is measured with the distance between the virtual and real landmarks. A comparison of calibration result between our method and the method use ARToolKit in [Qian et al., 2018] are listed in Tab. 5.2. The result shows that our method have a average error of $1.68mm$, which is much more accurate than $4.37mm$ with method in [Qian et al., 2018].

5.6.3 Tumor Prediction Validation

In order to evaluate our tumor position prediction method in Sec. 5.4.2, we performed two different validation methods. We perform the k-fold cross-validation for evaluating the accuracy of tumor position prediction under the respiratory motion. To compare the prediction accuracy on different data set, we use the leave-one-out cross-validation method.

Ground Truth Data

To validate the correctness of our prediction, we prepared ground truth data by continuously collect raw medical data with 4D-CT of the same dog. Here

Table 5.2: Registration error comparison

Marker	O_{Our}	O_{ARTK}	E_{Our}	E_{ARTK}
(1)	(-0.5, 0.7, -1.2)	(1.1, -0.9, 4.6)	1.48	4.81
(2)	(-0.3, 0.0, -1.4)	(1.8, -1.7, 3.9)	1.43	4.62
(3)	(-0.8, 0.1, -0.9)	(0.8, -1.1, 2.3)	1.21	2.67
(4)	(1.1, 0.7, -0.8)	(2.3, -1.7, 1.9)	1.53	3.43
(5)	(-1.2, 0.6, -1.9)	(1.7, -1.8, 3.3)	2.33	4.13
(6)	(-1.4, 1.1, -0.7)	(1.2, -1.3, 3.0)	1.91	3.48
(7)	(-1.1, 0.8, -3.0)	(0.9, -1.6, 1.7)	3.29	2.50
(8)	(-0.2, 0.8, -0.4)	(1.7, -2.1, 6.4)	0.92	6.95
(9)	(-0.6, 0.5, -0.5)	(2.2, -1.8, 5.6)	0.93	6.28
(10)	(-0.8, 1.4, -0.7)	(2.4, -2.0, 3.7)	1.76	4.84
AVG	(-0.58,0.67,-1.15)	(1.61,-1.60,3.64)	1.68	4.37

Note: O_{Our} is the offset with our registration method and O_{ARTK} is the registration offset use the ARTToolKit described in [Qian et al., 2018]. E_{Our} and E_{ARTK} are the error distance of landmarks using both method. AVG is the average accuracy of both method. Result shows our calibration method has an average error with $1.68mm$ while the method in [Qian et al., 2018], has registration error of $4.37mm$.

we obtained the ground truth data on two different days and name them *day1* and *day2* respectively. Then we process the data with Sec. 5.4.2 to get the position of the external markers and the corresponding internal tumor position at the same time. The data is separated in two parts, one is the training set to construct the motion model and the other one is validation set to evaluate the prediction result.

Accuracy of the prediction under respiratory motion

The tumor position we predict is based on the respiratory motion modeled in Sec. 5.4.2. The k-fold cross-validation is used to evaluate our predicted accuracy of tumor position under respiratory motion. Here we choose $k = 5$ for this evaluation. The ground truth data set *day1* is divided evenly into k part and then take one of them as the validation set and the rest $k - 1$ parts of them as training set.

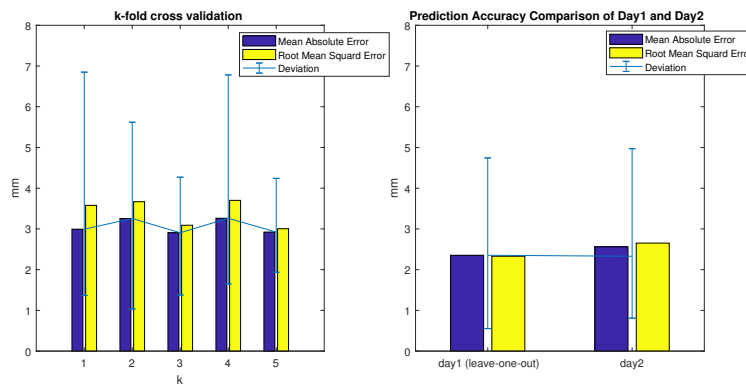


Figure 5.12: Left: The mean absolute error (MAE) of the prediction result and the deviation of the MAE for day1 with k-fold cross-validation. Right: The mean absolute error (MAE) of the prediction result and the deviation of the MAE for two different days with leave-one-out cross-validation.

For each sample in the validation set, we calculate the tumor position from the external skin markers' position with the method in Sec. 5.4.2. Then, we measure the distance between the predicted tumor position and the ground truth. We evaluate the statistical index of prediction for the k validation set. Fig. 5.12 illustrate that the predicted tumor position under respiratory motion can achieve an average error smaller than 3.5mm.

Pre- and intra-operative prediction validation

In order to compare the tumor prediction accuracy between the pre-operative and intra-operative stage, we performed the leave-one-out cross-validation on the data set *day1* and utilize the same model to predict the

tumor position in data set *day2*. The MAE and its deviation of the two data sets are shown in the Fig. 5.12, from which we can see that there is no significant difference. Thus, the internal-external correlation model trained with pre-operative data is feasible to be used for intra-operative tumor position prediction.

5.6.4 System Communication

In our system, we perform the computation of the navigation information processing for the respiratory liver tumor puncture on PC. Then, the system transfers the navigation information to HoloLens, which leads to the system delay. In this regards, our method can make good use of the computational power beyond the commercial HMDs. In order to validate whether our system fulfills the real-time requirement, we performs the following experiment to test the frame rate the system delay of our system.

We have tested the frame rate of OST-HMD by recording the system time stamp. The result shows that the average frame rate of HoloLens2 is $15.60fps$ in Tab. 5.3. With the same experiment, we get the frame rate of HoloLens is $15.50fps$. As human eyes consider the picture update over $12fps$ as continuous video [Read and Meyer, 2000], our method can fulfill the real-time requirement.

In order to obtain the system delay, we first record the the system time of the computer and HoloLens at the same time to synchronize this two devices. When the computer sends data to HoloLens, we marked down the computer's system time that sends out the data and the HoloLens' system time that receives the data. According to this experiment, the delay of our system is $165ms$ on average using HoloLens2. With the same experiment, we get the system delay of HoloLens is $174ms$. Research shows that, the minimum delay that surgeons can recognize is $250ms$ [Avgousti et al., 2016]. Thus, our system delay will have no influence on clinician's operation.

5.6.5 Puncture Experiment

We validate our system on both static phantom and vivo dog. In our puncture operation, an experienced surgeon is invited to insert the tumor in the phantom.

Experimental Material

For puncture validation on static phantom, the surgeon first performs puncture on the triple modality 3D abdominal phantom (Model 057A, Computerized Imaging Reference Systems, Inc.) as the experimental object. It is a plastic model for medical education usage including artificial liver, vessels and tumors. In addition, the anatomical structures of the phantom can be identified by 3D MR images.

Table 5.3: Data transfer delay from PC to HoloLens2 and frame rate of HoloLens2

cis	T_{PC_sys}	T_{HL_sys}	T_{HL_syn}	$Delay(s)$	$Invl(s)$	$Fr(fps)$
(1)	34:29.414	34:04.465	34:29.595	0.181	-	-
(2)	34:35.988	34:11.037	34:36.167	0.179	6.572	15.22
(3)	34:42.651	34:17.711	34:42.841	0.190	6.674	14.98
(4)	34:49.163	34:24.220	34:49.350	0.187	6.509	15.36
(5)	34:55.427	34:30.479	34:55.609	0.182	6.259	15.98
(6)	35:01.909	34:36.973	35:02.103	0.184	6.494	15.40
(7)	35:08.046	34:43.102	35:08.232	0.186	6.129	16.31
(8)	35:14.228	34:49.291	35:14.421	0.193	6.189	16.16
(9)	35:20.753	34:55.806	35:20.936	0.183	6.515	15.35
(10)	35:27.128	35:02.177	35:27.307	0.179	6.371	15.70
AVG				0.165		15.60

Note: T_{PC_sys} and T_{HL_sys} are original system time that PC sends data and HoloLens2 receives data. T_{HL_syn} is the time on HoloLens2 synchronized with PC system time. $Delay$ is the system delay induced by data transfer. $Invl$ is the time interval during 100 times of data received. Fr is the frame rate of HoloLens2. AVG is the average system delay and frame rate after the 10 times records.

For dynamic puncture validation, we employ the experiment animal: beagle dog, female, 40 months, 11 kg. Percutaneous liver puncture of experimental animal was performed after general anesthesia.

The artificial tumor model is built by implanting iodine oil into animal liver. The beagle dog is scanned with CT to determine the appropriate position of tumor implantation and the position of optical markers around liver region. Then, the surgeon choose the needle insertion path (7th subcostal), insertion angle (perpendicular to the skin) and insertion depth (8cm) from the puncture point on the skin to inject the prepared iodine oil (2ml) into the liver.

Needle insertion

In the augmented reality navigation modality, we add the NDI Polaris to track all the utilities in surgical scenario. Besides, the surgeon wears one of the HoloLens to locate the moving tumor while the assistant wears the other HoloLens to monitor the overall process and record the video.

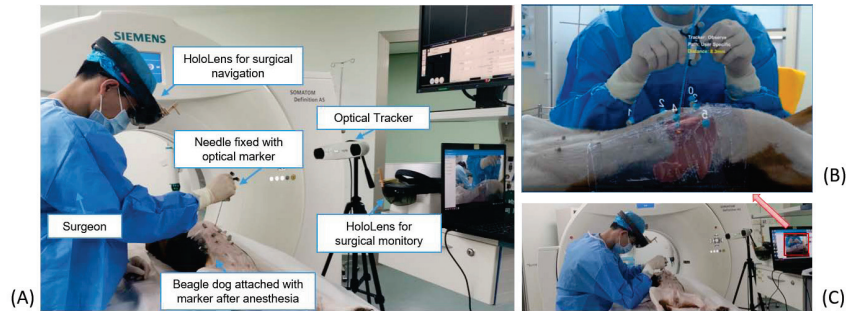


Figure 5.13: The surgeon performed AR-guided needle insertion on beagle dog. (A): The practical scenario of our augmented virtual reality tumor puncture surgery. (B): The virtual guidance information that real-time monitoring from the collaborative HoloLens. (C): Surgeon performs puncture.

We design the test scene with phantom and ablation needle shown in Fig. 5.8, while the operation process on vivo beagle dog is shown in the Fig. 5.13. The optimal path for percutaneous puncture is planned with the method described in Sec. 5.3. For the vivo dog tumor puncture, the position of the tumor position is real-timely updated during the operation, so that the needle puncture path is shown dynamically in the HoloLens.

Puncture precision

To validate the effectiveness of our navigation system under dynamic conditions, an experienced surgeon was invited to adopt both traditional CT-guided and augmented reality guided modalities to insert the ablation needle

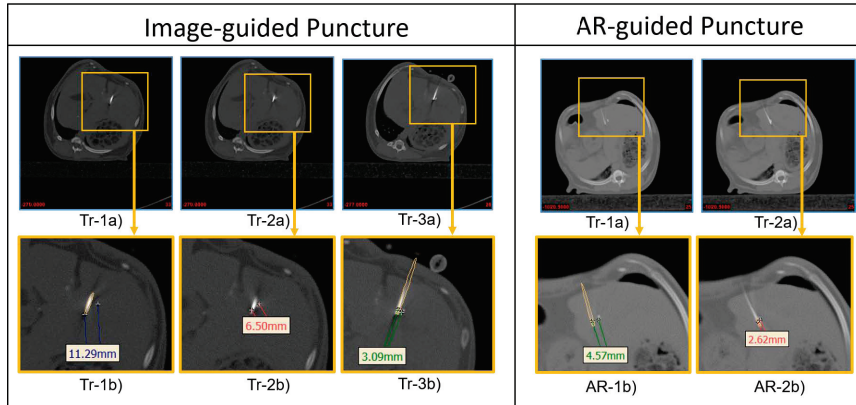


Figure 5.14: The axial plane of the needle insertion result. The bottom row shows the zoom-in of the tumor puncture area. The yellow pole marks the pose of insertion needle. Tr-1) to Tr3): traditional image-guided puncture with twice needle adjustment; AR-1) to AR-2): AR-guided puncture with once needle adjustment.

into the respiratory dog liver tumor. According to suggestions from the surgeon, only punctures no further than $3.50mm$ away from the tumor center can be regarded as an “accurate” puncture, needle adjustment is allowed to place the accurate puncture.

The percutaneous puncture results of traditional CT-guided modality and our augmented reality modality can be seen in Fig. 5.14, which illustrates that compared with traditional navigation modality, our method allows surgeons intuitively targeting the lesion from different insert angles with high accuracy, while it can also reduce the number of needle adjustments.

5.7 Discussion

Our prototype modeled the ablation needle as a rigid needle, which is not applicable in practical ablation puncture. In this regard, the surgeons in our experiment are asked to hold the needle in the proper way to make sure the puncture direction is always parallel with the direction of needle body, so that the effect of the deformation can be neglected. However, the ablation needle is a flexible body and will deform during the puncturing, so that we will further develop the hidden needle behavior prediction method.

Our prototype only considers the small tumor (diameter $< 3cm$) which can be totally ablated with a single ablation needle. As the ablation needle can only damage the tumor and tissue inside a specific region, for the larger tumors, the multi-needle puncture should be considered.

The dynamic tumor position in our prototype is predicted by the correlation model of external skin markers and internal respiratory tumor. How-

ever, under the practical surgical scenario, the dynamic motion of tumor and organ position are affected by the needle-tissue interaction as well. Therefore, the modeling of the needle-tissue interaction is also an important topic for our following research.

5.8 Conclusion and Future Work

In this paper, we present an augmented virtual reality guidance modality to improve the precision of liver tumor punctures by patient-specific surgical planning and providing the intuitive interface for puncture navigation. Our novel guidance modality can be divided into two major steps: a constraint-based puncture path planning method via 3D signed distance field fusion is proposed for automatically planning the optimal puncture trajectory from the quantitative perspective, which can greatly reduce the doctors' experience-dependence and improve the precision. A collaborative holographic augmented reality interface is designed for intra-operative navigation, which can not only superimpose the dynamic internal behavior and planned trajectory information onto surgical scenarios, but also integrate some visual cues to enhance the depth perception. The result of the pre-operative validation and the the puncture result both under static and dynamic conditions are evaluated via phantom and animal experiment respectively. The result shows our augmented reality based surgical navigation modality can achieve higher efficiency and accuracy than the traditional image-based surgical navigation modality.

Considering that our current correlation model can only predict the tumor moving along with the surface markers, which can't provide the deformation of other key structures in target region, such as vessels. Thus, our immediate plan is to achieve the non-rigid registration of such key structures in order to provide more comprehensive navigation information for the surgeons. Besides, we will be also interested in investigating the modeling method of flexible needle during puncture. Furthermore, we will extend this promising guidance modality to other challenging surgical scenarios, such as deep brain stimulation, where electrode needs to be placed in a high-precision target region.

Errata

The sentence in **5.1** on page **88** is updated as:

Also the deformation of the needle and target region are ~~took~~taken into consideration in the recent work [Hamzé et al., 2016].

The Equation **5.9** on page **99** should be updated as:

$$\left\{ \begin{array}{l} \dots \\ p(t_i) = a_i * t_i^2 + b_i * t_i + c_i \\ p(t_i) = a_{i+1} * t_i^2 + b_{i+1} * t_i + c_{i+1} \\ p(t_{i+1}) = a_{i+1} * t_{i+1}^2 + b_{i+1} * t_{i+1} + c_{i+1} \\ p(t_{i+1}) = a_{i+2} * t_{i+1}^2 + b_{i+2} * t_{i+1} + c_{i+1} \\ \dots \\ 2 * a_i * t_i + b_i = 2 * a_{i+1} * t_i + b_{i+1} \\ 2 * a_{i+1} * t_{i+1} + b_{i+1} = 2 * a_{i+2} * t_{i+1} + b_{i+2} \\ \dots \end{array} \right.$$

Part V

Discussion

Discussion

The therapy for tumor treatment nowadays considers not only curing cancer but also causing less damage to the healthy tissue. With the development of medical techniques, early diagnosis of cancer also gives doctors and patients more options for tumor treatment. The minimal invasive thermal ablation therapy like RFA or MWA become widely accepted. This thesis provides the solution for solving the liver tumor treatment with the computer-assisted method in a quantitative and intuitive way. In particular, the content in the former chapters covers thermal ablation planning, the dynamic surgical target estimation, and the mixed reality percutaneous tumor puncture navigation. In this final chapter, we summarize the contribution of our novel surgical planning and guiding system for liver tumor treatment, discuss the limitation of the current method and give instructions for future work.

6.1 Conclusion

With this dissertation, we had addressed major challenges of computer-assisted thermal ablation for hepatic tumor treatment to allow a minimally invasive surgery. This thesis provides a solution via automatic pre-operative surgical planning based on a digitized model incorporating a series of medical constraints extracted from the specialists' consensus, intra-operative calibration of model dynamics during the breathing process to accurately align the virtual representation with the real-world scenario, and augmented reality navigation collaborated with a holographic interface which can effectively assist surgeons in fast and accurately locating the target step-by-step.

In the context of pre-operative surgical planning, we presented a computer-assisted thermal ablation planning method. This method involves the multi-needle configuration for large tumors, the ablation center distribution, and the insertion trajectory optimization based on the medical and geometry constraints. The comparison with the state-of-the-art method shows that our method can give proper ablation suggestions without dependence on the pre-given potential needle paths. The experimental results also showed that our method allows completely ablating the tumor region with smaller healthy tissue damage than the manual planning sketched by the experimental clinical puncture paths. And it also offered great flexibility for adjusting empirical parameters for each step.

For considering the surgical target dynamics during the breathing process within the intra-operative needle puncture process, we constructed a correlation model between the surface marker and internal tumor movement, involving the motion compensation of the liver in the intra-operative process. In this way, the intra-operative dynamic movement of the surgical target can be estimated via the observed displacement of the external skin markers. So that surgeons are able to observe the real-time target movement and perform the tumor puncture with higher accuracy and efficiency. The in-vivo tumor puncture experiment shows that navigation including dynamic information can improve the puncture efficiency and accuracy.

In order to navigate the needle towards the correct target intuitive and quantitatively, this mixed reality liver tumor puncture navigation system superimposes the anatomical dynamics together with the 3D preoperative surgical planning information on the intra-operative real-world scenario. The performance of our tumor puncture navigation modality has been validated on both a static abdominal phantom and in-vivo animals with the artificial lesion. Experimental results demonstrated that surgeons with holographic augmented reality information can locate the needle to lesion more easily, efficiently, and accurately than using the traditional 2D CT images guided modality.

In summary, our proposed computer-assisted thermal ablation planning and navigation system can greatly reduce the doctors' experience-dependence and improve the precision and efficiency of the treatment. This gives the potential to apply this technique to other surgical navigation tasks.

6.2 Limitations and Future Work

This work presented in this thesis can be continued and extended for further applications in surgical or other medical scenarios. From the former work in this proposed liver tumor treatment planning and navigation system, some insights may instruct future research work:

- A proper interpretation of the medical experience to arithmetic constraints can make the computer-assisted surgical planning process smart and applicable. An example in the thermal ablation planning is, the needle tip configuration needs to follow the expert consensus that neither too close nor too far from each other, thus the logistic function (Function 2.9) can nicely interpret this relevance, thus can help to include this into the algorithm.
- The statistic motion model can use for reconstructing the organ displacement and deformation together with the statistic shape model. In the medical scene, the motion of organs like lungs and liver are highly dependent on the respiration of the patient. Thus, a correla-

tion model between the organ movement and the respiration state can help to estimate the organ behavior. As the respiration state can be extracted with a non-invasive approach like an optical tracking system, therefore the motion of organs can be estimated from it together with the pre-constructed correlation model.

- The proposed prototype in this thesis shows a strategy i.e. computes the time-consuming pre-operative planning and the intra-operative dynamic information on PC and transfers only the result to OST-HMDs for rendering via the network connection, which can extend computational power for the out-off-shelf OST-HMDs. When applying the mixed reality surgical navigation modality to different surgical scenarios, researchers can construct the scenes and process all the computations on a high-performance computer which can involve as much precise and detailed medical information as they need, deploy the pre-constructed surgical scene models for navigation on the head-mounted devices at the pre-operative stage, and transfer only the structured navigation data via the network connection during an intra-operation stage.

In this section, we talk about the potential direction for extending the current work:

6.2.1 Soft tissue prediction for the respiration movement

So far, our current correlation model can only predict the tumor and liver movement along with the surface markers, however, does not take into account the deformation of other key structures within the target region such as vessels. In order to provide more comprehensive navigation information for the surgeons, our immediate plan is to achieve the non-rigid registration of such key structures.

Considering the deformation of the liver structure that is influenced by respiration, we can involve a two-step method: first compute the liver surface deformation with the optical skin marker and then generate the liver internal structure with the liver surface deformation. By applying the generalized moving least square (GMLS) algorithm [Courtecuisse et al., 2014], live-updated marker positions on the skin surface can be used for predicting the liver surface deformation. Inspired by [Pfeiffer et al., 2020] and [Ma et al., 2018], an efficient Shuffle-UNet3D is employed to match the reference pre-operative liver volume to the intra-operative partial liver surface predicted by regularization GMLS (RGMLS) to fulfill the real-time requirement of intra-operative navigation. In this way, the intra-operative liver and vessel deformation can be predicted, and therefore gives the surgeon more navigation information.

6.2.2 Flexible needle behavior prediction

Our prototype modeled the ablation needle as a rigid needle, which in practical ablation puncture is not applicable. In this regard, in our experiment, the surgeons are asked to hold the needle in the proper way to make sure the puncture direction is always parallel with the direction of the needle body so that the effect of the deformation can be neglected.

However, under the practical surgical scenario, the dynamic motion of the tumor and organ position is affected by the needle-tissue interaction as well. Therefore, the modeling of the needle-tissue interaction is also an important topic for our following research. It will be also interesting in investigating the modeling of flexible needles during puncture as well as the needle behavior prediction method.

6.2.3 Thermal ablation planning for versatile needle configuration

So far, our thermal ablation planning method only considered the configuration of multiple single-tip-electrodes that perform the thermal ablation simultaneously. Further strategies for thermal ablation surgery include the sequential ablation based on single-tip-electrodes or the ablation with cluster electrodes that were not evolved in the current work. While we did not focus on these strategies, our approach can also be adapted to the sequential ablation by adjusting the remaining treatment zone and the current needle position. In future work, with an increasing number of available patient data, we will explore the selection of optimal parameter configurations for different cases.

6.2.4 Surgical planning in other surgical scenarios

In neurosurgery, electrodes implanted into brains are applied for treating some specific type of disease. We can extend this promising guidance modality and surgical planning method to more challenging surgical scenarios, such as deep brain stimulation (DBS) for treating movement disorders associated with Parkinson's disease (PD) or localizing the seizure focus with Stereoelectroencephalography (SEEG) in epilepsy treatment, where electrodes need to be placed in a high-precision target region [The Johns Hopkins University, 2022a, UPMC Presbyterian, 2022].

Similar to tumor puncture in thermal ablation, neurosurgery treatment also needs trajectory planning for inserting electrodes. With the anatomical and brain atlas annotation, researchers can first determine the feasible region or safety area for insertion of electrodes and then optimize the trajectory for electrodes' insertion based on the medical constraints extracted from the specialist consensus.

Hilfsmittel

The medical data and the experiment animal used in this thesis are provided by the co-operation hospitals of Shenzhen Institute of Advanced Technology, Chinese Academy of Sciences. They are: Shenzhen People's Hospital, Shenzhen Second People's Hospital and The First Affiliated Hospital, Sun Yat-sen University. All the medical experiment was approved by the local ethics committee.

Bibliography

- [Ahmed et al., 2011] Ahmed, M., Brace, C. L., Lee Jr, F. T., and Goldberg, S. N. (2011). Principles of and advances in percutaneous ablation. *Radiology*, 258(2):351–369.
- [Al Janabi et al., 2020] Al Janabi, H. F., Aydin, A., Palaneer, S., Macchione, N., Al-Jabir, A., Khan, M. S., Dasgupta, P., and Ahmed, K. (2020). Effectiveness of the hololens mixed-reality headset in minimally invasive surgery: a simulation-based feasibility study. *Surgical Endoscopy*, 34(3):1143–1149.
- [Altrogge et al., 2006] Altrogge, I., Kröger, T., Preusser, T., Büskens, C., Schmidt, D., Weihusen, A., and otto Peitgen, H. (2006). Towards optimization of probe placement for radio-frequency ablation. In *In MICCAI 2006, volume 4190 of LNCS*, pages 486–493.
- [Amalou and Wood, 2012] Amalou, H. and Wood, B. J. (2012). Electromagnetic tracking navigation to guide radiofrequency ablation (rfa) of a lung tumor. *Journal of bronchology & interventional pulmonology*, 19(4):323.
- [American Cancer Society, Inc, 2022] American Cancer Society, Inc (2022). Ablation for liver cancer. <https://www.cancer.org/cancer/liver-cancer/treating/tumor-ablation.html>. [Online; accessed 06-April-2022].
- [Andersen et al., 2016] Andersen, D., Popescu, V., Cabrera, M. E., Shanghavi, A., Gomez, G., Marley, S., Mullis, B., and Wachs, J. (2016). Virtual annotations of the surgical field through an augmented reality transparent display. *The Visual Computer*, 32(11):1481–1498.
- [Avgousti et al., 2016] Avgousti, S., Christoforou, E. G., Panayides, A. S., Voskarides, S., Novales, C., Nouaille, L., Pattichis, C. S., and Vieyres, P. (2016). Medical telerobotic systems: current status and future trends. *Biomedical engineering online*, 15(1):1–44.
- [Baegert et al., 2007a] Baegert, C., Essert, C., Schreck, P., Soler, L., and Gangi, A. (2007a). Trajectory optimization for the planning of percutaneous radiofrequency ablation of hepatic tumors. *Computer aided surgery : official journal of the International Society for Computer Aided Surgery*, 12:82–90.
- [Baegert et al., 2007b] Baegert, C., Villard, C., Schreck, P., and Soler, L. (2007b). Multi-criteria trajectory planning for hepatic radiofrequency ablation. In Ayache, N., Ourselin, S., and Maeder, A., editors, *Medical*

Image Computing and Computer-Assisted Intervention – MICCAI 2007, pages 676–684, Berlin, Heidelberg. Springer Berlin Heidelberg.

- [Bernhardt et al., 2017a] Bernhardt, S., Nicolau, S. A., Soler, L., and Doignon, C. (2017a). The status of augmented reality in laparoscopic surgery as of 2016. *Medical Image Analysis*, 37:66–90.
- [Bernhardt et al., 2017b] Bernhardt, S., Nicolau, S. A., Soler, L., and Doignon, C. (2017b). The status of augmented reality in laparoscopic surgery as of 2016. *Medical Image Analysis*, 37:66.
- [Birlo et al., 2022] Birlo, M., Edwards, P. E., Clarkson, M., and Stoyanov, D. (2022). Utility of optical see-through head mounted displays in augmented reality-assisted surgery: A systematic review. *Medical Image Analysis*, page 102361.
- [Biro et al., 2009] Biro, P., Spahn, D., and Pfammatter, T. (2009). High-frequency jet ventilation for minimizing breathing-related liver motion during percutaneous radiofrequency ablation of multiple hepatic tumours. *British journal of anaesthesia*, 102(5):650–653.
- [Bravo et al., 2001] Bravo, A. A., Sheth, S. G., and Chopra, S. (2001). Liver biopsy. *New England Journal of Medicine*, 344(7):495.
- [Breen and Lencioni, 2015] Breen, D. J. and Lencioni, R. (2015). Image-guided ablation of primary liver and renal tumours. *Nature Reviews Clinical Oncology*, 12(3):175–186.
- [Byrd et al., 2000] Byrd, R. H., Gilbert, J. C., and Nocedal, J. (2000). A trust region method based on interior point techniques for nonlinear programming. *Mathematical programming*, 89(1):149–185.
- [Byrd et al., 1999] Byrd, R. H., Hribar, M. E., and Nocedal, J. (1999). An interior point algorithm for large-scale nonlinear programming. *SIAM Journal on Optimization*, 9(4):877–900.
- [Cai et al., 2016] Cai, K., Yang, R., Chen, H., Ning, H., Ma, A., Zhou, J., Huang, W., and Ou, S. (2016). Simulation and visualization of liver cancer ablation focus in optical surgical navigation. *Journal of medical systems*, 40(1):19.
- [Cazzato et al., 2016] Cazzato, R. L., Garnon, J., Ramamurthy, N., Tsoumakidou, G., Imperiale, A., Namer, I. J., Bachellier, P., Caudrelier, J., Rao, P., Koch, G., et al. (2016). 18f-fdopa pet/ct-guided radiofrequency ablation of liver metastases from neuroendocrine tumours: Technical note on a preliminary experience. *Cardiovascular and interventional radiology*, 39(9):1315–1321.

- [Chan et al., 2021] Chan, H. H., Haerle, S. K., Daly, M. J., Zheng, J., Philp, L., Ferrari, M., Douglas, C. M., and Irish, J. C. (2021). An integrated augmented reality surgical navigation platform using multi-modality imaging for guidance. *PloS One*, 16(4):e0250558.
- [Chan and Heng, 2014] Chan, W.-Y. and Heng, P.-A. (2014). Visualization of needle access pathway and a five-dof evaluation. *IEEE journal of biomedical and health informatics*, 18(2):643–653.
- [Chen et al., 2018a] Chen, R., Jiang, T., Lu, F., Wang, K., and Kong, D. (2018a). Semiautomatic radiofrequency ablation planning based on constrained clustering process for hepatic tumors. *IEEE Transactions on Biomedical Engineering*, 65(3):645–657.
- [Chen et al., 2018b] Chen, R., Lu, F., Wu, F., Jiang, T., Xie, L., and Kong, D. (2018b). An analytical solution for temperature distributions in hepatic radiofrequency ablation incorporating the heat-sink effect of large vessels. *Physics in Medicine & Biology*, 63(23):235026.
- [Choi et al., 2001] Choi, H., Loyer, E. M., DuBrow, R. A., Kaur, H., David, C. L., Huang, S., Curley, S., and Charnsangavej, C. (2001). Radiofrequency ablation of liver tumors: assessment of therapeutic response and complications. *Radiographics*, 21(suppl_1):S41–S54.
- [Clasen and Pereira, 2008] Clasen, S. and Pereira, P. L. (2008). Magnetic resonance guidance for radiofrequency ablation of liver tumors. *Journal of Magnetic Resonance Imaging*, 27(2):421–433.
- [Couinaud, 1999] Couinaud, C. (1999). Liver anatomy: portal (and suprahepatic) or biliary segmentation. *Digestive surgery*, 16(6):459–467.
- [Courtecuisse et al., 2014] Courtecuisse, H., Allard, J., Kerfriden, P., Bordas, S. P., Cotin, S., and Duriez, C. (2014). Real-time simulation of contact and cutting of heterogeneous soft-tissues. *Medical image analysis*, 18(2):394–410.
- [Crezee and Legendijk, 1992] Crezee, J. and Legendijk, J. (1992). Temperature uniformity during hyperthermia: the impact of large vessels. *Physics in Medicine & Biology*, 37(6):1321.
- [Crocetti et al., 2016] Crocetti, L., Della Pina, M. C., Cioni, D., and Lencioni, R. (2016). Image-guided ablation of hepatocellular carcinoma. *Interventional Oncology: Principles and Practice of Image-Guided Cancer Therapy*, page 91.
- [De Paolis and De Luca, 2019] De Paolis, L. T. and De Luca, V. (2019). Augmented visualization with depth perception cues to improve the

- surgeon's performance in minimally invasive surgery. *Medical & biological engineering & computing*, 57(5):995–1013.
- [Emery and Sekins, 1982] Emery, A. F. and Sekins, K. M. (1982). The use of heat transfer principles in designing optimal diathermy and cancer treatment modalities. *International Journal of Heat and Mass Transfer*, 25(6):823–834.
- [EXTEND3D GmbH, 2019] EXTEND3D GmbH (2019). Werklicht pro I. <https://www.extend3d.com/de/>. [Online; accessed 28-Feb-2022].
- [Flaherty and Bilchik, 2017] Flaherty, D. C. and Bilchik, A. J. (2017). Radiofrequency ablation of liver tumors. In *Blumgart's Surgery of the Liver, Biliary Tract and Pancreas, 2-Volume Set (Sixth Edition)*, pages 1436–1447. Elsevier.
- [Galati et al., 2020] Galati, R., Simone, M., Barile, G., De Luca, R., Cartanese, C., and Grassi, G. (2020). Experimental setup employed in the operating room based on virtual and mixed reality: analysis of pros and cons in open abdomen surgery. *Journal of Healthcare Engineering*, 2020.
- [Gauß, 1876] Gauß, C. F. (1876). Besprechung des buchs von la seeber: Untersuchungen uber die eigenschaften der positiven ternaren quadratischen formen usw. *Gotttingensche Gelehrte Anzeigen*, 2:188–196.
- [Giering et al., 1995] Giering, K., Lamprecht, I., Minet, O., and Handke, A. (1995). Determination of the specific heat capacity of healthy and tumorous human tissue. *Thermochimica acta*, 251:199–205.
- [Google, 2018] Google (2018). Google measure. <https://www.googlewatchblog.de/2021/06/measure-das-googles-massband/>. [Online; accessed 28-Feb-2022].
- [Google, 2020] Google (2020). Glass. <https://www.google.com/glass/start/>. [Online; accessed 14-January-2020].
- [Grubert et al., 2018] Grubert, J., Itoh, Y., Moser, K., and Swan, J. (2018). A survey of calibration methods for optical see-through head-mounted displays. *IEEE transactions on visualization and computer graphics*, 24(9):2649.
- [Guha et al., 2017a] Guha, D., Alotaibi, N. M., Nguyen, N., Gupta, S., McFaul, C., and Yang, V. X. (2017a). Augmented reality in neurosurgery: A review of current concepts and emerging applications. *Canadian Journal of Neurological Sciences*, 44(3):235–245.
- [Guha et al., 2017b] Guha, D., M. Alotaibi, N., Nguyen, N., Gupta, S., Mcfaul, C., and Yang, V. (2017b). Augmented reality in neurosurgery: A

- review of current concepts and emerging applications. *Canadian Journal of Neurological Sciences / Journal Canadien des Sciences Neurologiques*, 44:1–11.
- [Hamzé et al., 2016] Hamzé, N., Peterlík, I., Cotin, S., and Essert, C. (2016). Preoperative trajectory planning for percutaneous procedures in deformable environments. *Comput. Medical Imaging Graph.*, 47:16–28.
- [Jud et al., 2017] Jud, C., Cattin, P. C., and Preiswerk, F. (2017). Chapter 14 - statistical respiratory models for motion estimation. *Statistical Shape and Deformation Analysis*, pages 379–407.
- [Kazemi and Sullivan, 2014] Kazemi, V. and Sullivan, J. (2014). One millisecond face alignment with an ensemble of regression trees. In *Proceedings of the IEEE conference on computer vision and pattern recognition*, pages 1867–1874.
- [Khan et al., 2006] Khan, M. F., Dogan, S., Maataoui, A., Wesarg, S., Gurrung, J., Ackermann, H., Schiemann, M., Wimmer-Greinecker, G., and Vogl, T. J. (2006). Navigation-based needle puncture of a cadaver using a hybrid tracking navigational system. *Investigative radiology*, 41(10):713–720.
- [Kim et al., 2012] Kim, P. N., Choi, D., Rhim, H., Rha, S. E., Hong, H. P., Lee, J., Choi, J.-I., Kim, J. W., Seo, J. W., Lee, E. J., et al. (2012). Planning ultrasound for percutaneous radiofrequency ablation to treat small (≤ 3 cm) hepatocellular carcinomas detected on computed tomography or magnetic resonance imaging: a multicenter prospective study to assess factors affecting ultrasound visibility. *Journal of Vascular and Interventional Radiology*, 23(5):627–634.
- [Knavel and Brace, 2013] Knavel, E. M. and Brace, C. L. (2013). Tumor ablation: common modalities and general practices. *Techniques in vascular and interventional radiology*, 16(4):192–200.
- [Lee et al., 2010] Lee, M. W., Kim, Y. J., Park, H. S., Yu, N. C., Jung, S. I., Ko, S. Y., and Jeon, H. J. (2010). Targeted sonography for small hepatocellular carcinoma discovered by ct or mri: factors affecting sonographic detection. *American Journal of Roentgenology*, 194(5):W396–W400.
- [Li et al., 2020a] Li, G., Dong, J., Wang, J., Cao, D., Zhang, X., Cao, Z., and Lu, G. (2020a). The clinical application value of mixed-reality-assisted surgical navigation for laparoscopic nephrectomy. *Cancer Medicine*, 9(15):5480–5489.
- [Li et al., 2020b] Li, J., Xu, Y., Shen, N., Feng, L., Ran, Z., and Deng, Z. (2020b). A practical pretreatment planning method of multiple punctur-

- ing for thermal ablation surgery. *Biocybernetics and Biomedical Engineering*, 40(4):1469–1485.
- [Li et al., 2021a] Li, R., Shi, Y., Huang, L., Zhaung, B., Weinmann, M., Klein, R., and Heng, P.-A. (2021a). Versatile multi-constrained planning for thermal ablation of large liver tumors. *Computerized Medical Imaging and Graphics*.
- [Li et al., 2019a] Li, R., Si, W., Liao, X., Wang, Q., Klein, R., and Heng, P.-A. (2019a). Mixed reality based respiratory liver tumor puncture navigation. *Computational Visual Media*, 5(4):363–374.
- [Li et al., 2021b] Li, R., Tong, Y., Yang, T., Guo, J., Si, W., Zhang, Y., Klein, R., and Heng, P.-A. (2021b). Towards quantitative and intuitive percutaneous tumor puncture via augmented virtual reality. *Computerized Medical Imaging and Graphics*, 90:101905.
- [Li et al., 2019b] Li, R., Yang, T., Si, W., Liao, X., Wang, Q., Klein, R., and Heng, P.-A. (2019b). Augmented reality guided respiratory liver tumors punctures: A preliminary feasibility study. In *SIGGRAPH Asia 2019 Technical Briefs*, pages 114–117.
- [Liang et al., 2019a] Liang, L., Cool, D., Kakani, N., Wang, G., Ding, H., and Fenster, A. (2019a). Automatic radiofrequency ablation planning for liver tumors with multiple constraints based on set covering. *IEEE transactions on medical imaging*, 39(5):1459–1471.
- [Liang et al., 2019b] Liang, L., Cool, D., Kakani, N., Wang, G., Ding, H., and Fenster, A. (2019b). Development of a multi-objective optimized planning method for microwave liver tumor ablation. In *International Conference on Medical Image Computing and Computer-Assisted Intervention*, pages 110–118. Springer.
- [Liang et al., 2020] Liang, L., Cool, D., Kakani, N., Wang, G., Ding, H., and Fenster, A. (2020). Multiple objective planning for thermal ablation of liver tumors. *International Journal of Computer Assisted Radiology and Surgery*, 15(11):1775–1786.
- [Liang et al., 2009] Liang, P., Wang, Y., Yu, X., and Dong, B. (2009). Malignant liver tumors: treatment with percutaneous microwave ablation-complications among cohort of 1136 patients. *Radiology*, 251(3):933–940.
- [Lin et al., 2018] Lin, M. A., Siu, A. F., Bae, J. H., Cutkosky, M. R., and Daniel, B. L. (2018). Holoneedle: augmented reality guidance system for needle placement investigating the advantages of three-dimensional needle shape reconstruction. *IEEE Robotics and Automation Letters*, 3(4):4156–4162.

- [Liu et al., 2018] Liu, H., Auvinet, E., Giles, J., and y Baena, F. R. (2018). Augmented reality based navigation for computer assisted hip resurfacing: a proof of concept study. *Annals of biomedical engineering*, 46(10):1595–1605.
- [Livraghi et al., 2011] Livraghi, T., Mäkisalo, H., and Line, P.-D. (2011). Treatment options in hepatocellular carcinoma today. *Scandinavian Journal of Surgery*, 100(1):22–29.
- [Livraghi et al., 2003] Livraghi, T., Solbiati, L., Meloni, M. F., Gazelle, G. S., Halpern, E. F., and Goldberg, S. N. (2003). Treatment of focal liver tumors with percutaneous radio-frequency ablation: complications encountered in a multicenter study. *Radiology*, 226(2):441–451.
- [Ma et al., 2018] Ma, N., Zhang, X., Zheng, H.-T., and Sun, J. (2018). Shufflenet v2: Practical guidelines for efficient cnn architecture design. In *Proceedings of the European conference on computer vision (ECCV)*, pages 116–131.
- [Magic Leap, 2018] Magic Leap, I. (2018). magic-leap-1. <https://www.magicleap.com/en-us/magic-leap-1>.
- [Mahmood et al., 2018] Mahmood, F., Mahmood, E., Dorfman, R. G., Mitchell, J., Mahmood, F.-U., Jones, S. B., and Matyal, R. (2018). Augmented reality and ultrasound education: initial experience. *Journal of cardiothoracic and vascular anesthesia*, 32(3):1363–1367.
- [Mauri et al., 2015] Mauri, G., Cova, L., De Beni, S., Ierace, T., Tondolo, T., Cerri, A., Goldberg, S. N., and Solbiati, L. (2015). Real-time us-ct/mri image fusion for guidance of thermal ablation of liver tumors undetectable with us: results in 295 cases. *Cardiovascular and interventional radiology*, 38(1):143–151.
- [Medtronic, 2020] Medtronic (2020). COOL-TIPTM RF ABLATION SYSTEM ELECTRODES AND ACCESSORIES. <https://www.medtronic.com/covidien/en-us/products/ablation-systems/cool-tip-rf-ablation-electrodes.html>. [Online; accessed 18-December-2020].
- [Microsoft, 2016] Microsoft (2016). Mixed Reality documentation. <https://docs.microsoft.com/en-us/windows/mixed-reality/>. [Online; accessed 09-August-2019].
- [Microsoft, 2019] Microsoft (2019). Hololens2. <https://www.microsoft.com/en-us/hololens/hardware>. [Online; accessed 01-Jan-2022].

- [Minami and Kudo, 2013] Minami, Y. and Kudo, M. (2013). M (2013) radiofrequency ablation of liver metastases from colorectal cancer: a literature review. *gut liver*: 1-6.
- [Niantic, 2016] Niantic, I. (2016). Pokemon go. <https://pokemongolive.com/#news>. [Online; accessed 28-Feb-2022].
- [Nicolau et al., 2007] Nicolau, S., Pennec, X., Soler, L., and Ayache, N. (2007). Clinical evaluation of a respiratory gated guidance system for liver punctures. In *International Conference on Medical Image Computing and Computer-Assisted Intervention*, pages 77–85. Springer.
- [Novarad Healthcare Imaging, 2019] Novarad Healthcare Imaging (2019). OpenSight augmented reality for surgical applications. <https://www.opensight.health/>. [Online; accessed 14-January-2020].
- [Pelanis et al., 2020] Pelanis, E., Kumar, R. P., Aghayan, D. L., Palomar, R., Fretland, Å. A., Brun, H., Elle, O. J., and Edwin, B. (2020). Use of mixed reality for improved spatial understanding of liver anatomy. *Minimally Invasive Therapy & Allied Technologies*, 29(3):154–160.
- [Pepe et al., 2019] Pepe, A., Trotta, G. F., Mohr-Ziak, P., Gsaxner, C., Wallner, J., Bevilacqua, V., and Egger, J. (2019). A marker-less registration approach for mixed reality-aided maxillofacial surgery: a pilot evaluation. *Journal of digital imaging*, 32(6):1008–1018.
- [Pfeiffer et al., 2020] Pfeiffer, M., Riediger, C., Leger, S., Kühn, J.-P., Sepelt, D., Hoffmann, R.-T., Weitz, J., and Speidel, S. (2020). Non-rigid volume to surface registration using a data-driven biomechanical model. In *International Conference on Medical Image Computing and Computer-Assisted Intervention*, pages 724–734. Springer.
- [Qian et al., 2018] Qian, L., Deguet, A., and Kazanzides, P. (2018). Arssist: augmented reality on a head-mounted display for the first assistant in robotic surgery. *Healthcare technology letters*, 5(5):194–200.
- [Read and Meyer, 2000] Read, P. and Meyer, M.-P. (2000). *Restoration of motion picture film*. Elsevier.
- [Ren et al., 2013] Ren, H., Campos-Nanez, E., Yaniv, Z., Banovac, F., Abeledo, H., Hata, N., and Cleary, K. (2013). Treatment planning and image guidance for radiofrequency ablation of large tumors. *IEEE journal of biomedical and health informatics*, 18(3):920–928.
- [Ren et al., 2014a] Ren, H., Campos-Nanez, E., Yaniv, Z., Banovac, F., Abeledo, H., Hata, N., and Cleary, K. (2014a). Treatment planning and image guidance for radiofrequency ablation of large tumors. *IEEE journal of biomedical and health informatics*, 18(3):920–928.

- [Ren et al., 2014b] Ren, H., Guo, W., Ge, S. S., and Lim, W. (2014b). Coverage planning in computer-assisted ablation based on genetic algorithm. *Computers in biology and medicine*, 49:36–45.
- [Ren et al., 2007] Ren, Q., Nishioka, S., Shirato, H., and Berbeco, R. I. (2007). Adaptive prediction of respiratory motion for motion compensation radiotherapy. *Physics in medicine and biology*, 52(22):6651.
- [Rhim et al., 2008] Rhim, H., Lee, M. H., Kim, Y.-s., Choi, D., Lee, W. J., and Lim, H. K. (2008). Planning sonography to assess the feasibility of percutaneous radiofrequency ablation of hepatocellular carcinomas. *American Journal of Roentgenology*, 190(5):1324–1330.
- [Rojas-Muñoz et al., 2019] Rojas-Muñoz, E., Cabrera, M. E., Andersen, D., Popescu, V., Marley, S., Mullis, B., Zarzaur, B., and Wachs, J. (2019). Surgical telementoring without encumbrance: a comparative study of see-through augmented reality-based approaches. *Annals of surgery*, 270(2):384–389.
- [Salati et al., 2017] Salati, U., Barry, A., Chou, F. Y., Ma, R., and Liu, D. M. (2017). State of the ablation nation: a review of ablative therapies for cure in the treatment of hepatocellular carcinoma. *Future Oncology*, 13(16):1437–1448.
- [Sauer et al., 2003] Sauer, F., Schoepf, U. J., Khamene, A., Vogt, S., Das, M., and Silverman, S. G. (2003). Augmented reality system for ct-guided interventions: System description and initial phantom trials. In *Medical Imaging 2003: Visualization, Image-Guided Procedures, and Display*, volume 5029, pages 384–395. International Society for Optics and Photonics.
- [Schumann et al., 2010] Schumann, C., Bieberstein, J., Trumm, C., Schmidt, D., Bruners, P., Niethammer, M., Hoffmann, R., Mahnken, A., Pereira, P., and Peitgen, H.-O. (2010). Fast automatic path proposal computation for hepatic needle placement. *Fraunhofer MEVIS*.
- [Schumann et al., 2015] Schumann, C., Rieder, C., Haase, S., Teichert, K., Süß, P., Isfort, P., Bruners, P., and Preusser, T. (2015). Interactive multi-criteria planning for radiofrequency ablation. *International journal of computer assisted radiology and surgery*, 10(6):879–889.
- [Schweikard et al., 2004] Schweikard, A., Shiomi, H., and Adler, J. (2004). Respiration tracking in radiosurgery. *Medical physics*, 31(10):2738–2741.
- [Scopis Inc., 2017] Scopis Inc. (2017). Scopis Introduces the First Mixed-Reality Surgical Holographic Navigation Platform Integrating Microsoft HoloLens for Open and Minimally-Invasive Spine Surgery. <https://www.businesswire.com/news/home/20170505005037/en/>

- Scopis-Introduces-Mixed-Reality-Surgical-Holographic-Navigation-Platform. [Online; accessed 07-August-2019].
- [Seiko Epson Corp., 2020] Seiko Epson Corp. (2020). MOVERIO Smart Glasses Epson. <https://moverio.epson.com/>. [Online; accessed 14-January-2020].
- [Seitel et al., 2011a] Seitel, A., Engel, M., Sommer, C., Radeleff, B., Essert-Villard, C., Baegert, C., Fangerau, M., Fritzsche, K., Yung, K., Meinzer, H., and Maier-Hein, L. (2011a). Computer-assisted trajectory planning for percutaneous needle insertions. *Medical Physics*, 38(6):3246–3259.
- [Seitel et al., 2011b] Seitel, A., Engel, M., Sommer, C. M., Radeleff, B. A., Essert-Villard, C., Baegert, C., Fangerau, M., Fritzsche, K. H., Yung, K., Meinzer, H.-P., et al. (2011b). Computer-assisted trajectory planning for percutaneous needle insertions. *Medical physics*, 38(6Part1):3246–3259.
- [Simon et al., 2005] Simon, C. J., Dupuy, D. E., and Mayo-Smith, W. W. (2005). Microwave ablation: Principles and applications. *RadioGraphics*, 25(suppl.1):S69–S83. PMID: 16227498.
- [Stadler, 1979] Stadler, W. (1979). A survey of multicriteria optimization or the vector maximum problem, part i: 1776–1960. *Journal of Optimization Theory and Applications*, 29(1):1–52.
- [sun Kim et al., 2006] sun Kim, Y., Rhim, H., Cho, O. K., Koh, B. H., and Kim, Y. (2006). Intrahepatic recurrence after percutaneous radiofrequency ablation of hepatocellular carcinoma: Analysis of the pattern and risk factors. *European Journal of Radiology*, 59(3):432 – 441. Uncommon Traumatic Injuries.
- [Swiss Society of Virtual and Augmented Reality, 2017] Swiss Society of Virtual and Augmented Reality (2017). Philips Augmented-Reality Surgical Navigation System. <https://ssvar.ch/philips-augmented-reality-surgical-navigation-system/>. [Online; accessed 07-August-2019].
- [Teittinen, 1993] Teittinen, M. (1993). Depth cues in the human visual system. *The Encyclopedia of Virtual Environments 1*.
- [The Johns Hopkins University, 2022a] The Johns Hopkins University, The Johns Hopkins Hospital, J. (2022a). Deep brain stimulation. <https://www.hopkinsmedicine.org/health/treatment-tests-and-therapies/deep-brain-stimulation>. [Online; accessed 16-April-2022].

- [The Johns Hopkins University, 2022b] The Johns Hopkins University, The Johns Hopkins Hospital, V. (2022b). Tumor ablation. <https://www.hopkinsmedicine.org/interventional-radiology/procedures/tumor/>. [Online; accessed 06-April-2022].
- [Tiong and Maddern, 2011] Tiong, L. and Maddern, G. (2011). Systematic review and meta-analysis of survival and disease recurrence after radiofrequency ablation for hepatocellular carcinoma. *British Journal of Surgery*, 98(9):1210–1224.
- [UPMC Presbyterian, 2022] UPMC Presbyterian (2022). Neurological surgery. <https://www.neurosurgery.pitt.edu/centers/epilepsy/seeg>. [Online; accessed 16-April-2022].
- [Villard et al., 2005] Villard, C., Baegert, C., Schreck, P., Soler, L., and Gangi, A. (2005). Optimal trajectories computation within regions of interest for hepatic rfa planning. In Duncan, J. S. and Gerig, G., editors, *Medical Image Computing and Computer-Assisted Intervention – MICCAI 2005*, pages 49–56, Berlin, Heidelberg. Springer Berlin Heidelberg.
- [Waltz et al., 2006] Waltz, R. A., Morales, J. L., Nocedal, J., and Orban, D. (2006). An interior algorithm for nonlinear optimization that combines line search and trust region steps. *Mathematical programming*, 107(3):391–408.
- [Wang et al., 2011] Wang, D., Zhang, Y., Zhou, W., Zhao, H., and Chen, Z. (2011). Collocation accuracy of visuo-haptic system: metrics and calibration. *IEEE transactions on haptics*, 4(4):321–326.
- [Wang et al., 2012] Wang, Z., Aarya, I., Gueorguieva, M., Liu, D., Luo, H., Manfredi, L., Wang, L., McLean, D., Coleman, S., Brown, S., et al. (2012). Image-based 3d modeling and validation of radiofrequency interstitial tumor ablation using a tissue-mimicking breast phantom. *International journal of computer assisted radiology and surgery*, 7(6):941–948.
- [World Health Organization, 2021] World Health Organization (2021). Cancer. <https://www.who.int/news-room/fact-sheets/detail/cancer>. [Online; accessed 22-August-2021].
- [Wu et al., 2018] Wu, M.-L., Chien, J.-C., Wu, C.-T., and Lee, J.-D. (2018). An augmented reality system using improved-iterative closest point algorithm for on-patient medical image visualization. *Sensors*, 18(8):2505.
- [Wunderink et al., 2008] Wunderink, W., Romero, A. M., De Kruijff, W., De Boer, H., Levendag, P., and Heijmen, B. (2008). Reduction of respiratory liver tumor motion by abdominal compression in stereotactic body frame, analyzed by tracking fiducial markers implanted in liver. *International Journal of Radiation Oncology Biology Physics*, 71(3):907–915.

- [Xie et al., 2017] Xie, T., Islam, M. M., Lumsden, A. B., and Kakadiaris, I. A. (2017). [poster] holographic iray: Exploring augmentation for medical applications. In *2017 IEEE International Symposium on Mixed and Augmented Reality (ISMAR-Adjunct)*, pages 220–222. IEEE.
- [Zhou et al., 2020] Zhou, Z., Yang, Z., Jiang, S., Ma, X., Zhang, F., and Yan, H. (2020). Surgical navigation system for low-dose-rate brachytherapy based on mixed reality. *IEEE Computer Graphics and Applications*, 41(3):113–123.
- [Zhou et al., 2019] Zhou, Z., Yang, Z., Jiang, S., Zhang, F., and Yan, H. (2019). Design and validation of a surgical navigation system for brachytherapy based on mixed reality. *Medical physics*.